

INAUGURAL - DISSERTATION
zur
Erlangung der Doktorwürde
der
Naturwissenschaftlich - Mathematischen
Gesamtfakultät
der
Ruprecht - Karls - Universität
Heidelberg

vorgelegt von
Dipl.-Phys. Hans Engler
aus Ludwigshafen

Tag der mündl. Prüfung: 12.7.2000

**A quasi-electrostatic trap
for neutral atoms**

Gutachter: Priv.-Doz. Dr. Rudolf Grimm
Prof. Dr. Reinhard Neumann

Dissertation
submitted to the
Combined Faculties for the Natural Sciences and for Mathematics
of the Rupertus Carola University of
Heidelberg, Germany
for the degree of
Doctor of natural Sciences

**A quasi-electrostatic trap
for neutral atoms**

presented by
Diplom-Physicist Hans Engler
born in Ludwigshafen

Heidelberg, 12.7.2000

Referees: Priv.-Doz. Dr. Rudolf Grimm
Prof. Dr. Reinhard Neumann

Zusammenfassung

Im Rahmen dieser Arbeit wurde eine “quasi-elektrostatische” Atomfalle (QUEST) für neutrale Atome realisiert. Cäsium (^{133}Cs) und Lithium (^7Li) wurden gespeichert und damit erstmals die Mischung verschiedener Spezies in einer optischen Dipolfalle demonstriert. Die Falle wird durch den Fokus eines CO_2 -Laser Strahls mit 30 W Dauerstrich-Leistung und nahezu gauss'schem Strahlprofil gebildet. Bei einem Fokus mit einer Strahltaile von $108\ \mu\text{m}$ beträgt die Fallentiefe $k_B \times 118\ \mu\text{K}$ für Cäsium und $k_B \times 48\ \mu\text{K}$ für Lithium. Es werden bis zu 2×10^6 Cäsium und 10^5 Lithium Atome aus einer magnetooptischen Falle in die QUEST transferiert, wobei bei gleichzeitiger Speicherung beider Spezies die transferierte Teilchenzahl derzeit noch etwa eine Größenordnung kleiner ist. Da Photonenstreuung aus dem Fallenlicht vernachlässigt werden kann, stellt die QUEST eine fast perfekte Realisierung eines konservativen Fallenpotentials dar. Die in der QUEST gespeicherten Atome befinden sich in ihren elektronischen Grundzuständen, wobei beliebige Unterniveaus durch optisches Pumpen populiert werden können. Aufgrund des sehr geringen Hintergrundsdrucks von 2×10^{-11} mbar erreichen wir Speicherzeiten von mehreren Minuten. Verdampfungs-Kühlung bei Cäsium wird beobachtet. Ein zweiter, effektiverer Kühlmechanismus für die Cäsium-Wolke in der QUEST wird demonstriert: mittels Laserkühlung in der Falle kann die Temperatur von $25\ \mu\text{K}$ auf unter $7\ \mu\text{K}$ reduziert werden. Bei Präparation der Atome im oberen Hyperfeinniveau des Grundzustands beobachten wir spinändernde Stöße nicht nur innerhalb einer Spezies, sondern erstmals auch zwischen zwei verschiedenen Atomsorten. Die entsprechenden Relaxationsraten werden quantitativ analysiert.

Abstract

This thesis reports on the realization of a “quasi-electrostatic trap” (QUEST) for neutral atoms. Cesium (^{133}Cs) and Lithium (^7Li) atoms are stored, which represents for the first time a mixture of different species in an optical dipole trap.

The trap is formed by the focused Gaussian beam of a 30 W cw CO_2 -laser. For a beam waist of $108\ \mu\text{m}$ the resulting trap depth is $k_B \times 118\ \mu\text{K}$ for Cesium and $k_B \times 48\ \mu\text{K}$ for Lithium. We transfer up to 2×10^6 Cesium and 10^5 Lithium atoms from a magneto-optical trap into the QUEST. When simultaneously transferred, the atom number currently is reduced by roughly a factor of 10. Since photon scattering from the trapping light can be neglected, the QUEST represents an almost perfect conservative trapping potential. Atoms in the QUEST populate the electronic ground state sublevels. Arbitrary sublevels can be addressed via optical pumping. Due to the very low background gas pressure of 2×10^{-11} mbar storage times of several minutes are realized. Evaporative cooling of Cesium is observed. In addition, laser cooling is applied to the trapped Cesium sample, which reduces the temperature from $25\ \mu\text{K}$ to a value below $7\ \mu\text{K}$. If prepared in the upper hyper-fine ground state sublevel, spin changing collisions are observed not only within one single species, but also between the two different species. The corresponding relaxation rates are quantitatively analyzed.

Contents

1	Introduction	3
2	Quasi-electrostatic optical dipole trap	7
2.1	Dipole potential and scattering rate	7
2.2	Quasi-electrostatic trap (QUEST)	10
2.3	Heating mechanisms in a QUEST	11
2.4	Cooling methods	13
3	Experimental prerequisites	21
3.1	The Lithium atom	21
3.2	The Cesium atom	22
3.3	Radiation pressure trap	23
3.4	Vacuum system	25
3.5	CO ₂ -laser system and resulting trap parameters	31
3.6	Detection methods	37
3.7	Timing of the experiment	40
4	Characterizing the quasi-electrostatic trap	43
4.1	Typical parameters of trapped Cesium atoms	43
4.2	Determination of the radial trap frequency	44
4.3	Typical parameters of trapped Lithium atoms	47
5	Transfer into the QUEST	49
5.1	Model	50
5.2	Cesium transfer	53
5.3	Lithium transfer	58
6	Long time storage	63
6.1	Long storage times of Cesium	63

6.2	Long storage times of Lithium	68
7	Cooling of Cesium	73
7.1	Evaporative cooling of Cesium	73
7.2	Polarization-gradient cooling of Cesium inside the QUEST	77
8	Simultaneous trapping of Cesium and Lithium	85
8.1	Combined transfer of Cesium and Lithium	85
8.2	Inelastic interspecies ground state collisions	88
9	Status and prospects	91
A	B-field compensation by ground state Hanle effect	95
B	Magnetic fields of the new apparatus	101
B.1	MOT magnetic field	101
B.2	Magnetic field for compensation of residual fields	102
B.3	New Lithium Zeeman-slower section	104
B.4	New Cesium Zeeman-slower section	107
C	Polarization-gradient cooling of Cesium in free space	111
D	Absorption imaging	115
E	Analytical model of transfer efficiency	117
	Bibliography	121

Chapter 1

Introduction

Methods for storage and trapping of particles have often been the experimental key to great scientific advances. For neutral atoms the regime of ultralow temperature became experimentally accessible due to the dramatic developments in the field of laser cooling and trapping in the last twenty years [Met95]. Today it has become experimental routine to produce ensembles in the microkelvin scale. Applications can be found in many different fields, such as high-resolution spectroscopy and metrology [Ber95], ultracold collisions [Wei99b] and investigation of quantum statistical effects in Bose-Einstein condensation [Ket99].

The experiments are performed in atom traps, which can be realized on the basis of three different interactions, each having specific properties and offering particular advantages:

Radiation pressure traps operating with near resonant light, have a typical depth of a few kelvin. Because of very strong energy dissipation they allow to capture and accumulate atoms from an atomic beam or thermal gas. The atomic ensemble is trapped and simultaneously cooled below a temperature of 1 mK. Therefore these traps are often used as a tool to provide a dense and cold sample of atoms for further investigations. Most common is the “magneto optical trap”, which was firstly realized by Raab *et al.* [Raa87]. It utilizes radiation pressure in combination with an inhomogeneous magnetic field to confine the atoms.

Magnetic traps are based on the force acting on the atomic magnetic dipole moment in an inhomogeneous magnetic field [Ber87]. Representing an ideal conservative trap with a depth on the order of 100 mK, it is an excellent tool for evaporative cooling and the achievement of Bose-Einstein condensation. A fundamental restriction is imposed by the fact that the trapping mechanism relies on the internal atomic state, which determines the magnetic dipole moment. In general the absolute magnetic ground state will be repelled from such a trap.

Optical dipole force traps rely on the interaction of the induced atomic dipole moment with a light field [Gri00, Wei99a]. Typical trap depths are in the range below one millikelvin. If the laser frequency is detuned below an atomic resonance, the simplest setup is realized by a focused laser beam, for which the focus represents the trapping volume.

The first atom trap was realized in 1986 by Chu *et al.* [Chu86]. They used a focused beam optical dipole trap, operated at relatively small detunings of several hundred GHz. Hence a significant fraction of the atoms populated excited states and radiation pressure was not negligible. Miller *et al.* [Mil93] demonstrated the first “far-off resonance” dipole trap in 1993. The detuning was 65 nm below resonance, strongly suppressing atomic excitation and radiation pressure effects. The photon scattering rate was on the order of 10^3 per s. An extreme type of such a trap, providing photon scattering on the order of 1 per hour, was introduced by Takekoshi *et al.* [Tak95] in 1995 by utilizing a CO₂-laser at $\lambda = 10.6 \mu\text{m}$. Due to the huge detuning from any atomic resonance the interaction of the *static* polarizability of the atoms with the light field determines the confining potential. Therefore this trap is called “quasi-electrostatic trap” (QUEST).

Today optical dipole traps find many applications: cold collisions [Vul99], formation of molecules via photoassociation [Hei99] as well as the storage of the ground state molecules [Tak98] are studied. New optical cooling schemes were developed Kermann *et al.* [Ker99]. Recently optical dipole traps entered the domain of magnetic traps in BEC experiments [Sta98]. Even outside the “cold atom community” one utilizes optical dipole traps, e.g. as optical tweezers in biochemistry [Gre95].

The advantages of an dipole trap over other types of traps are, besides technical considerations, based on the ability to trap particles in the absence of magnetic fields, which allows to fully control the internal atomic degrees of freedom. For large detunings, the dipole force does not depend on the particular ground state hyperfine or magnetic sublevel. This allows for sub-Doppler [Boi98] and sub-recoil cooling [Lee96, Kuh96] and facilitates experiments at zero or arbitrary external magnetic fields. Moreover, the optical excitation can be kept low, so that such a trap is not limited by light induced mechanisms present in radiation-pressure traps. As a further advantage, many different trapping geometries can be realized, which allows for various potential shapes [Gri00].

We have chosen a quasi-electrostatic trap for our experiment, because it is the ideal tool to investigate the ground state interaction between two different species. We decided to combine the heaviest (stable) alkali Cesium (Cs) and the lightest one, Lithium (Li). Nothing is known so far about the scattering cross section of Lithium and Cesium. This combination is particular interesting, since the Li-Cs system represents a promising mixture for experiments related to sympathetic cooling of Lithium using Cesium as a cold reservoir. Due to its large mass Cesium has a low recoil temperature and can therefore be cooled down to a few μK . When transferring this temperature to the Lithium ensemble via elastic collisions, due to its small mass, Lithium will reach the quantum degenerated state at moderate densities of $10^{13}/\text{cm}^3$. In this context working with Lithium is quite attractive, since the quantum statistical behaviour of the bosonic isotope (^7Li) and also of the fermionic isotope (^6Li) could be investigated. Collisional phenomena

of Lithium are of particular interest since ground state sublevels with attractive and repulsive interaction potentials can be prepared in the QUEST. The freedom to apply external magnetic fields gives one as well the opportunity to investigate Feshbach resonances [Vul99].

Bose-Einstein condensation of ^7Li was so far only achieved in magnetic traps [Bra95]. Here only magnetic substates are trapped which exhibit an attractive interaction among the particles, limiting the number of condensed atoms to about 2000 [Bra97]. In a QUEST ^7Li can be prepared in substates with repulsive interaction, therefore setting no principle limit on the number of condensed particles.

Cesium itself is an attractive atom for ground state studies, because of its extremely large elastic and inelastic scattering cross section and the existence of a Zero-Energy resonance [Arn97].

We have also chosen the QUEST because of its ability to confine molecules, since we plan the formation of ultracold, stable Li-Cs dimers via photoassociation in their ground state. The Li-Cs dimer will have a large internal dipole moment and hence will serve as a prototype molecule for the development of manipulation techniques based on electrostatic fields.

Important experimental steps towards these goals were realized and are reported in this thesis. We show that both atomic species can be confined in the same trapping volume. Due to the differing temperatures achieved on both species with laser cooling, individual transfer schemes were developed. Via optical pumping we are able to populate certain ground state sublevels, in particular the lowest energetic ground state which excludes loss through inelastic binary collisions. Here we achieved storage times of several minutes, which are among the longest storage times ever achieved in optical dipole traps [O'H99]. On these long time scales we investigated evaporative cooling of the particles. Besides the excellent vacuum of our apparatus, both results were only made possible by the absence of photon scattering. Since the optical dipole potential is independent of the magnetic sublevels, we applied polarization-gradient cooling to Cesium inside the QUEST. Furthermore we prepared the atoms in the upper ground state sublevel by optical pumping and investigated spin-changing ground state collisions of unpolarized Cesium and Lithium. For the first time we were able to observe ground state collisions between different species.

The present thesis is structured as follows: chapter two gives the basics about the optical dipole potential and introduces the mechanism and possibility of polarization-gradient cooling inside the QUEST. Chapter three introduces our experimental setup. Details about the concept of the vacuum system are covered as well as the optical setup and detection methods. Chapter four characterizes the basic properties of the trapped Cesium and Lithium ensembles. Since a quasi-electrostatic trap is loaded from magneto optical traps, chapter five introduces the transfer procedure, which is conceptionally different for both species. The achievement of long storage

times are subject of chapter six. When separately stored, we reached storage times of several minutes for both candidates, due to the excellent vacuum and the absence of heating by trap light. We observed spin changing ground state collisions, showing up as exoergic binary collisions. The associated loss rate coefficients for both species are given. Chapter seven reports on evaporative cooling and polarization-gradient cooling on Cesium inside the QUEST down to a temperature of a few μK . Chapter eight reports on the first observation of interspecies ground state collisions. In chapter nine the prospects of the experiment are given.

Chapter 2

Quasi-electrostatic optical dipole trap

Optical dipole traps rely on the electric dipole interaction of particles with far-detuned laser light. The interaction is very weak, typical trap depths are in the range below one millikelvin. The optical excitation can be kept extremely low, so that such a trap is not limited by the light induced mechanisms present in radiation pressure traps.

In the present chapter the main features of optical dipole traps are introduced. This section is based on [Gri00] and structured as follows: After a brief introduction of the physics underlying the optical dipole force acting on neutral atoms, the basic equations for the optical dipole potential and photon scattering rate are derived. Then an extreme representative of so-called “red-detuned” optical dipole traps is introduced: the carbon-dioxide (CO_2) laser trap, which represents a *quasi-electrostatic trap* [Tak95] due to the huge detuning of the trapping light ($\lambda_{\text{CO}_2} = 10.6 \mu\text{m}$) from any atomic transition. The chapter ends with a discussion of heating and cooling mechanisms of atoms inside this type of trap.

2.1 Dipole potential and scattering rate

The optical dipole force arises from the dispersive interaction of the induced atomic dipole moment with the intensity gradient of the light field [Gor80]. Due to its conservative character, the force can be derived from a potential, the minima of which can be used for trapping neutral atoms.

2.1.1 Main properties

Consider an atom placed in laser light. The electric field \vec{E} induces an atomic dipole moment \vec{p} that oscillates with the driving field frequency ω . Using the complex notation $\vec{E}(\vec{r}, t) = \hat{e}\tilde{E}(\vec{r})\exp(-i\omega t) + c.c.$ and $\vec{p}(\vec{r}, t) = \hat{e}\tilde{p}(\vec{r})\exp(-i\omega t) + c.c.$, where \hat{e} is the unit polarization vector. The amplitude \tilde{p} of the dipole moment is related to the light field

amplitude \tilde{E} by

$$\tilde{p} = \alpha \tilde{E}. \quad (2.1)$$

The complex polarizability $\alpha \equiv \alpha(\omega)$ depends on the driving frequency ω .

The *interaction potential* of the induced dipole moment \vec{p} in the driving field \vec{E} is given by the relation

$$U_{dip} = -\frac{1}{2} \langle \vec{p} \vec{E} \rangle = -\frac{1}{2\epsilon_0 c} \text{Re}(\alpha(\omega)) I, \quad (2.2)$$

where the factor $\frac{1}{2}$ takes into account that the dipole moment is not a permanent but an induced one, the angular brackets denote the time average over the rapid oscillation terms, and $I = 2\epsilon_0 c |\tilde{E}|^2$ is the field intensity. Eq. 2.2 gives the potential energy experienced by the atom, which is proportional to the intensity I of the light, as well as to the real part of the polarizability $\alpha(\omega)$. The real part of the polarizability describes the in-phase component of the dipole oscillation, being responsible for the dispersive properties of the interaction.

The gradient of the interaction potential generates the *dipole force*.

$$F_{dip}(\vec{r}) = -\nabla U_{dip}(\vec{r}) = \frac{1}{2\epsilon_0 c} \text{Re}(\alpha(\omega)) \nabla I(\vec{r}). \quad (2.3)$$

The dipole force is thus proportional to the intensity gradient of the driving field.

The *absorbed power* of the oscillator in the field results from the imaginary part of the atomic polarizability, which describes the out-of-phase component of the oscillation. It is given by

$$P_{abs} = \langle \dot{\vec{p}} \vec{E} \rangle = 2\omega \text{Im}(\tilde{p} \tilde{E}^*) = \frac{\omega}{\epsilon_0 c} \text{Im}(\alpha(\omega)) I. \quad (2.4)$$

Regarding the light as a stream of photons with energy $\hbar\omega$, the absorption can be interpreted in terms of photon scattering in cycles of absorption and subsequent spontaneous emission processes.

The corresponding *scattering rate* is

$$\Gamma_{sc} = \frac{P_{abs}}{\hbar\omega} = \frac{1}{\hbar\epsilon_0 c} \text{Im}(\alpha(\omega)) I. \quad (2.5)$$

The interaction potential and the scattered radiation power in terms of the field intensity $I(\vec{r})$ and the polarizability $\alpha(\omega)$ are the main quantities of optical dipole traps. These expressions are valid for any polarizable neutral particle in an oscillating field, which can be an atom or even a molecule in a near-resonant or far off-resonant field.

2.1.2 The oscillator model for the atomic polarizability

To calculate the polarizability $\alpha(\omega)$ one can consider the atom in the Lorentz's model of a classical oscillator, where the electron is bound elastically to the core with an oscillation eigenfrequency

ω_0 corresponding to the optical transition frequency. By integrating the equation of motion $\ddot{x} + \Gamma_\omega \dot{x} + \omega_0^2 x = -eE(t)/m_e$ for the driven oscillation of the electron, one gets

$$\alpha(\omega) = \frac{e^2}{m_e} \frac{1}{\omega_0^2 - \omega^2 - i\omega\Gamma_\omega}. \quad (2.6)$$

Here

$$\Gamma_\omega = \frac{e^2\omega^2}{6\pi\epsilon_0 m_e c^3} \quad (2.7)$$

is the classical damping rate due to the radiative energy loss [Jac62]. By substituting $e^2/m_e = 6\pi\epsilon_0 m_e c^3 \Gamma_\omega/\omega^2$ and introducing the on-resonance damping rate $\Gamma \equiv \Gamma_{\omega_0} = \Gamma_\omega(\omega_0/\omega)^2$, Eq. 2.6 is put into the form

$$\alpha(\omega) = 6\pi\epsilon_0 c^3 \frac{\Gamma/\omega_0^2}{\omega_0^2 - \omega^2 - i(\omega^3/\omega_0^2)\Gamma}. \quad (2.8)$$

Remarks:

- The *classical oscillator* picture does not consider the possible occurrence of saturation. At too high intensities of the driving field, the excited state gets strongly populated and Eq. 2.8 is no longer valid. For dipole trapping, one is especially interested in the far-detuned case of very low saturation and thus very low scattering rates ($\Gamma_{sc} \ll \Gamma$). Therefore we can use the expression in Eq. 2.8 also as an excellent approximation for the quantum-mechanical oscillator.
- In a *semiclassical approach* the atomic polarizability can be calculated by considering an atom as a two-level quantum system interacting with the classical radiation field. As long as saturation effects can be neglected, the semi-classical calculation yields the same result as Eq. 2.8, with only one modification: In general the damping rate Γ (corresponding to the spontaneous decay rate of the excited level) can no longer be calculated from Eq. 2.7, but is determined by the dipole matrix element between the ground and excited state:

$$\Gamma = \frac{\omega_0^3}{6\pi\epsilon_0 \hbar c^3} |\langle e|\mu|g\rangle|^2. \quad (2.9)$$

For the *D*-lines of the alkali atoms the classical result agrees with the true decay rate to within a few percent.

With the above expression for the polarizability $\alpha(\omega)$ the following explicit expressions are derived for the optical dipole potential and the scattering rate in the relevant case of large detuning and negligible saturation:

$$U_{dip}(\vec{r}) = -\frac{3\pi c^2}{2\omega_0^3} \left(\frac{\Gamma}{\omega_0 - \omega} + \frac{\Gamma}{\omega_0 + \omega} \right) I(\vec{r}), \quad (2.10)$$

$$\Gamma_{sc}(\vec{r}) = \frac{3\pi c^2}{2\hbar\omega_0^3} \left(\frac{\omega}{\omega_0} \right)^3 \left(\frac{\Gamma}{\omega_0 - \omega} + \frac{\Gamma}{\omega_0 + \omega} \right)^2 I(\vec{r}). \quad (2.11)$$

These are general expressions, valid for any driving frequency ω . They show two resonant contributions: Besides the usually considered resonance at $\omega = \omega_0$, there is also the so-called counter-rotating term resonant at $\omega = -\omega_0$.

2.2 Quasi-electrostatic trap (QUEST)

Pushing the principle of a red-detuned dipole trap to its extreme, one can consider a quasi-electrostatic trap (QUEST) [Tak95], for which the frequency of the trapping light ω is by more than one decade smaller than the frequency of any atomic transition. In this quasi-electrostatic situation $\omega \ll \omega_0$, one can replace $\alpha(\omega)$ by the static polarizability $\alpha_{stat} \equiv \alpha(\omega = 0) = \frac{e^2}{m_e \omega_0^2}$, which directly follows from Eq. 2.6 in the case of $\omega \rightarrow 0$ and is called the “quasi-electrostatic approximation”. Now, using Eq. 2.2 one can express the optical dipole potential as

$$U_{dip}(\vec{r}) = -\alpha_{stat} \frac{I(\vec{r})}{2\epsilon_0 c}. \quad (2.12)$$

Here the optical dipole potential is always attractive, independently of the atomic state, since the trap depth in Eq. 2.12 does not depend on the detuning from a specific resonance line as in the case of a far off-resonance trap (FORT). Atoms can therefore be stored in any internal state by the same light field. Even different atomic species and molecules might simultaneously be captured in the same trapping volume. For a given intensity the trap depth only depends on the value of α_{stat} . For the ground-state of alkalis, Eq. 2.12 is well approximated by applying the quasi static approximation to Eq. 2.10 which gives an expression of the trapping potential in experimentally relevant terms:

$$U_{dip}(\vec{r}) = -\frac{3\pi c^2}{\omega_0^3} \frac{\Gamma}{\omega_0} I(\vec{r}). \quad (2.13)$$

Compared to a FORT at a given detuning $\Delta = \omega - \omega_0$, the optical dipole potential for ground state atoms in a QUEST is smaller by a factor of $2\Delta/\omega_0$. Therefore, high power lasers in the far-infrared spectral range have to be employed to create sufficiently deep traps. CO₂-lasers at $\lambda = 10.6 \mu\text{m}$ which are commercially available with cw powers up to some kilowatts are particularly well suited for the realization of a QUEST [Tak95].

A very important feature of the QUEST is the absence of photon scattering. The relation between

photon scattering rate and trap depth can be derived from Eq. 2.10 and Eq. 2.11 in the quasi-electrostatic approximation:

$$\hbar\Gamma_{sc}(\vec{r}) = 2 \left(\frac{\omega}{\omega_0} \right)^3 \frac{\Gamma}{\omega_0} U_{dip}(\vec{r}). \quad (2.14)$$

Therefore atoms captured in the QUEST occupy all the time their ground-states. Typical scattering rates are below one photon per hour, showing that the QUEST is representing an ideal realization of a purely conservative trap.

Besides our experiment there are three other groups working with a CO₂-laser trap:

- Takekoshi and Knize at the University of Southern California in Los Angeles have firstly realized trapping in a focused CO₂-laser in 1996 [Tak96]. They could store up to 10⁶ cesium atoms in the 100 μm waist of a 20 W laser, leading to a potential depth of 115 μK. The atomic sample was prepared in the $F = 3$ ground state. Due to background gas collisions, the lifetime of the trapped atoms was about 3 s.
- The group around Thomas and O'Hara at the Duke University in Durham, NC has closely investigated laser induced heating in dipole traps. With an extremely stable setup and an excellent vacuum of 10⁻¹¹ mbar they have reached storage times for Lithium on the order of several 100 seconds [O'H99].
- In Munich at the MPI für Quantenoptik the group of Weitz and Hänsch works with Rubidium atoms in a 1-dimensional, mesoscopic optical lattice, created by a 5 W CO₂-laser [Fri98b, Fri98c]. The laser is focused on a waist of 50 μm, creating a trap potential U/k_B of 360 μK. About 3×10^4 atoms were transferred into this standing wave trap, the lifetime of 1.8 s was limited by background gas collisions. Temperatures of about 10 μK were achieved by polarization gradient cooling.

2.3 Heating mechanisms in a QUEST

Basically there are three possible mechanisms of heating in a CO₂-laser trap: collisions with hot background gas atoms, photon scattering by the trap light, and laser fluctuations. The effect of the first argument might considerably be suppressed by generating an excellent vacuum. Concerning heating by trap light, one can calculate the scattering rate to get a reliable estimation for the associated heating rate. For our experiment the most critical point were laser fluctuations, since the appropriate values of the laser we used are not given by the manufacturer.

Collisions with background gas atoms at a temperature of 300 K will rather lead to single particle loss than to heating of trapped atoms. Since typical trap potentials U_0/k_B are on the order of a few mK or below, almost every collision with a background gas atom of energy E_{bg}

will lead to an instant escape from the trap. This mechanism scales linearly with the background gas pressure and therefore can be externally controlled. However, it is known that small-angle collisions can leave atoms in the trap and cause heating. In shallow traps where $U_0 \ll E_{bg}$, this heating arises from diffractive collisions [Bal99], where the angle θ between the final and initial relative velocity \vec{v}_r is small. A short estimation according to [Bal99] shows that this heating is extremely unlikely to occur in the present case, since θ has to be very small, in order to cause only heating instead of a clean loss: An atom escapes in any case from the trap if the transferred energy $\Delta E > U_0$. For small scattering angles $\Delta E \simeq \mu |\vec{v}_r|^2 \theta^2$, where μ is the reduced mass. For traps at very low pressure, He and H₂ are the dominant background gases. In the case of trapped Cesium colliding with a hot He atom, the upper limit of the diffractive angle not leading to instant trap loss can be estimated from the above equation to less than 0.002 mrad. Thus heating processes due to background gas collisions are highly negligible and indeed were not observed in our experiment.

Heating by the trap light is an issue of particular importance in red-detuned traps, since the atoms are located in the most intense spot of the laser light. The scattering is completely elastic, which means the energy of the scattered photons is determined by the frequency of the trapping light and not of the atomic resonance. Both absorption and spontaneous re-emission show fluctuations and thus contribute to the heating [Min87]. In contrast to a far-detuned dipole trap (FORT), where this elastic scattering plays an important role, in the case of a QUEST this process is completely negligible: firstly, the heating scales with $E_{rec} = (\hbar k)^2/(2m)$ per scattering event, which is considerably small for photons at $\lambda_{CO_2} = 10.6 \mu\text{m}$. Secondly, according to Eq. 2.14 one calculates for an assumed trap potential of $U/k_B \approx 100 \mu\text{K}$ in the case of Cesium a scattering rate of $\Gamma_{sc} = 2 \times 10^{-5}$ photons per second, which is equivalent to 1.7 photons per day! The heating power $P_{heat} \propto E_{rec} \times \Gamma_{sc}$ is therefore negligible for the relevant time scales of up to several minutes in our experiment.

Fluctuations in the laser source. It was recently pointed out by Savard *et al* [Sav97] that technical heating can occur due to *intensity fluctuations* and *beam pointing instabilities*. In the first case, fluctuations occurring at twice the characteristic trap frequencies are relevant, as they can parametrically drive the oscillatory motion of the atoms. In the second case a shaking of the optical dipole potential at the trap frequencies increases the motional amplitude. Experimentally, these issues will strongly depend on the particular laser source and its technical noise spectrum. It is therefore difficult to predict the quantity of laser induced heating. However, the setup of the optical system for the trapping light beam should be made as mechanically stable as possible in order to avoid additional sources of technical heating.

O'Hara *et al.* demonstrated a longtime storage of Lithium [O'H99] with a lifetime of 300 s in a

CO₂-laser trap. They used a highly sophisticated, custom built laser with extremely low intensity fluctuations. To circumvent beam pointing instabilities the mechanical setup of mirrors and lenses also was quite solid and stable.

The CO₂-laser we use is an industrial grade, 30 W device, of which the relevant parameters for the intensity induced heating rates are not known. Hence it was a crucial point if our laser would negatively influence the storage time by heating. The fact that high quality industrial grade CO₂-lasers are usually used in the metalworking industry led us to the well founded assumption that beam pointing problems due to the laser itself were out of question. An estimation about the intensity noise was not possible. Finally our long time storage experiments showed clearly that the decay time reached is background gas pressure limited.

2.4 Cooling methods

Efficient cooling techniques are an essential requirement to load the atoms into an optical dipole potential since the attainable trap depth U_0/k_B of some 100 μK is very small compared to the energy of the atoms at room temperature. Once trapped, further cooling might be desirable i.e. in order to increase the phase-space density.

Since the potential of a QUEST is purely conservative, the trapping light does not generate any cooling effects. Once the atoms are trapped in a QUEST they do not experience a friction force caused by the trapping laser.

In our experiment we have investigated two “external” cooling mechanisms such as *evaporative* cooling and *blue-detuned molasses* cooling. Experimental results will be presented in the following chapters. In this section only a brief introduction into the two mechanisms will be given.

2.4.1 Evaporative cooling

Evaporative cooling is observed in any trapping potential of limited depth U_0 . It was originally demonstrated with magnetically trapped hydrogen [Hes87] and has been the key technique to achieve Bose-Einstein condensation in magnetic traps [Ket96]. Adams et al. in the group of S. Chu at Stanford University have demonstrated evaporative cooling of sodium atoms in a crossed beam dipole trap at $\lambda = 1.06 \mu\text{m}$ [Ada95]. Starting from an initial temperature of 140 μK , by reducing the trapping potential a final temperature of 4 μK was reached, increasing the phase-space density by a factor of 28.

Evaporative cooling relies on the selective removal of high-energetic particles from the trapped sample and subsequent thermalization of the remaining particles through elastic collisions [Lui96].

Consider an atomic sample at temperature $T \leq U_0/k_B$ in a potential of depth U_0 . On average a particle escaping from the trap takes away the energy $E \approx U_0 + k_B T$.

Evaporative cooling requires high particle densities to assure fast thermalization rates and large initial atom numbers since a large fraction of the trapped particles is removed from the trap during the cooling process. To become effective, the ratio between inelastic collisions causing losses and heating, and elastic collisions providing thermalization and evaporation, has to be large. In a QUEST the inelastic processes are greatly suppressed, since the atoms can be prepared in their absolute ground-state. However, the requirement of large particle numbers in a QUEST poses a dilemma for the application of evaporative cooling. Additionally, the evaporation will come to an end if the ratio η of trap depth and temperature has reached a factor of about 10, because for the atoms it is getting more and more unlikely to surmount the top of the trap. Since in our experiment we can't reduce the trapping potential, the sample of Cesium would not become colder than $U_0/(10 k_B) \approx 10 \mu\text{K}$. The initial temperature of Cesium in the QUEST is about $25 \mu\text{K}$ and below, depending on the transfer scheme (see section 5.2), hence evaporative cooling is not very effective in the present case. Nevertheless we observed evaporative cooling on Cesium in one of our first experiments. The reason that evaporation takes place lies in the combination of very long storage times in our experimental setup and the anomalously large elastic cross section of Cesium at low temperatures [Arn97]. The outcome of evaporative cooling in our experiment is detailed in section 7.1.

2.4.2 Polarization-gradient cooling

The classical optical cooling process relies on the velocity dependent absorption of photons from a pair of counter propagating laser beams due to the Doppler effect, and is therefore called ‘‘Doppler cooling’’. It leads to temperatures not lower than $\approx 100 \mu\text{K}$ (as stated in section 3.3.1).

A different type of cooling arises from the state-dependent nature of the optical dipole potential given in Eq. 2.16. It makes use of a pumping process between differently shifted atomic sublevels. This technique is known as *polarization-gradient cooling* [Dal85]. Dalibard and Cohen-Tannoudji have closely studied the effects of polarization-gradient cooling [Dal89]. In [Met94] a summary of their work is given.

With polarization-gradient cooling one can prepare in free-space atomic samples at temperatures of about $10 \times T_{rec}$, where the recoil temperature

$$T_{rec} = \frac{\hbar^2 k^2}{k_B m} \quad (2.15)$$

is defined as the temperature associated with the kinetic energy gain by emission of one single photon. The achievable temperatures are much below the typical optical dipole potential depth. Besides enhancing the loading efficiency by using a short molasses phase before transfer, polarization-gradient cooling can directly be applied to atoms in a dipole trap by illuminating

them with near-resonant light in a standing wave configuration [Boi98, Win98]. A necessary condition for efficient polarization-gradient cooling inside the trap is the independence of the trapping potential from the Zeeman substates. In contrast to magnetic traps, this is perfectly fulfilled in a QUEST.

In free space polarization-gradient cooling can be done in red-detuned ($\omega < \omega_0$) [Let88, Sal90, Dal89] and blue-detuned ($\omega > \omega_0$) [Asp86, Wei94] fields, where ω denotes the laser frequency. As it turned out in our experiment, in a QUEST only the blue-detuned configuration works efficiently.

Blue molasses cooling on Cesium atoms in a focused-beam trap has been investigated at ENS in Paris [Boi98]. The atoms were trapped in the focus of a 700 mW Nd:YAG beam at $\lambda_{YAG} = 1064$ nm, creating a trap depth of $50 \mu\text{K}$. Polarization-gradient cooling was applied for some milliseconds yielding temperatures between $1 \mu\text{K}$ and $3 \mu\text{K}$.

A second experiment, at the University of Tokyo, reports on polarization-gradient cooling inside a blue-detuned dipole trap with a Laguerre-Gaussian beam [Tor98] from a Ti:sapphire laser. Application of pulsed cooling beams to a large sample (up to 10^8 atoms) of Rubidium (^{85}Rb) has suppressed the trap loss due to heating from the trapping light. The temperatures reached were about $13 \mu\text{K}$.

The group of M. Weitz and T.W. Hänsch at the Max-Planck-Institut für Quantenoptik in Munich reports on blue-detuned molasses cooling of Rubidium atoms in a standing wave CO_2 -laser trap down to $15 \mu\text{K}$ [Fri98a, Fri98c].

In our experiment we have implemented a 3-dimensional polarization-gradient cooling in σ^+/σ^- standing wave configuration to optically cool Cesium atoms during the transfer as well as inside the QUEST. During the transfer red-detuned molasses and blue-detuned molasses are applied, inside the QUEST only blue-detuned molasses cooling was performed successfully. The frequency of the light was typically tuned 5 linewidths to the blue side of the transition $F = 3 \rightarrow F' = 2; 3$ and a repumping beam at the transition $F = 4 \rightarrow F' = 4$ was added. The outcome is detailed in the following chapters.

The *mechanism of polarization-gradient cooling* is illustrated in the following. In order to understand the mechanism, we will briefly introduce the effect of detuned light on atomic energy levels. The generated energy shift $\Delta\mathcal{E}$ is known as “light shift” or “ac Stark shift” and can be treated as a second order perturbation of the electric field, i.e. linear in terms of the electric field intensity. As general result of second order time-independent perturbation theory for non-degenerated states, the interaction leads to an energy shift of the i -state that is given by

$$\Delta\mathcal{E}_i = \sum_{j \neq i} \frac{|\langle j | \mathcal{H}_1 | i \rangle|^2}{\mathcal{E}_i - \mathcal{E}_j}. \quad (2.16)$$

Here \mathcal{E}_i denotes the unperturbed energy and \mathcal{H}_1 gives the interaction Hamiltonian of an atom in

the light field $\mathcal{H}_1 = -\hat{\mu}\vec{E}$, with $\hat{\mu} = -e\vec{r}$ representing the electric dipole operator.

For an optical transition between ground and excited states with angular momentum J respectively J' , Eq. 2.16 leads to the expression

$$\Delta\mathcal{E} = C_{J',m'_J,J,m_J}^2 \times \frac{3\pi c^2}{2\omega_0^3} \frac{\Gamma}{\Delta} I, \quad (2.17)$$

where $m'_J = m_J$ for linear polarization (π) and $m' = m_J \pm 1$ for circular polarization (σ^\pm) of the light field, I is the intensity, and $\Delta \equiv \omega - \omega_0$ denotes the detuning from resonance ω_0 . The real coefficients C_{J',m'_J,J,m_J} are known as Clebsch-Gordon coefficients, their square values can be interpreted as line-strength factors ($C_{J',m'_J,J,m_J}^2 \leq 1$).

By the appropriate configuration of a standing light field one can induce optical pumping between the atomic substates in a way that the motion of an atom in the light field is damped by a Sisyphus effect [Dal89]. This can either be achieved by detuning the light field below resonance (“red-detuned molasses”) or above resonance (“blue-detuned molasses”). For both configurations the temperature limit is clearly below the Doppler temperature. The cooling mechanism is different for the two configurations, as sketched for one dimension in the following.

2.4.3 Cooling below the Doppler limit in red-detuned molasses

Consider an atom subjected to a pair of counter propagating laser beams with perpendicular linear polarization (“lin \perp lin” configuration). The polarization of the resulting light field varies over half a wavelength from linear at 45° (with respect to the polarization of the beams), to σ^+ , to linear but perpendicular to the first direction, to σ^- , and then it repeats.

To illustrate the damping in this polarization-gradient cooling scheme consider the atom is traveling with velocity v in direction of the beam axis, located on a purely σ^+ spot. The light field will pump the atom to the strongly negative shifted $m_J = +1/2$ state. In moving along the axis through the light field, the atom must increase its potential energy (climb up a hill) because the polarization changes and the $m_J = +1/2$ state becomes less strongly down-shifted. The atom arriving at a position $\lambda/4$ away where the field is purely σ^- will be optically pumped to $m_J = -1/2$, which is now the lowest state. Again the moving atom sits at the bottom and starts to climb the hill, converting kinetic into potential energy, as illustrated in Fig. 2.1. Such a process is called “Sisyphus cooling” because of the similarity of its cyclic mechanism to the job of the ancient Greek hero. In the optical pumping process the potential energy is radiated away since the spontaneous emission is at higher frequency than the absorption. Such cooling cycles repeatedly occur until the the kinetic energy is not sufficient any longer to climb the potential well.

According to the calculations in [Dal89, Met94] the final temperature is on the order of $T_{lim} = \Delta\mathcal{E}/k_B$. Hence the final temperature scales with the light shift.

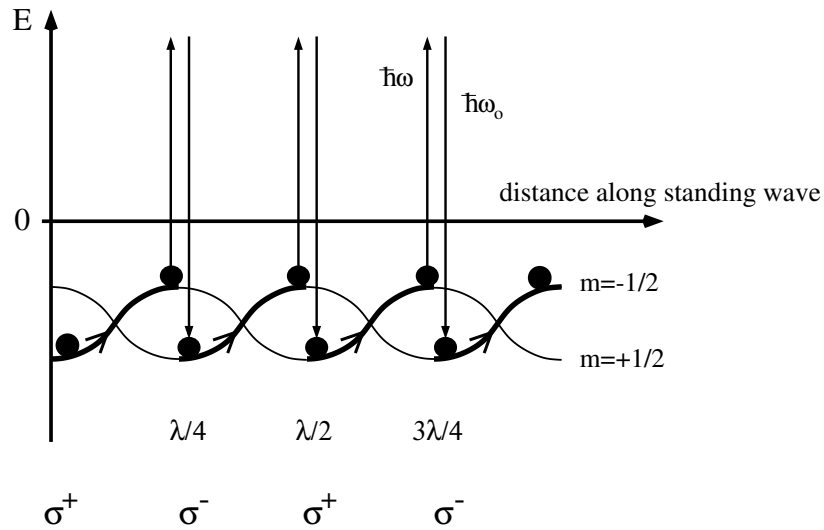


Figure 2.1: Optical potential of a $J = 1/2$ ground state in a “lin \perp lin” configuration. The arrows show the path followed by atoms being cooled in this arrangement, for explanation see the text before. Each optical pumping cycle results in absorption of light at a lower frequency than emission, thus dissipating energy to the radiation field.

A similar effect can be achieved when the laser polarization is circular. This so called “ σ^+ / σ^- ” configuration leads to a resulting polarization that is linear everywhere, but the direction rotates through an angle of 2π over one optical wavelength. Here an optical pumping is induced, since the induced atomic dipole moment always lags behind the local orientation of the polarization. For more details see [Dal89, Met94].

2.4.4 Cooling below the Doppler limit in blue-detuned molasses

One of the disadvantages of red-detuned molasses is the fact that the atoms emit a lot of spontaneous photons, which can be re-absorbed by other atoms, leading to a repulsive interaction and thus limiting the achievable density. In blue-detuned molasses cooling one does not face such a problem, since the atoms also possess states which are decoupled from the light field, thus reducing the scattering rate. Therefore blue-detuned molasses cooling is also called “gray” or “dark”-molasses cooling [Boi95]. The time an atom spends in the non-coupling state is inversely proportional to the square of its momentum p , thus part of the atomic sample is trapped in the dark state with low momentum.

Since a decoupled state is required, a blue-detuned molasses cooling process works only on a $J \rightarrow J' = J - 1$ or $J \rightarrow J' = J$ transition. The principle of blue-detuned molasses cooling is similar to the one given for a “lin \perp lin” configuration in the case of red-detuning and described

for a 1 dimensional “lin \perp lin” light field in Fig. 2.2 ¹. The Sisyphus effect arises from the ve-

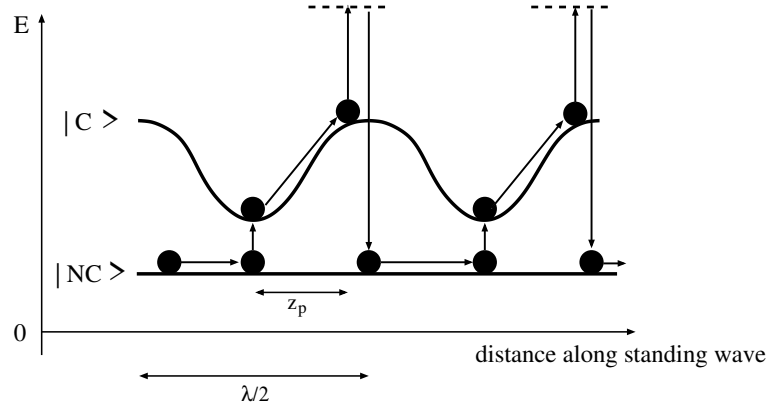


Figure 2.2: *Illustration of blue-detuned molasses cooling. The population is transferred from $|NC\rangle$ to $|C\rangle$ via motion-induced coupling primarily at the potential minima. Before being optically pumped back to $|NC\rangle$ after a distance z_p , the atom loses kinetic energy by climbing the potential hill.*

locity induced non-adiabatic transition of atomic population from the non-coupling state to the coupling state, while the atom is traveling along the laser beam axis. Assume the atom populates a coupling state $|C\rangle$ and is climbing the potential hill, its motion gets damped. With highest probability at the hilltop it will be pumped into the non-coupled state $|NC\rangle$, after traveling the distance z_p , as indicated in Fig 2.2. After repeated cycles the atomic motion is efficiently damped, the slower the atomic motion becomes, the longer the atoms stay in the non-coupling state. Therefore the friction coefficient is below the corresponding value in red-detuned molasses cooling. For more details see [Wei94].

Conclusion

With both cooling schemes a temperature on the order of some T_{rec} can be achieved. Nevertheless red-detuned molasses cooling has some disadvantages, caused by the fact, that atoms are pumped into states, which are most strongly coupled to the molasses light field. Therefore the photon scattering rate is much higher as compared to the case of blue-detuned molasses cooling, which results in a higher heating rate due to the random transfer of photon recoils. The presence of a non-negligible photon scattering rate also limits the density due to photon re-absorption. Additionally, the presence of a significant fraction of excited atoms as well as the fact that the atoms are pumped into upper ground state sublevels, opens the door for heating processes due to inelastic collisions.

In the case of blue-detuned molasses cooling atoms primarily populate ground state sublevels which are decoupled from the light field resulting in a reduction of photon scattering. Hence the

¹Since in 3 dimensions one can't distinguish between “lin \perp lin” and “ σ^+/σ^- ” configuration, this differentiation is not made here.

strength of interaction between the atoms such as photon re-absorption and short-range resonant dipole-dipole interaction is reduced and higher atomic densities can be reached. Additionally, it is a quality of this process that the decoupled state is the lowest hyper-fine ground state and only a negligible fraction of the atoms populates excited states, therefore one circumvents heating processes due to inelastic collisions.

The typical temperature realized in blue-detuned molasses ($T_{bm} \simeq 5 \times T_{rec}$) is below the temperature achievable in red-detuned molasses cooling ($T_{rm} \simeq 10 \times T_{rec}$), because of the advantageous balance between cooling and heating effects in a blue-detuned molasses configuration.

In our experiment we combined both techniques: A red-detuned molasses period, which also utilizes “Doppler”-cooling effects, “pre-cools” the atoms and “hands over” the atomic sample to a blue-detuned molasses sequence to reduce the temperature further and to allow for higher densities.

In three-dimensional experiments, where one can no longer distinguish between “lin \perp lin” and “ σ^+ / σ^- ” configuration, the intensity and polarization gradients experienced by the atoms can change dramatically during the diffusive atomic movement through the molasses. As it turned out in various experiments i.e. with Rubidium or Cesium, the cooling scheme works even more efficient than expected from the 1 dimensional model [Sal90, Kas92, Dre94, Sin95].

In the presence of a magnetic field B polarization-gradient cooling does not work efficiently any more. The detrimental effect of a magnetic field is caused by the competition between Larmor precession and the alignment of the atomic dipole due to optical pumping. The final total kinetic energy will be on the order of the magnetic energy $\mu_B B$ [Ada96].

Chapter 3

Experimental prerequisites

In this chapter different selected requirements for long time storage of neutral atoms in an optical dipole potential are explained. After introducing the relevant parameters about the atomic systems of Lithium and Cesium, the principles of the source of cold and dense atoms, the magneto optical trap [Raa87] are given. The middle part of this section will introduce the vacuum system, the magnetic field setup, and the CO₂-laser system. Finally the most frequently used detection methods are presented and the control system of the experiment is briefly described.

3.1 The Lithium atom

Lithium (Li) is the lightest alkali atom. It can be found naturally in two isotopes. The bosonic ⁷Li (abundance of 92.5 %) with nuclear spin $I=3/2$ and total spin of $F=I \pm S=1; 2$ and the fermionic ⁶Li (abundance of 7.5 %) with nuclear spin $I=1$ and total spin of $F=I \pm S=1/2; 3/2$. Here the bosonic ⁷Li is considered, since in our experiment we are working with this isotope exclusively.

Like all alkalis Lithium has only one valence electron, its ground state is $2^2S_{1/2}$. The relevant part of the level scheme for laser cooling, the so called *D2* line, is shown in Fig. 3.1. The hyperfine structure splitting in the ground state is 803.5 MHz, the hyperfine structure splitting of the excited state $2^2P_{3/2}$ is in total only 18.4 MHz and not resolved in our experiment, since it is on the order of the natural linewidth $\Gamma_{Li} = \tau_{Li}^{-1} = 2\pi \times 5.87$ MHz. The natural lifetime τ_{Li} of the excited state is 27 ns. The small hyperfine structure splitting of the excited state is a peculiarity of Lithium. The level system can be regarded as a Λ -like system, with two ground states and one excited state. Optical pumping between the two ground states $F = 1$ and $F = 2$ is very likely. Since a closed transition is needed for magneto-optical trapping, two cooling lasers of almost equal intensity are needed.

Due to its light mass (7 a.u.) the ratio of recoil temperature $T_{rec} = \hbar^2 k_{Li}^2 / (M_{Li} k_B) = 6 \mu\text{K}$ and Doppler temperature $T_{dop} = \hbar \gamma_{Li} / k_B = 140 \mu\text{K}$ is relatively small. Hence polarization-gradient

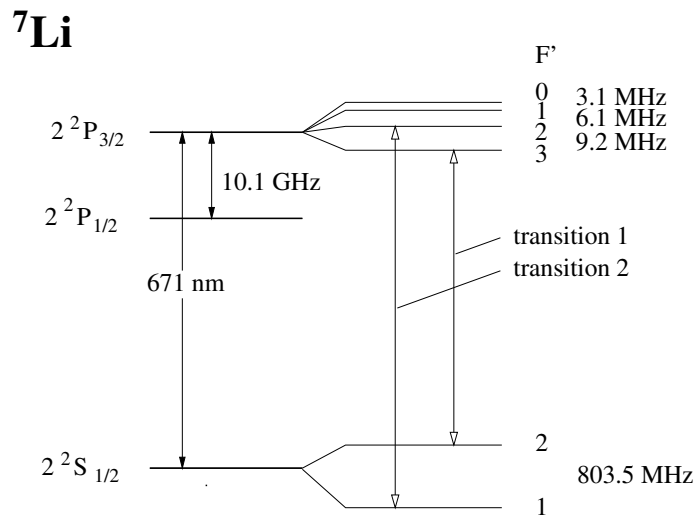


Figure 3.1: Relevant part from the level scheme of ${}^7\text{Li}$. The arrows show the transition used for trapping in the MOT, namely ${}^2S_{1/2}, F=2 \rightarrow {}^2P_{3/2}, F'=3$ and ${}^2S_{1/2}, F=1 \rightarrow {}^2P_{3/2}, F'=2$.

cooling will not work efficiently.

3.2 The Cesium atom

Cesium (Cs) is the heaviest stable alkali element. In nature only a bosonic isotope ${}^{133}\text{Cs}$ occurs with nuclear spin $I_{Cs}=7/2$. Its ground state is a $6^2S_{1/2}$ state.

The relevant level scheme is given in Fig. 3.2. The natural lifetime of the excited state $6^2P_{3/2}$

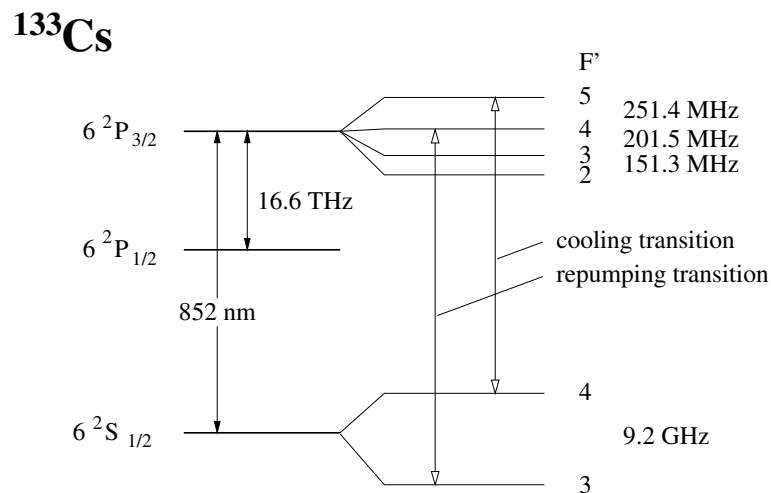


Figure 3.2: Relevant part from the level scheme of ${}^{133}\text{Cs}$. The arrows show the transition used for cooling and repumping in the MOT.

is $\tau_{Cs}=30$ ns, the corresponding linewidth $\Gamma_{Cs} = \tau_{Cs}^{-1} = 2\pi \times 5.3$ MHz is almost the same as for Lithium. But the ground state hyperfine structure splitting of 9.2 GHz is large compared to the one of Lithium as well as the hyperfine structure splitting of the relevant levels ($F'=4$ and $F'=5$) in the excited state of 251.4 MHz. Here the “closed” cycle for operating a MOT is found in the $F = 4 \rightarrow F' = 5$ transition. Since off-resonant pumping via the $F = 4 \rightarrow F' = 4$ transition has a relative probability of 0.001, only a weak repumping beam, resonant at $F = 3 \rightarrow F' = 4$ is required to pump the atoms back into the cooling cycle.

The Doppler temperature of Cs is $T_{dop} = \hbar\gamma_{Cs}/k_B=130$ μ K. Due to its large mass of 133 a.u., its recoil temperature is $T_{rec} = \hbar^2 k_{Cs}^2/(M_{Cs} k_B)=0.2$ μ K and therefore Cs an excellent candidate for polarization-gradient cooling techniques.

3.3 Radiation pressure trap

So far only the mechanism of far detuned light interacting with atoms has been considered. In this section the interaction of near resonant light with atoms in principle is described. Information about the magneto optical trap laser systems used in our experiment is given in detail by [Web00, Nil99, Sch98a] and therefore not introduced in this work.

A magneto optical trap (MOT) is a radiation pressure trap and hence based on the spontaneous scattering force.

3.3.1 Spontaneous scattering force

This force arises from subsequent cycles of absorption and spontaneous emission of resonant photons and the momentum transfer connected to these processes. Therefore two conditions have to be fulfilled: a closed optical transition is needed to ensure that many cycles of absorption and spontaneous emission are possible. Second, the interaction time of the atoms with the light has to be long compared to the natural lifetime τ of the excited state.

To illustrate the mechanism of momentum transfer from a light beam to an atom consider a two-level atom. The energy gap between the ground state and excited state is $\hbar\omega_0$. Assume the atom is in resonance with a laser at frequency $\omega \simeq \omega_0$, it is excited by absorbing a photon, whose momentum $\hbar\vec{k}$ is transferred to the atom. During the spontaneous decay the atom emits a photon of momentum $\hbar\vec{k}'$, where in general $\vec{k} \neq \vec{k}'$. After n cycles the momentum $n \times \hbar\vec{k}$ in the direction of the laser is transferred to the atom, whereas the total momentum transfer by the emitted photons averages to zero $\langle \hbar\vec{k}' \rangle = 0$, since the spontaneous emission of photons is isotropic. Therefore a net force in the direction of the laser beam is exerted on the atom. The averaged momentum transfer of one cycle is:

$$\Delta\vec{p}_{spont} = \langle \hbar\vec{k} - \hbar\vec{k}' \rangle = \langle \hbar\vec{k} \rangle - \langle \hbar\vec{k}' \rangle = \hbar\vec{k}. \quad (3.1)$$

The force exerted on an atom is thus given by the rate of absorption multiplied with the averaged momentum transfer:

$$\vec{F}_{spont} = \hbar \vec{k} \times (\text{rate of absorption}). \quad (3.2)$$

For the two level atom, which is a good approximation for our experiments, one obtains:

$$\vec{F}_{spont} = \hbar \vec{k} \times \gamma \frac{S}{1 + S + \left(\frac{\delta}{\gamma}\right)^2}, \quad (3.3)$$

where $\gamma = 1/(2\tau)$ denotes the half natural linewidth, $S = I/I_{sat}$ is the saturation parameter containing the saturation intensity $I_{sat} = 2\hbar\omega_0^3\gamma/(12\pi c^2)$, and $\delta = \omega - \omega_0 + \vec{k}\vec{v}$ is the detuning from resonance ω_0 , where \vec{v} is the velocity of the atom.

Now consider an atom placed in two counter-propagating laser beams, whose frequency is slightly below the atomic transition ω_0 . Due to the Doppler shift the atom preferably absorbs a photon from the laser counter-propagating to its own motion. Therefore the atomic motion in the direction of the light beams is damped. This cooling mechanism is called ‘‘Doppler cooling’’. It relies on momentum transfer by photon scattering, in contrast to the sub-Doppler cooling mechanism introduced in the previous chapter. Here the maximum friction coefficient is $\beta_{dop} = \hbar k^2/2$. The temperature achieved with this process is called ‘‘Doppler temperature’’ T_{dop} :

$$T_{dop} = \hbar\gamma/k_B. \quad (3.4)$$

It is limited by the random emission of the photons and therefore in general higher than the recoil temperature T_{rec} discussed in the previous chapter. Since all alkalis have approximately the same natural linewidth, their Doppler temperature is on the same order, e.g. for Cesium T_{dop} is 130 μK and for Lithium 140 μK .

3.3.2 Magneto optical trap

First realized by Raab et al. [Raa87], the magneto optical trap became a widely used tool for various experiments, where a cold and dense sample of neutral atoms is needed. The standard configuration consists of three orthogonal counter-propagating pairs of laser beams and a pair of anti-Helmholtz coils, which produce an axially symmetric quadrupole field. A schematic drawing of a magneto optical trap (MOT) is shown on the right hand side in Fig. 3.3. The magnetic field induces a spatially varying Zeeman splitting of the atomic sublevels. According to the selection rules of dipole transitions the laser beams are circularly polarized, such that they push back an atom moving out of the center and experiencing a Zeeman shift. In the center the magnetic field vanishes and the net force cancels out. The atoms are collected in a small volume of typically a

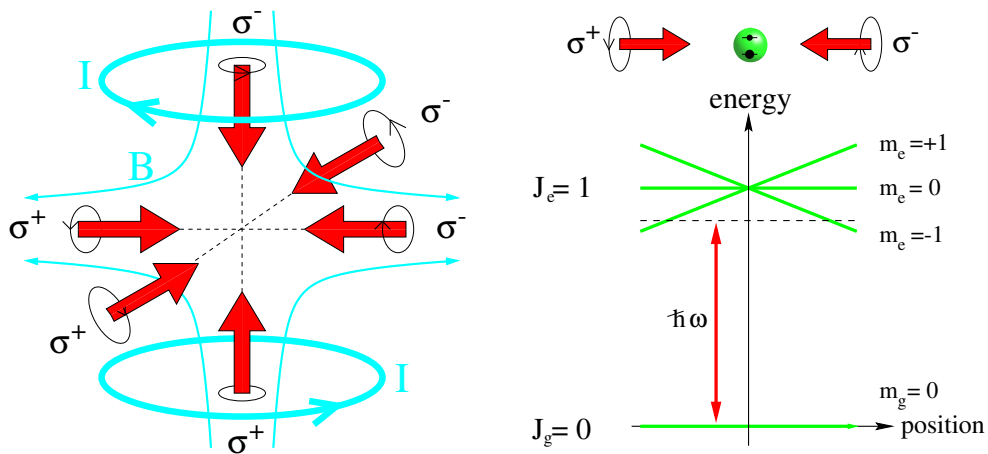


Figure 3.3: **Left-hand side:** schematic drawing of a magneto optical trap . **Right-hand side:** level splitting of a two-level atom in the field of two counter-propagating red-detuned laser beams.

few mm^3 in the center of this configuration. The principle of the space dependent force is shown on the left hand side of Fig. 3.3. Upon entering the intersection region of the MOT beams an atom is captured, if its initial velocity is smaller than the capture velocity v_c , which is about 25 m/s in the case of Cesium and about 45 m/s in the case of Lithium. The trap can efficiently be loaded from the low velocity tail of an effusive atomic beam, using a ‘‘Zeeman slower’’ [Met94]. Here the atoms are decelerated by an additional laser beam, counter-propagating to the atomic beam. In our experiment the actual source of the atoms is an oven, located several 10 cm from the MOT. On their way along the x -axis from the oven to the center of the MOT, the atoms travel through a decreasing longitudinal magnetic field. The field gradient is designed in a way that the Zeeman shift always compensates for the Doppler shift,

$$\vec{k}(x) \vec{v}(x) = -\vec{\mu} \vec{B}(x). \quad (3.5)$$

Therefore the atoms are at any position in resonance with the slowing beam and hence constantly decelerated until they reach the MOT. By this slowing process the MOT-loading flux is increased, since atoms being initially faster than v_c are decelerated by the Zeeman-slower to the capture velocity of the MOT. The slowing process and the experimental realization in our apparatus for the case of Lithium is explained in detail in [Eng97] and in appendix B.3, and for Cesium the basic parameters of the slowing process are given in appendix B.4.

3.4 Vacuum system

During this Ph.D. thesis it became clear that the former vacuum system would not meet the requirements needed for the present and future experiments. Beyond several minor problems we had serious ones, such as no sufficient optical access for the lasers and detection devices, and a

pressure that was two orders of magnitude too high, so that the storage times were background gas limited to typically 2 s. Estimations about the time scale of the experiments we planned showed clearly we would need at least a 15 times longer storage time. Hence the vacuum system was completely rebuilt and meets now the required preconditions.

The entire vacuum system consists of a central part, and three auxiliary sections, as shown in Fig. 3.4. In the following the “main chamber” specifies the central part of our apparatus, where the atomic traps are operated. Closely hooked on it is the pumping section, realized by the upright tubus to the right of the main chamber (Fig. 3.5). Two atomic beam sections are also mounted to this central unit, connecting it with the Lithium oven, respectively Cesium oven. This new apparatus is already described in detail in [Web00], here only the most important features are introduced and some supplementary information is given.

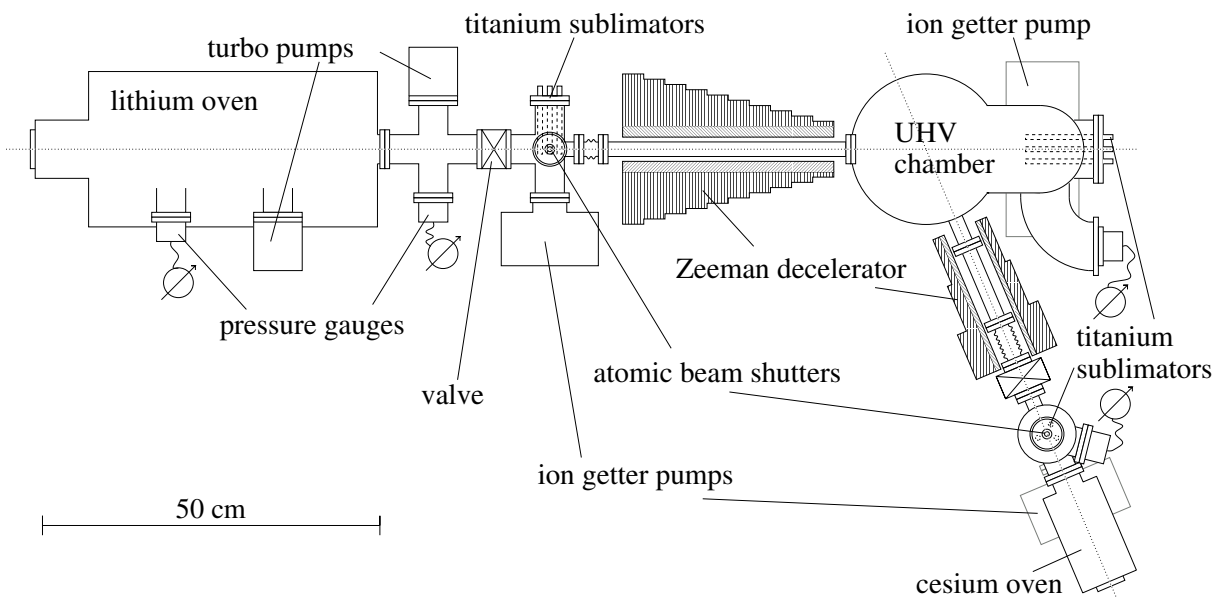


Figure 3.4: *Top view on the entire vacuum system (true to scale).*

3.4.1 Main vacuum chamber and pumping unit

The main vacuum chamber is the heart of our experiment. Inside this chamber the magneto optical trap and quasi-electrostatic trap are implemented. Fig. 3.5 shows the new central vacuum chamber with the pumping section, made of stainless steel (type 316LN). On the upper part are mounted 24 short tubes with CF[©]-flanges in different diameters. They are mainly used as laser ports and for detection purposes, for which large spatial angles are wanted. On the very top of the device one sees the large DN100 flange of the main detection viewport. This port is also used for the vertical MOT beams. This flange has a counterpart at the bottom of the chambers top part.

In order to reach much better pressure conditions we followed two basic ideas: use larger pumping speeds and reduce the contamination due to out-gassing and leakage rates, since the final pressure is given by the equilibrium of pumping speed and contamination rate. Because all connectors are CF[®]-flanges, providing leakage rates below 10^{-11} mbar l/sec, the out-gassing rate of the chambers inner surface dominates the contamination rate. The final out-gassing rate of the material is a question of duration and temperature of bake out. Here the specification of the anti-reflective coating on the Zinc-Selenite viewports limited us to a maximum bake out temperature of 200° C. During bake out this temperature was maintained for 6 days. After such a procedure the expected out-gassing rate of the total inner surface can be estimated as 2×10^{-8} mbar l/s.

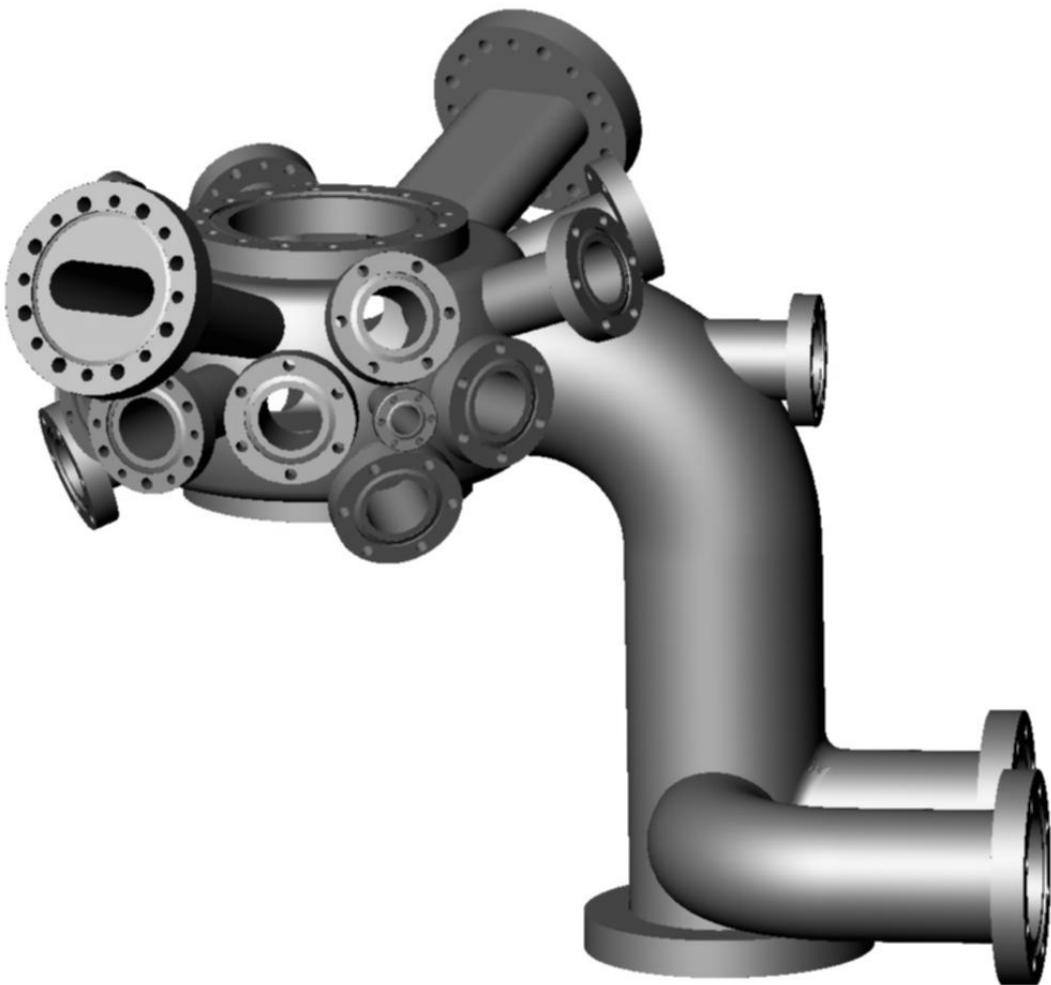


Figure 3.5: *The new ultra-high vacuum chamber.*

The pumping speed was mainly increased by the use of Titanium sublimation pumping in addition to a 60 l/s ion-getter pump, which is mounted to the very low end of the tubus in the right part of Fig. 3.5. Titanium sublimation pumping is based on the getter properties of Titanium.

The pumping speed per cm^2 Titanium coated surface at room temperature varies for the relevant gases between 4 l/s in the case of N_2 and 11 l/s for CO_2 (note: methane and noble gases are NOT pumped by the Titanium film, they are only pumped by the ion-getter pump). Hence the total pumping speed is only a matter of Titanium covered surface. In our apparatus the Titanium filaments are placed in the middle part of the tubus. When activated, Titanium covers the complete inner surface of that tubus, including the upper bow, where the tubus is mounted to the main chamber. From the covered area size one calculates a total pumping speed of 3270 l/s for N_2 . Taking into account the finite conductance of the opening (10 cm in diameter) between the main chamber and the tubus, the resulting effective pumping speed in the main chamber is 710 l/s in the case of N_2 . We expected to achieve a pressure of $p_0 \simeq \frac{2 \times 10^{-8} \text{ mbar l/s}}{710 \text{ l/s}} = 2.8 \times 10^{-11}$ mbar. This value is consistent with the actual pressure measured in our chamber of roughly 2×10^{-11} mbar. This excellent vacuum allows for the long storage times we are aiming for.

Since the contamination rate of the chamber is small, the Titanium layer will not be saturated for months. Hence the filaments are activated only once at the ending of the bake out. For activation we run a current of 50 A for 30 minutes through the Titanium wires, causing the evaporation of Titanium. After that procedure, the final pressure is reached one day later and maintained for months.

At the two ports in the lower right, the current feedthroughs of the Titanium filaments and the pressure gauge are mounted.

3.4.2 Atomic beam section

Two separate ovens in which Lithium, respectively Cesium, are evaporated serve as sources for the trap loading atomic beams. In order to reach sufficient trap loading flux, due to its low vapor pressure the temperature of the Lithium oven usually is 450°C . Cesium has a higher vapor pressure, hence 140°C oven temperature is enough. Under these typical operation conditions the pressure in both oven chambers is on the order of 10^{-6} mbar [Nes63]. Each oven is connected by a tube with some small internal apertures to the main chamber. By the apertures a fine atomic beam is formed and the reduced conductance of the tubes and apertures allows for a pressure gradient between the main chamber and the oven by additional pumping of the atomic beam sections.

In the case of *Lithium* a double differential pumping section is realized by implementing a 60 l/s turbo pump in the first and a 30 l/s ion-getter pump plus Titanium sublimation pumping in the second section. That way we do not see any influence on the pressure in the main chamber by the Lithium oven. The designed pressure gradient of this differential pumping section is 2×10^{10} . The distance from the oven to the center of the chamber is about 95 cm.

In the *Cesium* atomic beam section only one differential pumping stage is realized by a 25 l/s ion-getter pump in addition to Titanium sublimation pumping. That way the Cesium oven could be

located closer to the main chamber (distance to the center about 55 cm) yielding a larger spatial angle for loading of the trap. The designed pressure gradient of the Cesium differential pumping section is 7×10^7 . As it turned out in recent experiments the pressure in the main chamber is increased by a factor of 3 if the Cesium oven is operated under extremely high temperatures of about 170°C , where the Cesium vapor pressure in the oven is about 5×10^{-3} mbar.

Both atomic sections are equipped with mechanical atomic beam shutters so that we can control the loading fluxes separately. In each section valves are implemented to physically separate the main chamber from the oven sections. Thus one does not have to break the vacuum in the main chamber when opening one of the ovens.

In Fig. 3.4 a true to scale sketch of the complete apparatus is shown.

3.4.3 Magnetic fields

In our apparatus various separate magnetic fields are playing together. Namely the axial symmetric quadrupole field, generated by a pair of coils in anti-Helmholtz configuration, and compensation fields in three dimensions, which are realized by three pairs of large Helmholtz coils. Finally the solenoids for the magnetic fields used in the Zeeman-slower section of the Lithium and Cesium atomic beam sections. Changing one of those fields more or less influences the shape of the total field, hence the different magnetic fields have to be well tuned among each other.

To reduce local inhomogeneities only non-magnetic materials in the area of the main chamber are used. For example, exclusively non-magnetic stainless steel, type 316LN with $\mu \leq 1.005$, is used for the chamber itself and its mounts. Even the screws used for the viewports are made of this material.

For transferring the atoms from the magneto optical trap into the dipole trap it is essential to turn off the *quadrupole field* of the MOT quickly. Therefore the field coils are designed as small as possible (16 cm in diameter) and are mounted as close as possible (8 cm to central plane) to the main vacuum chamber, in order to keep the total magnetic field energy small for the desired gradient of 25 G/cm along the symmetry axis of the quadrupole field. During normal operation a current of 30 A is running through the 67 windings of each coil. The windings are supported by a water cooled brass-ring, which has a radial slit in it to suppress inductive currents inside this ring when turning off and on the current. The switching is performed by power MOS-FET's (Thomson, STE53NA50) and the induction voltage is controlled and limited to 300 V by high power transient voltage suppressor diodes (Protek Devices, 15KPA100/200). This allows for turning off the MOT field within $300 \mu\text{s}$ (100% to 10% of B_0). The nice matching of the calculated MOT field with its measured contour is shown in appendix B as well as the course of the field gradient. Additionally a coil of 35 turns is wound around each of the main MOT coils. This extra pair of coils can be used to increase the field gradient or to add a field in the vertical direction along the symmetry axis of the quadrupole.

Since for polarization-gradient cooling methods total control of the magnetic field at the trap center is needed, we use 3 independent pairs of *coils to compensate* non-controllable fields such as the earth magnetic field, tails of the Zeeman-slower fields inside the main chamber or the field of ion-getter pumps. These compensation coils are operated in Helmholtz configuration. The windings are supported by a large box (dimension of $1.60 \times 1.10 \times 0.80$ m), centered on the main chamber. This way a very homogeneous field is realized and we do not get any influence on the field compensation during the turn-down of the MOT field. The maximum current of 5 A through the 2×96 windings of each pair generates a field of about 4 G. To sensitively equalize the field at the trap center we used a dark resonance method that is explained in detail in appendix A. The calculated shape of these compensation fields is shown in appendix B.2.

The solenoids of the *Zeeman-slower fields* are shown in Fig. 3.4. To reduce their influence on the field at the trap center they are realized as “decreasing field slowers” [Tho94, McA95], in a way that the ending tail of the slowing field fits smoothly into the quadrupole field of the MOT. The *Lithium* Zeeman-slower solenoid has a total length of 32 cm and consists of 10 independent segments, allowing for fine tuning. The maximum magnetic field strength is 595 G, corresponding to an initial resonance velocity of 600 m/s. Detailed description of the Lithium Zeeman-slower configuration is given in [Eng97], and the nice matching of the calculated with the measured shape of the current field is shown in appendix B.3.

In the case of *Cesium*, the calculated design of the longitudinal magnetic field inside the slowing section is given in Fig. B.9. The maximum field strength is 117 G, resulting in a maximum resonance velocity of about 160 m/s, giving us sufficient trap loading flux. Therefore we could keep the setup compact, the total length of the solenoid is 20 cm only. Due to large saturation broadening of the Cesium slowing laser beam, the shape of the magnetic field had not to be precisely adjustable and therefore the slowing field consists only of three independent coils. A measurement of this field was not taken due to the architecture of the apparatus. The nice agreement of the actual Lithium Zeeman-slower field with the calculations leads to the well founded assumption, that in the case of Cesium the fields match nicely as well. This assumption is confirmed by the enhancement of the loading flux by a factor of about 5, as predicted when using the Zeeman-slower in contrast to decelerating the atoms only in the MOT fringe fields. In appendix B.4 the associated beam properties are detailed. The basic information on the Cesium Zeeman-slower is also given in [Web00].

3.5 CO₂-laser system and resulting trap parameters

In the present section the basic parameters of the CO₂-laser system are displayed. Starting with the spatial intensity distribution of the trapping beam and the associated parameters of the trapping potential, the basic technical data about the laser we are using is given. Then an overview on the optical setup is presented. The section ends with the results of the mechanical measurement of the beam waist.

This chapter gives only brief information about the CO₂-laser setup, in [Web00, Nil99] a more detailed description can be found.

3.5.1 Spatial intensity distribution of the trapping beam

The spatial intensity distribution of a focused Gaussian beam with power P propagating along the z -axis is described by

$$I_{GB}(r, z) = \frac{2P}{\pi w^2(z)} \exp\left(-2\frac{r^2}{w^2(z)}\right), \quad (3.6)$$

where r denotes the radial coordinate. The $1/e^2$ intensity radius $w(z)$ depends on the axial coordinate z via

$$w(z) = w_0 \sqrt{1 + \left(\frac{z}{z_R}\right)^2}. \quad (3.7)$$

The minimum radius w_0 is called “beam waist”, $z_R = \pi w_0^2/\lambda$ denotes the “Rayleigh range” and λ the wave length of the laser light.

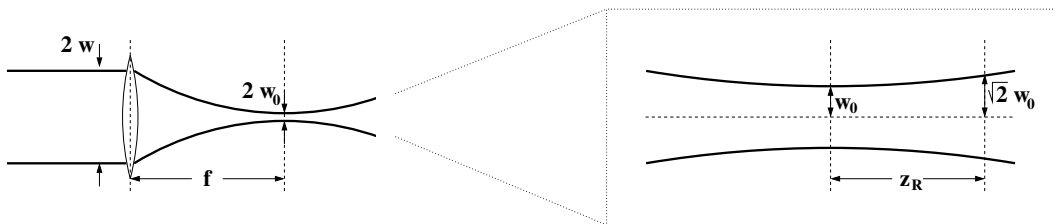


Figure 3.6: *Illustration of Gaussian beam parameters.*

Using a lens with focal distance f , for a given waist w the Gaussian beam can be focused onto a minimal waist w_0 of [Sie86]

$$w_0 = \frac{\lambda f}{\pi w}. \quad (3.8)$$

This is only valid for a pure Gaussian beam with a TEM₀₀ mode. The output beam of a real laser usually contains some additional modes with larger transverse extension compared to the TEM₀₀ mode, causing an enlarged minimum waist. The so called M^2 factor [Sie86] takes this effect into

account. The focal spot of a non-Gaussian beam is by a factor of M^2 enlarged compared to a beam with pure TEM₀₀ mode under the same conditions. When calculating the minimum waist, Eq. 3.8 has to be modified:

$$w_0 = M^2 \frac{\lambda f}{\pi w}. \quad (3.9)$$

3.5.2 Shape and depth of the trapping potential

From the intensity distribution one can derive the optical potential $U(r, z) \propto I_{GB}(r, z)$ using Eq. 2.13. Hence a particle with static polarizability α_{static} experiences the potential

$$U(r, z) = \frac{\alpha_{stat}}{2\epsilon_0 c} I_{GB}(r, z) = \frac{\alpha_{stat}}{\epsilon_0 c} \frac{P}{\pi w^2(z)} \exp\left(-2\frac{r^2}{w^2(z)}\right), \quad (3.10)$$

where $w(z)$ is given by Eq. 3.7 and Eq. 3.8. Since the atoms trapped in a QUEST populate the ground state, α_{stat} denotes the ground state polarizability. The maximum trap depth U_0 is given by

$$U_0 = |U(r=0, z=0)| = \frac{\alpha_{stat}}{\epsilon_0 c} \frac{P}{\pi w_0^2}. \quad (3.11)$$

The Rayleigh range z_r is larger than the beam waist w_0 by a factor of $\pi w_0/\lambda$. Therefore the optical dipole potential in the radial direction is much steeper as compared to the axial direction. To provide stable trapping, the gravitational force has to be smaller than the confining dipole force. Focused beam traps are therefore usually aligned horizontally, so that the strong radial force minimizes the perturbing effects of gravity.

If the thermal energy of the atomic ensemble is much smaller than U_0 , the extension of the atomic cloud is radially small compared to the beam waist and axially short compared to the Rayleigh range. For that case, the optical dipole potential can be well approximated by a cylindrically symmetric harmonic oscillator potential:

$$U(r, z) \simeq -U_0 \left[1 - 2 \left(\frac{r}{w_0} \right)^2 - \left(\frac{z}{z_R} \right)^2 \right]. \quad (3.12)$$

The oscillation frequencies of a trapped atom of mass m are given by $\omega_r = \sqrt{4U_0/mw_0^2}$ in the radial direction, and by $\omega_z = \sqrt{2U_0/mz_R^2}$ in the axial direction.

In our setup the CO₂-laser is focused to a waist of $108 \mu\text{m}$ ¹ and the actual power is 30 W. With the static polarizability of the Cesium ground state $\alpha_{stat}^{Cs} = 66.3 \times 10^{-40} \text{ C m}^2/\text{V}$, respectively of the Lithium ground state $\alpha_{stat}^{Li} = 27.0 \times 10^{-40} \text{ C m}^2/\text{V}$ [Wea88], the trap depth U_0/k_B

¹The value of $w_0 = 108 \mu\text{m}$ originates from the measurement of the radial trap frequency of Cesium atoms in our quasi-electrostatic trap (see section 4.2). The value is considered to be the most accurate value we have on w_0 . The designed value is $97 \mu\text{m}$. From a measurement using a sharp edge that was slowly moved in radial direction into the beam while monitoring the fractional power, we got a fitted value of $90 \mu\text{m}$ (see section 3.5.4).

calculated according to Eq. 3.11 for Cesium is $118 \mu\text{K}$ and for Lithium $48 \mu\text{K}$. The associated trap frequencies for Cesium are $\omega_r^{Cs} = 2\pi \times 254 \text{ Hz}$ and $\omega_z^{Cs} = 2\pi \times 8.1 \text{ Hz}$. The ones for Lithium are calculated to $\omega_r^{Li} = 2\pi \times 717 \text{ Hz}$ and $\omega_z^{Li} = 2\pi \times 23 \text{ Hz}$. A measurement of the radial frequency ω_r^{Cs} of Cesium is given in section 4.2.

The following table summarizes the values of the static polarizability α_{stat} of the relevant states for Cesium and Lithium. The numbers for the ground state are taken for both species from [Wea88], the ones of the Cesium excited state sublevels from [Mar66] and the ones of the Lithium excited state sublevels from [Win92].

State	α_{stat} of Cs [$10^{-40} \text{ C m}^2/\text{V}$]	α_{stat} of Li [$10^{-40} \text{ C m}^2/\text{V}$]
$S_{1/2}, m_j = \pm 1/2$	66.3	27.0
$P_{3/2}, m_j = \pm 3/2$	218.0	21.1
$P_{3/2}, m_j = \pm 1/2$	303.6	20.6

Table 3.5.2: The static polarizability α_{stat} of the $S_{1/2}$ and $P_{3/2}$ states in Cs and Li.

In Fig. 3.7 the light shift acting on the Cesium ground state and excited state is given. For trapping the atoms in the QUEST only the light shift of the ground state potential is relevant, since due to the absence of photon scattering the atoms populate the ground states exclusively. But if additionally resonant light is present (e.g. during the transfer from the MOT into the QUEST), some of the atoms populate an excited state which becomes light shifted to lower energies as well². Since the static polarizability differs for the various states, the atomic transition frequencies of the trapped atoms are shifted. This behaviour has to be taken into account when transferring the atoms into the QUEST (see section 5.2 and 5.3).

Gravitational effect

An atom in the quasi-electrostatic trap not only experiences the dipole force but also the gravitational force. Due to gravitation the optical dipole potential loses its symmetry, the potential depth in vertical direction (y -axis) is smaller by a term of $mg y$. Fig. 3.8 shows the influence of gravitation in the optical dipole potential in vertical direction, the effective potential depth for Cesium is therefore $U_0^{eff}/k_B = 106 \mu\text{K}$. In the case of Lithium the influence of gravitation on the effective trap depth is negligible due to the small Lithium mass.

²As mentioned in the previous chapter, the potential of the quasi-electrostatic trap is attractive for all atomic states.

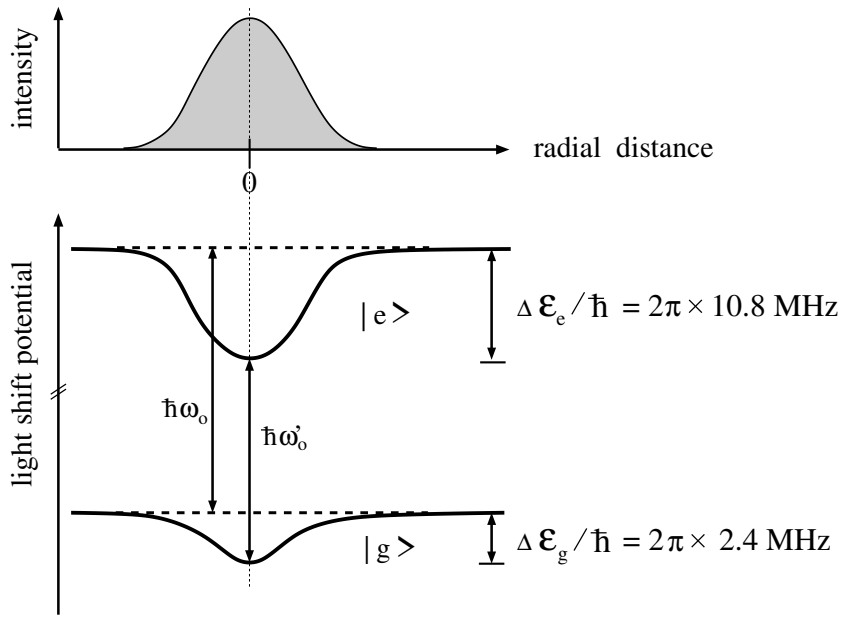


Figure 3.7: Illustration of the light shift potential in a CO_2 -laser trap. In the **upper figure** the radial distribution of the laser intensity is sketched. The **lower figure** shows the corresponding light shifts on the Cesium ground state $^2S_{1/2}$, $m_j = \pm 1/2$ potential and on the $^2P_{3/2}$, $m_j = \pm 3/2$ excited state potential. The values of the potential depth are given for a $w_0 = 108 \mu\text{m}$ focus of a 30 W CO_2 -laser beam. Note that the atomic transition frequencies of the trapped atoms are shifted to lower energies, since the excited state is more strongly shifted than the ground state. Here the light shift is given in MHz, since the influence on the atomic transition $\hbar \omega'_0 = \hbar \omega_0 - (\Delta \mathcal{E}_e - \Delta \mathcal{E}_g)$ is illustrated. The resulting maximum frequency shift corresponds in total to about $-1.6 \Gamma_{Cs}$.

The relevant potential for trapping the atoms in the QUEST is the ground state potential, its depth corresponds to $U_0/k_B = 118 \mu\text{K}$.

For Lithium the potentials follow a similar shape but are less strongly affected since the static polarizability is smaller (see Table 3.5.2).

3.5.3 CO_2 -laser parameter and optics

Laser source: The CO_2 -laser is a very energy efficient gas discharge laser at $\lambda=10.6 \mu\text{m}$. The active medium is a trimix of He (typically 70%), N_2 (typically 20%) and CO_2 (typically 10%). Mostly by radio frequency or d.c.-voltage induced discharge N_2 gets vibrationally excited. The energy is quickly transferred by inelastic collisions to the CO_2 molecules, which have an excited state at a similar energetic level. This state serves as upper laser level. By collisions with He, the lower laser level gets de-populated. For more detailed information on CO_2 -laser processes see [Eic91, Wit87].

In our experiment we are using an industrial grate CO_2 -laser with nominal cw-power of 25 W (“Synrad 48-2WS”). The actual power was measured to be 30 W, varying on a time scale of some 10 s by $\pm 5\%$, due to thermal drifts of the laser resonator. This laser is a “plug-and-play” device.

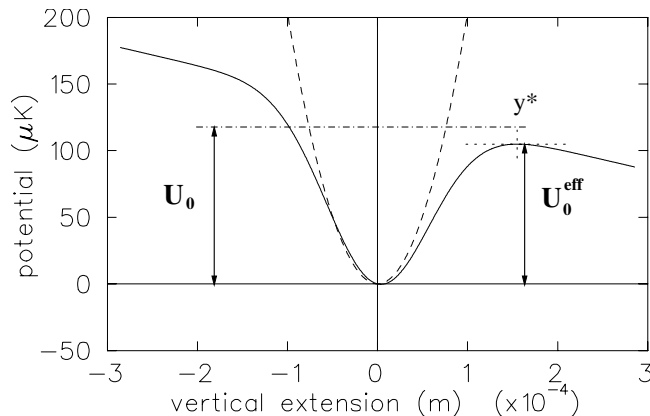


Figure 3.8: *QUEST* potential for Cs in the vertical axis under the influence of gravity. The effective potential depth U_0^{eff}/k_B is lowered to $106 \mu K$ in the case of Cesium. The location, where gravity exceeds the optical dipole force is denoted by y^* . In the case of Cesium $y^* = 140 \mu m$, in the case of Lithium the influence of gravitation on the effective trap depth is negligible due to the small Lithium mass.

The resonator is a sealed-off system with a lifetime of several thousand hours, no maintenance is needed. Our laser is radio frequency (rf) excited at 45 MHz, the rf-power can be controlled by a TTL input. This way we can comfortably turn on and off the laser, the dynamics of the discharge allows the drop from 90% to 10% of maximum intensity within $200 \mu s$.

According to the laser manual, the $1/e^2$ -intensity waist of the out-coming beam is supposed to be 1.75 mm and the M^2 value is listed with 1.2.

Optics: The optical setup contains only few elements, since each lens or mirror potentially disturbs the shape of the laser beam and causes intensity losses, which directly reduce the trap depth. The optical elements are mounted on solid sockets. This way one suppresses problems of beam pointing instabilities. Therefore also the laser itself is mounted as close as possible to the main vacuum chamber in order to keep the optical distance short. The setup of the CO₂-laser optics is sketched in Fig. 3.9. Mirror M_1 and M_2 are needed to align the initial laser beam (waist 1.75 mm) with the optical axis of the telescope ($f_1 = -50$ mm and $f_2 = 318$ mm), where the beam gets expanded to a waist of 11 mm. A third lens ($f_3 = 254$ mm) is used to focus the beam to the desired spot size of $w_0 \approx 100 \mu m$. This lens is mounted on a z-translation stage, to allow an adjustment of the focus in the axial direction. Mirror M_3 finally guides the beam into the vacuum chamber and gives us control over the focus position in the radial axes. According to Eq. 3.8 the lens system was designed with the aim to realize a sufficiently small beam waist in the center of the vacuum chamber at the given geometric conditions such as free aperture of the viewports and their distance from the center of the chamber. For the given laser and lens parameters, one calculates a final waist of $w_0 = 97 \mu m$ and a Rayleigh range of $z_R = 2.4$ mm.

All lenses and viewports are made of “Zinc-Selenite”, besides Diamond the material with the

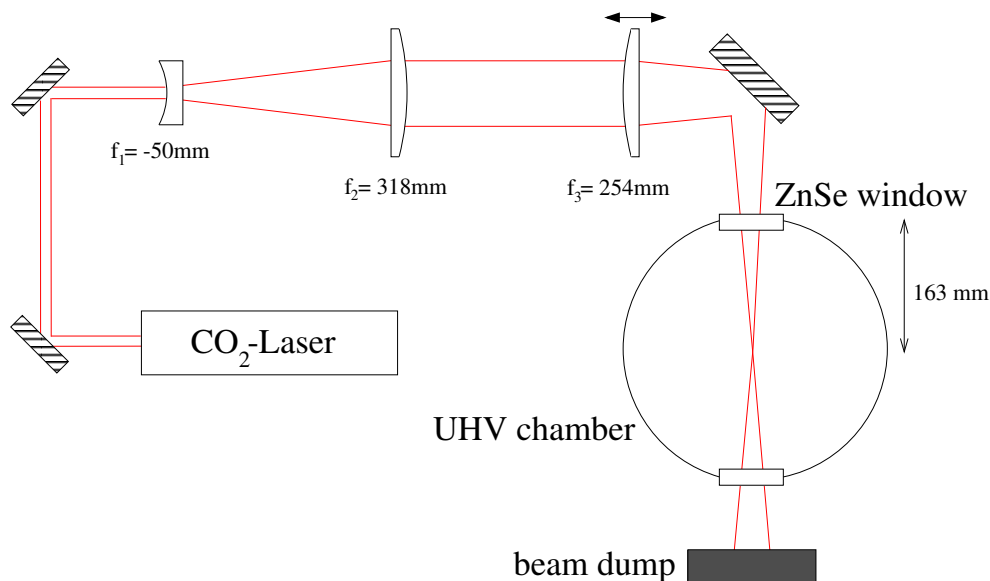


Figure 3.9: *Illustration of optical setup.*

lowest absorption coefficient at a wavelength of $10.6 \mu\text{m}$. Zinc-Selenite has an index of refraction of 2.4 at $10.6 \mu\text{m}$. Hence an anti-reflective coating is needed, because without the reflectivity is almost 17%. One of the advantages in using Zinc-Selenite optics is its transparency for visible light. That makes the adjustment of the CO_2 -laser beam much easier by using a guiding beam. The mirrors are gold-plated copper surface mirrors. They reach a reflectivity of up to 99.97%.

3.5.4 Measurement of beam waist

In order to experimentally confirm the calculated final beam waist of $97 \mu\text{m}$ we have measured the waist by using a test setup, which was a copy of the actual optical system but without the vacuum chamber. This test setup included also the Zinc-Selenite viewports.

Visualizing the intensity distribution of light at $\lambda = 10.6 \mu\text{m}$ is a nontrivial task. Most of the usual light detecting devices fail to work on $10.6 \mu\text{m}$. Appropriate photodiodes are available but are quite expensive and inconvenient to use, since they have to be cooled to the temperature of liquid Nitrogen. The method we favored to get a measure of the beam shape was to partly cover the beam profile with a sharp edge, that was slowly moved in radial direction into the beam. That was done at different axial positions around the focus. The residual total laser power was measured by a thermal power meter (Spectra Physics 407A). Assuming a Gaussian distribution in radial direction according to Eq. 3.6, a fit of an error function to the data gave a value of $w_0 = 90 \pm 10 \mu\text{m}$. The data is presented in Fig. 3.10.

The beam profile of our CO_2 -laser is transversally not purely Gaussian ($M^2=1.2$). The fitted value of $w_0 = 90 \mu\text{m}$ can be considered as a lower limit of the true waist, since higher orders of transversal modes will lead to larger focal sizes according to Eq. 3.9. Therefore the experimental

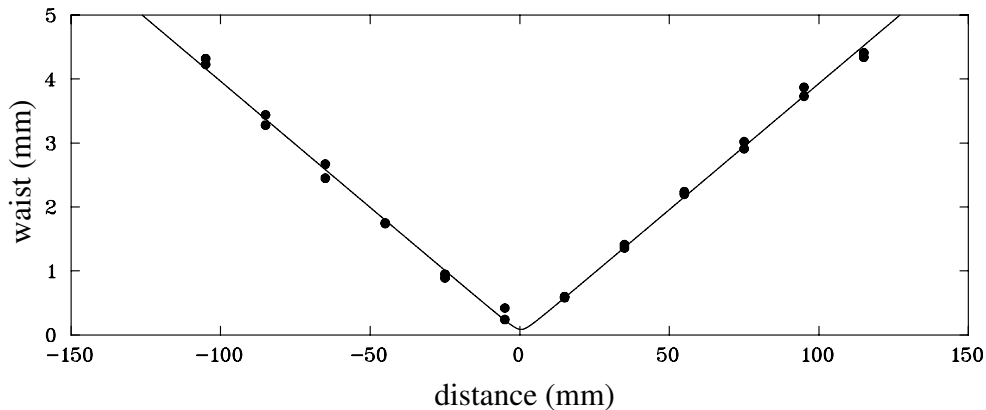


Figure 3.10: CO_2 -laser beam waist along the laser propagation axis.

value is in great accordance with the expected focal waist of $97 \mu\text{m}$.

From a measurement of the radial trap frequency, given in section 4.2, follows a waist of $w_0 = 108 \mu\text{m}$. This value is considered to be to most precise we have on w_0 and therefore it is the value used for any calculation in this thesis.

3.6 Detection methods

The most relevant parameters to characterize an atomic sample are: number of atoms, extension of the atomic cloud, its density distribution and temperature. To determine these parameters, two standard types of detection methods are employed in our experiment: fluorescence and absorption measurements. The characteristics, advantages and disadvantages of those methods are introduced in the following.

3.6.1 Fluorescence detection

The most commonly used method for detecting an atomic cloud is a fluorescence measurement, which is based on the detection of scattered light from the atomic sample. This can be done by the use of photo-multiplier tubes, photodiodes and CCD cameras. In the present work only the two latter ones are employed.

The spontaneous scattering rate for a two level atom is given by

$$\Gamma_{sc} = \gamma \frac{S}{1 + S + \left(\frac{\delta}{\gamma}\right)^2}. \quad (3.13)$$

This expression corresponds to the “rate of absorption” in Eq. 3.2. Here $\gamma = \frac{1}{2\tau}$ denotes the half natural linewidth and $S = I/I_{sat}$ the saturation parameter, $\delta = \omega - \omega_0 + \vec{k}\vec{v}$ is the detuning from resonance ω_0 . Due to the low temperature of the regarded atomic samples $|\vec{v}|$ is only a

few 10 cm/s or below, and can therefore be neglected in the detuning. Since we measured the saturation parameters generated by the Cesium and Lithium laser system [Sch98a], the scattering rate in dependence of the detuning δ is well known. Hence by knowing the solid angle of which the detected fluorescence is accumulated and taking the quantum efficiency of the photodiode and the gain of its transducer into account, we know the total amount of light emitted by the sample of atoms. Dividing by the photon energy $\hbar\omega_0$ yields the total number N of atoms. With good agreement this gauge was cross-checked by illuminating our photodiodes with a reference laser beam of well known absolute power. We gauged the CCD camera for a given exposure time and aperture by taking a fluorescence picture of the trapped atoms while measuring the fluorescence with the photodiode. The integral of the total pixel count corresponds to the total number of atoms.

As a standard procedure we monitor the number of atoms for each species in the MOT separately by using photodiodes with wavelength selective filters. The photodiodes can only be used for sufficient numbers of atoms ($\gtrsim 10^5$), otherwise electrical noise dominates the signal. To detect smaller numbers of atoms, i.e. for determination of the number of recaptured atoms in the MOT after storage in the CO₂-laser trap, the CCD camera is a better choice, since its signal to noise ratio is much better. Additionally, from the CCD picture we get information about the atomic distribution in 2 dimensions. The CCD camera we use is a commercial slow-scan camera (Spectra source, Teleris-2) equipped with a Kodak KAF-E0400, grade 1 chip. Its ultra-low readout noise and dark current rate allows for extremely long exposure time up to several seconds. Therefore atomic numbers down to a few hundreds can be detected, when captured in a MOT, where naturally fluorescence light is present.

When applying a fluorescence detection method in “ballistic expansion” measurements or by taking pictures of atoms stored in the QUEST one has to take special care. Since naturally under these circumstances no fluorescence light is present, one has to flash on the atoms with near resonant light. The duration of that flash and the detuning of the light has to be chosen properly, to make sure the initial distribution gets not disturbed by the detection flash. In these cases we typically choose a red-detuning of 5 linewidths for Lithium and 10 linewidths for Cesium to generate an optical molasses (section 2.4.2), in order to freeze out the motion of the atoms while illuminating them for a few milliseconds.

If the number of atoms is sufficient, an absorption method is in general a better choice for measurements where the atoms are not tightly confined, i.e. in the QUEST or for ballistic expansion measurements, where additionally exact time resolution is desirable.

A second disadvantage of fluorescence detection appears for large atom numbers at high densities. When the cloud gets optically dense, photons of the laser beams are mostly scattered in the outer region of the cloud and the inner regions appear darker. Hence a fluorescence measurement tends to under-estimate the actual number of atoms.

Finally, from a fluorescence measurement one can not distinguish between different atomic states.

Without using wavelength selective filters, one could not even distinguish between two different species when simultaneously illuminated with resonant light.

3.6.2 Absorption detection

Absorption detection is based on the transmission of a *weak* probe laser beam of resonant light through the cold and dense atomic sample. Here two basic methods were used: firstly, absorption imaging with an extended, resonant probe beam that projects the shadow of the cloud onto a CCD chip. Since this method does not rely on photodiode calibration, it is a more precise, independent way to determine the total number of atoms, as detailed in the following.

Secondly, pointing a focused probe beam through the center of the cloud to a photodiode. By scanning the probe beam frequency one gets information about the state distribution of the sample.

Absorption imaging

This method works only in the absence of fluorescence light. It is a good choice for detecting the atomic distribution in the QUEST or for taking ballistic expansion measurements, as long as one has sufficiently high densities. From the absorption picture one gets immediately the total number of atoms, the column density distribution, and the 2-dimensional extension of the sample. Furthermore, this method allows for excellent time resolution in ballistic expansion measurements since extremely short flash-on times down to $50 \mu\text{s}$ can be used. In addition, with the ultra low intensity of the probe beam on the order of $2 \times 10^{-3} I_0$, which corresponds to intensities of a few $\mu\text{W}/\text{cm}^2$, the atomic distribution gets quasi not disordered by the detection flash.

The procedure is as follows: Two pictures are taken. On the first one, the resonant beam passes through the cloud onto the CCD camera which records the picture. The second picture is taken under the same conditions but without the atoms. Dividing both pictures pixel by pixel yields the two dimensional column density distribution. Integrating over the divided picture leads to the total number of atoms, as detailed in appendix D. From the density distribution one can get not only the size of the atomic cloud, but also the temperature, if the trapping potential is known [Web00, Wei00].

A more precise method to determine the temperature of an atomic sample is to take a sequence of ballistic expansion measurements. Here the atoms are released from the trap and a picture of the atoms is taken after various time periods after release. Assuming a Gaussian distribution, from the evolution of the cloud size $\sigma(t)$ versus expansion time t one can determine the temperature T according to:

$$\sigma(t) = \sqrt{\sigma_0^2 + \frac{k_B T}{m} t^2}, \quad (3.14)$$

where k_B denotes the Boltzmann constant, σ_0 the initial extension, and m the mass.

Absorption measurement by use of a probe beam

To obtain quick and on-line information on the density of the atomic cloud in the MOT or their distribution in states, we used the absorption signal of a focused probe beam, propagating through the cloud onto a photodiode. Depending on the probe beam waist w_0 , one gets information on the peak column density ($w_0 < \text{cloud extension}$) or the total number of atoms ($w_0 > \text{cloud extension}$). Since this can be done while the magneto optical trap is running, one can monitor on-line the distribution of states, by scanning the probe laser. For demonstration a typical picture is shown in Fig. 3.11. The intensity of the probe beam has to be low ($I < I_0/10$), to make sure the atoms are not pushed out of the trap or get pumped by the probe beam. We usually used this method for adjusting the MOT laser beam axes. Together with the fluorescence signal we adjusted the beam path in a way, that both fluorescence and absorption are maximized.

To use this method in the QUEST is not recommended, since the optical dipole potential is too shallow, and the atoms are partly pushed out of the trap.

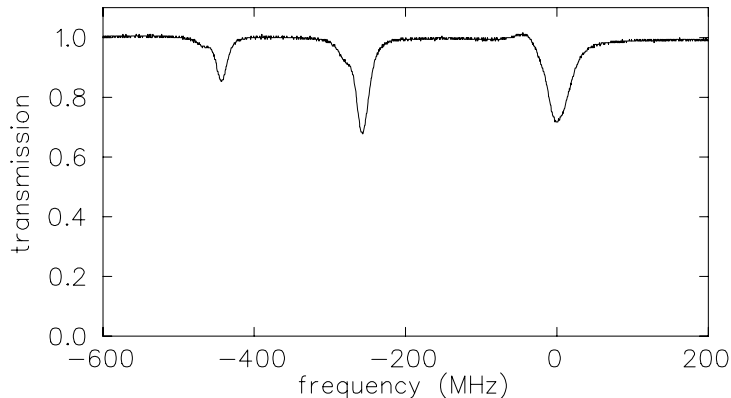


Figure 3.11: Absorption of a weak, focused probe laser by an ensemble of about 10^7 Cesium atoms in the MOT. The absorption peaks correspond to the transition $F = 4 \rightarrow F' = 3; 4; 5$ (from left to right). The frequency is given with respect to the MOT transition $F = 4 \rightarrow F' = 5$. The distortion in the absorption peaks originates from non-linear effects under the presence of the intense MOT light.

3.7 Timing of the experiment

The work presented here reports on experiments with two different species (Li and Cs) stored in two different traps (MOT and QUEST). Since on one hand the two species behave so differently and on the other hand the character of the various experiments differs so much, large effort was needed to provide sufficient flexibility in controlling the experiment. Without anticipating the following chapters at this point, a few tasks of the control system are mentioned, to illustrate the large variety of demands on timing and controlling the experiment.

For transferring atoms from the magneto optical trap into the quasi-electrostatic trap the timing sequences for both species differ quite a lot. As it turned out simultaneous storage of both species in the QUEST even requires separate transfer for best results. During the transfer, the relevant timing scheme is on the sub millisecond range. Even more precise resolution was required in ballistic expansion measurements where a total exposure time of $50\ \mu\text{s}$ was used. Here the timing resolution had to be reliable on a microsecond scale, while for long storage time experiments one single run took longer than 10 minutes. Hence the combination of high timing resolution and long cycle times is needed. Additionally, depending on the experiment up to 36 different TTL output channels have to be operated, some of them within a relative timing of $10\ \mu\text{s}$. During one cycle a single channel has possibly to be addressed a couple of times.

Today's standard personal computer (pc) working at several hundred MHz can not guarantee such a precision in timing, since unpredictable delays of several milliseconds due to the operating system of the machine are possible. We use an intelligent pc-card with "on board" processor (ADwin-4L card together with ADwin-LD extension card, manufacturer: Jäger Messtechnik, Lorsch). The digital signal processor (DSP) used on this device (Inmos transputer T40, 20 MHz) is optimized for short response times. In its 4 Mbyte memory data and program codes can be stored and recalled from the DSP in real time³. The card features its own timer of $1\ \mu\text{s}$ resolution and a timing depth of 32 bit, corresponding to a maximum cycle duration of 4000 s ($\simeq 66\ \text{min}$) at the given resolution. The real-time operating system is capable of controlling ten different processes quasi-simultaneously. Together both cards provide 44 TTL input/output channels and additionally 8 analog input channels and two analog output channels (each 0 to 10 V at 12 bit resolution).

The TTL-output channels can be addressed in steps of $10\ \mu\text{s}$ with a jitter of 200 ns only. The flexibility of this intelligent system allows for arbitrary programming of channels for the maximum cycle time of 66 minutes.

The experimental schedule can comfortably be determined by a LABVIEW[®] application. When starting the cycle, LABVIEW[®] generates a table containing the given timing sequences. The table is interpreted and executed by the ADwin cards, independent of the computer's CPU. Hence during a run, we can use the pc for other applications, such as data processing and analysis.

³ "Real time" in this context means, the desired operations are executed at a precisely predictable time within small tolerances of about 200 ns.

Chapter 4

Characterizing the quasi-electrostatic trap

This chapter briefly summarizes the basic parameters of the trapped atoms in the optical dipole potential of our CO₂-laser. In the first paragraph the characteristic values of the trapped Cesium ensemble are given. The second part reports on a measurement of the radial trap frequency of Cesium in the QUEST, which yields a precise value of the beam waist w_0 . In the last section a characterization of the trapped Lithium ensemble is given.

4.1 Typical parameters of trapped Cesium atoms

This section gives the most important parameters of the Cesium ensemble in the optical dipole potential of the CO₂-laser, such as storage time, number of atoms, temperature, spatial extension and resulting density respectively phase space density. Other significant quantities are the oscillation frequencies of the atoms in the QUEST, which are covered in the following section. Cesium atoms experience a trap depth of $U_0/k_B = 118 \mu\text{K}$ and their background gas limited decay time of several minutes is almost independent of the ground state population. No significant heating mechanism was found.

With the optimized transfer scheme typically 1.5×10^6 Cesium atoms are transferred into the QUEST, the associated transfer efficiency is about 6%. At a temperature of $12 \mu\text{K}$ right after transfer, the cloud extensions are: $\sigma_r = 21(\pm 2.8) \mu\text{m}$ and $\sigma_z = 900(\pm 30) \mu\text{m}$. From those numbers one calculates the peak density $\hat{n}_{Cs} = N/(\sigma_r^2 \sigma_z \sqrt{2\pi^3}) = 2.4 \times 10^{11} \text{ cm}^{-3}$.

The corresponding peak phase space density $\hat{\eta}$ is:

$$\hat{\eta} = \frac{1}{g} \hat{n} \Lambda_{dB}^3 = \frac{1}{g} \hat{n} \left(\sqrt{\frac{2\pi\hbar^2}{mk_B T}} \right)^3 \approx 1 \times 10^{-5}. \quad (4.1)$$

Here g denotes the degeneracy factor. Since the atoms are subjected to blue-detuned molasses only two Cesium sublevels are populated ($F=3; m_F=\pm 3$), therefore we get $g=2$ [Ver94].

After blue-detuned molasses cooling inside the QUEST a temperature of $6.5 \mu\text{K}$ is reached with typically 1×10^6 Cesium atoms. The cloud extensions under these conditions are: $\sigma_r = 17(\pm 1.5) \mu\text{m}$ and $\sigma_z = 700(\pm 30) \mu\text{m}$. From these numbers one calculates the peak density $\hat{n}_{Cs} = 4 \times 10^{11} \text{ cm}^{-3}$. The corresponding phase space density η is about 5×10^{-5} .

With evaporative cooling we reached $T=11 \mu\text{K}$ with 10^4 atoms. The corresponding peak density is $\hat{n} = 10^{10} \text{ cm}^{-3}$, and the phase space density is $\eta \approx 2 \times 10^{-6}$. Obviously, compared to evaporative cooling, with blue-detuned molasses cooling we can increase the phase space density by a factor of ten.

4.2 Determination of the radial trap frequency

The trap oscillation frequency is an important parameter to describe the dynamics of the atomic samples inside the optical dipole potential.

At a given laser power one can deduce the minimum waist w_0 from the radial trap frequency ω_r (assuming a harmonic approximation of the potential). Only with the knowledge of the waist one can accurately predict the potential depth.

By measuring only a single trap frequency for one atomic species one can calculate the frequency in any other direction as well as for any other species from the equations given in section 3.5.2.

We measured the radial trap frequency of Cesium and Lithium in our QUEST. In the following I will focus on the data of the Cesium radial trap frequency measurement since in the case of Lithium the measured data was less accurate.

4.2.1 Measurement of the radial trap frequency for Cesium

To measure the radial oscillation frequency of atoms in the quasi-electrostatic trap we take advantage of the fast switching capability of the CO_2 -laser. The laser can be turned off and on within about $200 \mu\text{s}$ ($90\% P_{max}$ to $10\% P_{max}$) by simply switching the rf-power driving the gas discharge. By turning the laser off for a short time interval (around 1 ms), the trapped ensemble moves ballistically until the laser is turned on again (*release-recapture*). One part of the atoms escapes from the trap, while the recaptured sample constitutes a non-equilibrium distribution which oscillates at twice the trap frequency¹.

When the first release-recapture cycle is followed by a second one, the number of finally recap-

¹The oscillation takes place in the radial as well as in the axial direction. On the short time scales relevant in the present case only the radial oscillation is considered.

tured atoms depends on the phase of the oscillation and thus on the delay time between the two cycles. Turning off the laser for the second time during an expansion phase of the atomic

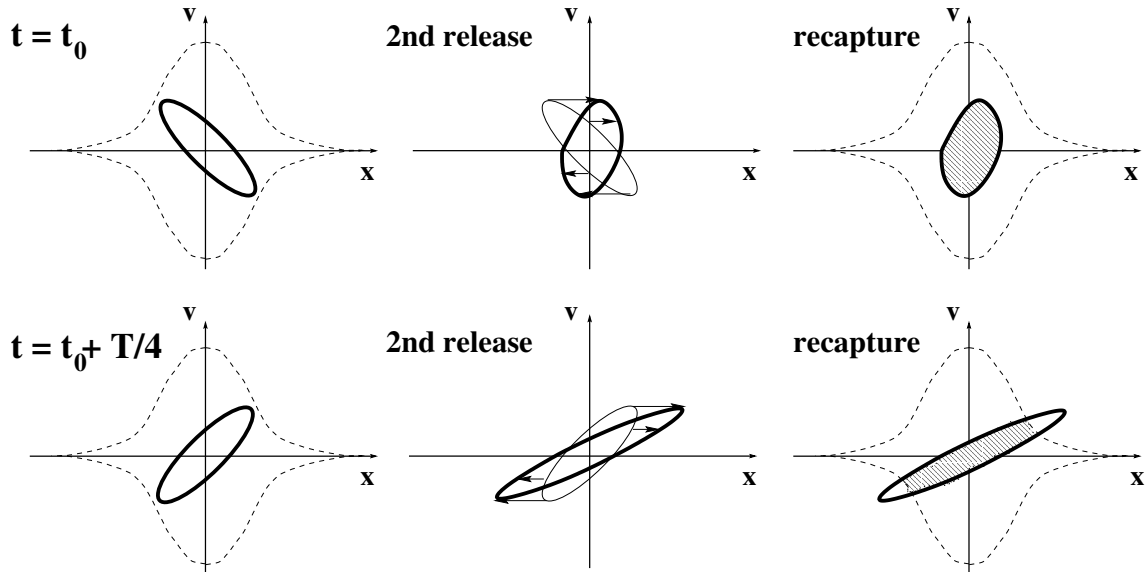


Figure 4.1: Illustration of the phase space evolution after the first recapture in the radial trap frequency measurement. The area inside the dashed lines indicates the phase space of the QUEST, the area inside the solid lines the occupied phase space of the atoms. Only atoms denoted by the hatched area remain in the trap after recapture. For explanation of the experiment see text above.

cloud leads to strong particle loss, since the atoms move ballistically apart and leave the trapping volume. On the other hand, if the second turn-off happens during the contraction phase, the loss is relatively small. Fig. 4.1 illustrates this behaviour in phase space. In the upper pictures the latter situation is illustrated. To the left, the phase of the ensemble right before second release is displayed. During the free expansion the cloud shrinks. At recapture the distribution lies completely inside the phase space volume of the QUEST. The lower picture shows the case of particle loss, since the atoms expand further during the second release, and at recapture only a fraction of the initial distribution occupies the phase space volume of the QUEST (hatched area).

4.2.2 Results for the radial trap frequency

In Fig. 4.2 the number of recaptured atoms is plotted as a function of delay time t between the two release-recapture cycles, the off period τ during the first release-recapture cycle was 0.7 ms. One observes a few cycles of coherent oscillations of the ensemble until the oscillation dephases mainly due to the anharmonicity of the trapping potential. The oscillation period of 1.8 ms yields a radial trap frequency of $\omega_r^{Cs} = 2\pi \times 270$ Hz in good agreement of the value expected from the trap parameters.

From this value one can calculate the axial frequency ω_z of Cesium according to

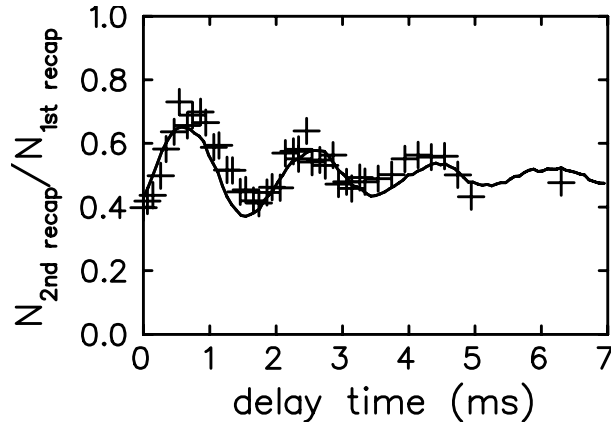


Figure 4.2: Measurement of the radial trap frequency of Cesium in the optical dipole potential of our CO_2 -laser. Two cycles of release-recapture are separated by a variable time delay. The free expansion time in each release-recapture cycle is 0.7 ms. The number of recaptured atoms after the second release-recapture cycle is normalized to the number of atoms after the first cycle. The result of a Monte-Carlo simulation is depicted by the solid line.

$\omega_z = \omega_r \times z_R / (w_0 \sqrt{2}) = 2\pi \times 8.6$ Hz, where z_R denotes the Rayleigh-range and w_0 the minimum waist.

By using the relation $\omega_i^{Li} = \omega_i^{Cs} \times \sqrt{U_0^{Li} m_{Cs} / (U_0^{Cs} m_{Li})}$ one calculates the corresponding frequencies for Lithium as: $\omega_r^{Li} = 2\pi \times 762$ Hz, respectively $\omega_z^{Li} = 2\pi \times 24.4$ Hz.

The solid line in Fig. 4.2 shows the result from a Monte-Carlo simulation of the classical atom trajectories for the sequence of two release-recapture cycles with variable time delay between them. The simulation takes into account the anharmonicity of the QUEST potential and the extension of the atomic cloud. The only free parameter in the simulation is w_0 . The best fit to the data corresponds to $w_0 \simeq 100 \mu\text{m}$, which is in good agreement with the value of $w_0 = 108 \mu\text{m}$, calculated from $\omega_r^{Cs} = \sqrt{4U_0^{Cs} / m_{Cs} w_0^2}$ (see section 3.5.2). For more details on the simulation see [Nil99].

Minimum waist w_0

With the equations given in section 3.5.2 one calculates from the value of ω_r^{Cs} a minimum waist of $w_0 = 108 \mu\text{m}$ for a given laser power of 30 W. This value is considered to be the most accurate we have on w_0 . As mentioned already, it is the basis for all calculations in this thesis.

In section 3.5.4 we have introduced a different evaluation of the beam waist w_0 , using an edge that was slowly moved in radial direction into the beam while monitoring the fractional power. A fit to the measured data yields value of $90 \mu\text{m}$. The evaluation of w_0 from the radial trap frequency gives a more reliable value, since:

- The present method takes into account the actual non-Gaussian intensity distribution of the CO₂-laser.
- For the measurements described in section 3.5.4 the laser power linearly influences the value of the waist. In contrast to those measurements for the present method the intensity fluctuations affect only weakly the result of w_0 , because for the radial trap frequency follows: $\omega_r \propto \sqrt{U_0}/w_0$. Since the trap depth U_0 is proportional to P/w_0^2 one finds: $w_0 \propto \sqrt[4]{P}$.
- The present measurement was performed on the actual setup of the experiment, not on a copy of the setup.

4.3 Typical parameters of trapped Lithium atoms

For the case of Lithium our CO₂-laser generates a trap depth of $U_0/k_B = 48 \mu\text{K}$. When prepared in the lower ground state the decay time of several minutes is background gas pressure limited. This value is in nice accordance with the one found for Cesium, as detailed in section 6. Again no significant heating mechanism was observed.

With the optimized transfer scheme typically 2.5×10^4 Lithium atoms are transferred into the QUEST, which corresponds to a transfer efficiency of about 0.02%.

The cloud extension in the optical dipole potential of the CO₂-laser is $\sigma_r^{Li} = 100 \mu\text{m}$, respectively $\sigma_z^{Li} = 1500 \mu\text{m}$. This results in an estimation for the peak density of $\hat{n} \approx 5 \times 10^8 \text{ cm}^{-3}$. These values have not been measured yet, but can be estimated from a Monte-Carlo simulation (section 5.1.2).

To assign a temperature to the Lithium ensemble in the QUEST potential makes no sense, since the transferred distribution is non-thermal and the density of the Lithium atoms in the QUEST is too small to assume thermalization within the storage time. Hence it is more reasonable to describe the mean thermal energy of the trapped ensemble. We investigated the mean thermal energy experimentally by a release-recapture measurement². The CO₂-laser trap was turned off for variable time intervals and the number of recaptured atoms into the QUEST was detected by finally transferring these atoms back into the MOT and measuring the fluorescence signal. By normalizing the number of recaptured atoms to the initial number, we get the fraction of recaptured atoms in dependence of the CO₂-laser's off duration (see Fig 4.3).

In order to determine the mean kinetic energy of the Lithium atoms a Monte-Carlo simulation of the process was performed. The mean kinetic energy was one of the free parameters. The solid curve in Fig 4.3 shows the best fit to the data, the associated mean kinetic energy is $k_B \times 21(\pm 2) \mu\text{K}$. Using the Virial-law, the mean total energy can be estimated as $k_B \times 42 \mu\text{K}$. Both, the measurement and the simulation are detailed in [Nil99].

²The usual ballistic expansion measurements did not work due to the small number of particles.

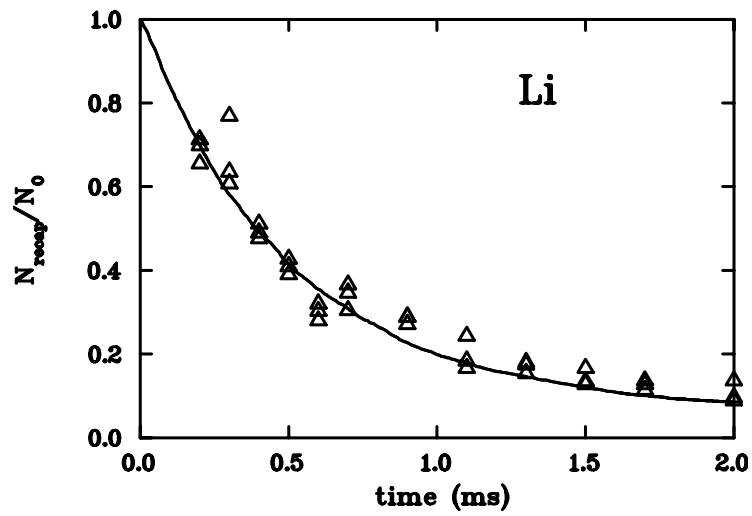


Figure 4.3: Ratio of recaptured Lithium atoms, when the CO_2 -laser trap was turned off for variable times. The solid curve represents the best fit of a simulation to the data, yielding a mean kinetic energy of $k_B \times 21 \mu\text{K}$.

Chapter 5

Transfer into the QUEST

Performing experiments with cold atoms in a QUEST requires as very first step the transfer of pre-cooled atoms from a magneto optical trap into the dipole trap. This chapter is based on the experimental outcome of our experiments. Nevertheless it starts with general calculations concerning the transfer efficiency. In the second part the optimum transfer scheme for Cesium and in the third part the one for Lithium is introduced. Finally a schedule of the combined transfer for simultaneous trapping of both species in the QUEST is given.

To illustrate the situation, in Fig 5.1 a simplified sketch of the transfer from the MOT into the quasi-electrostatic trap is shown.

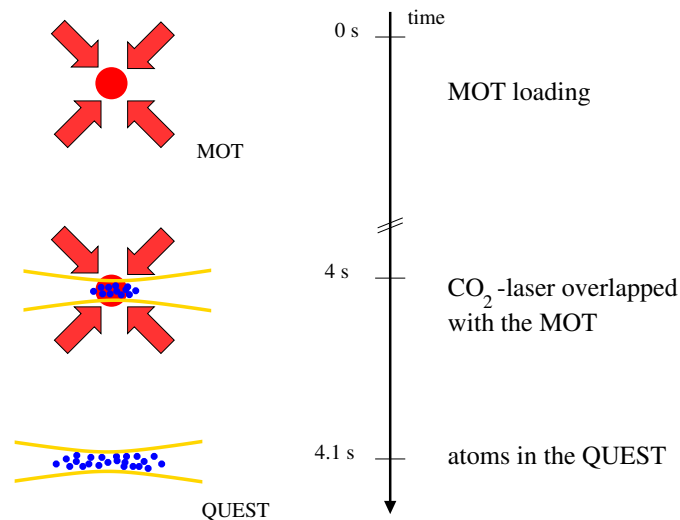


Figure 5.1: *The MOT provides a cold and dense atomic sample. The focus of the CO₂-laser is overlapped with the atomic cloud. After turning off the MOT lasers a fraction of the atoms is captured in the QUEST.*

5.1 Model

Transfer of magneto-optically trapped atoms into the CO₂-laser trap relies on the overlap in phase-space of the MOT and QUEST potentials, since after turning off the MOT beams and the quadrupole field an atom from the MOT is only trapped in the QUEST if it occupies a spot in the phase space of the QUEST potential. The Cesium and Lithium systems represent two extreme situations, since the relevant quantities of magneto-optically trapped Cesium atoms differ significantly from the corresponding values in the case of Lithium. Hence transferring the two different species into the CO₂-laser trap leads to well distinguished experimental starting points.

In the case of Cesium the MOT cloud has a similar extension (rms radius of 120 μm) as the beam waist $w_0 = 108 \mu\text{m}$ of the CO₂-laser, and the atomic temperature of not more than 25 μK is at least a factor of 4.7 below the optical dipole potential depth of $U_0^{Cs}/k_B = 118 \mu\text{K}$.

For Lithium the situation is completely different: MOT extension is about 2 mm in diameter and therefore exceeds by far the CO₂-laser waist w_0 . The temperature is about 1 mK, while the CO₂-laser trap depth of $U_0^{Li}/k_B = 48 \mu\text{K}$ ¹ is a factor of 20 smaller than the initial atomic temperature.

Therefore the transfer efficiencies for both species differ dramatically. In the following, two methods for predicting the transfer efficiency are introduced. Firstly, the model to calculate the transfer efficiency from the phase space overlap, and secondly the outcome of a Monte-Carlo simulation that gives information about the phase space distribution right after transfer is displayed.

Gravitational effects are small compared to the optical dipole potential depth and therefore not considered in the models.

5.1.1 Expected transfer efficiency

Since the QUEST parameter such as intensity distribution $I(r, z)$ and trap depth U_0 , as well as the atomic distribution in the MOT are well known, one can calculate the expected transfer efficiency from the overlap in phase space between the MOT distribution and QUEST potential. The calculations are shown in appendix E. In the following only the relevant results are given.

Transfer efficiency of Cesium

In order to calculate the transfer efficiency of Cesium one has to solve the integral in Eq. E.6. As stated above, with the given potential this can be done by solving numerically Eq. E.13. The trap depth is $U_0/k_B = 118 \mu\text{K}$. In our early experiments the achieved temperature was 25 μK

¹The trap depths for both species differ, because of the difference in the static polarizability; compare to section 3.5.2.

right before transfer, hence we get $\eta = U_0/k_B T = 4.72$. With a given MOT cloud extension of $\sigma_x = \sqrt{2} \sigma_y = \sigma_z \simeq 120 \mu\text{m}$ mathematica[®] calculates from Eq. E.13 a transfer efficiency of 25 %. The experimentally achieved transfer efficiency is typically on the order of 10 %.

More recent experiments started from one order of magnitude more atoms in the MOT. Here the cloud size was twice as large as before. Since we implemented an improved cooling scheme, MOT temperatures of $T \simeq 3 \mu\text{K}$ were reached. Here approximately 15 % of transfer efficiency is calculated, from the experimental data we get about 6 %. Even though the transfer efficiency is reduced, the total number of transferred atoms was increased of course, as shown later.

Transfer efficiency of Lithium

As stated at the beginning of this section, in the case of Lithium the situation is totally different. For Lithium the trap depth is much more shallow than the temperature at transfer, hence one can truncate the expansion of $\eta^{l+1/2}$ in Eq. E.13 after the first term, since $\eta \simeq 48 \mu\text{K}/1000 \mu\text{K} = 0.048$ and therefore terms of higher order can be neglected. Considering the extension of the cloud $\sigma_{MOT} \equiv \sigma_x = \sqrt{2} \sigma_y = \sigma_z \simeq 1000 \mu\text{m}$ with respect to the CO₂-laser waist of $w_0 = 108 \mu\text{m}$, one gets a simplified expression for the transfer efficiency:

$$\frac{N_T}{N} = \frac{4}{\sqrt{\pi}} \frac{1}{3} \frac{w_0^2}{6 \sigma_{MOT}^2} \frac{1}{\sqrt{1 + 3 \frac{\sigma_{MOT}^2}{z_R^2}}} \eta^{2/3} \simeq 8 \times 10^{-5}. \quad (5.1)$$

The measured value in the experiment was about 25×10^{-5} . The transfer efficiency is quite low, which represents the relatively small overlap in phase space due to the relatively high temperature and large extension of the Lithium MOT.

The measured transfer efficiencies differ typically by a factor of three from the calculated ones. Since the deviation is in different directions, this effect can not be caused by a systematic error. The introduced transfer model does neither consider dynamical effects during the transfer such as rearrangement of the atomic distribution while the MOT is turned off, nor the optical dipole potential is exactly known. Furthermore, the potential shape along the laser propagation axis z is described correctly by a Lorentzian curve and not by a Gaussian as assumed for simplification. For large MOT cloud extensions, like in the case of Lithium, this incorrectness gains influence. All these points are possible reasons for the deviation between model and experimental outcome. When considering the typical fluctuations in the transfer of up to 30 % from run to run, one can state the predictions are actually quite well.

The value of the transfer efficiency is of course important to know, however more important is the total number of atoms transferred into the QUEST. When starting from much higher numbers

N in the MOT, the number of transferred atoms N_T increases according to Eq. E.13. At the same time usually the transfer efficiency drops according to Eq. E.13, since the atomic cloud gets larger when the MOT is operated in the density limited regime [Wal94] and the number of particles is increased.

Optimum focal spot size

According to Eq. E.13 the transfer efficiency is determined by the trap depth, implemented in η , as well as by the focal spot size, expressed by the waist w_0 . With the above model, one can calculate the expected transfer efficiency in dependence of w_0 . In Fig. 5.2 the curves for both species are displayed. For the calculation the laser power is kept constant at 30 W, hence the potential depth U_0 decreases with larger w_0 .

Obviously the waist of $w_0 = 108 \mu\text{m}$ realized in our experiment matches the ideal value for both

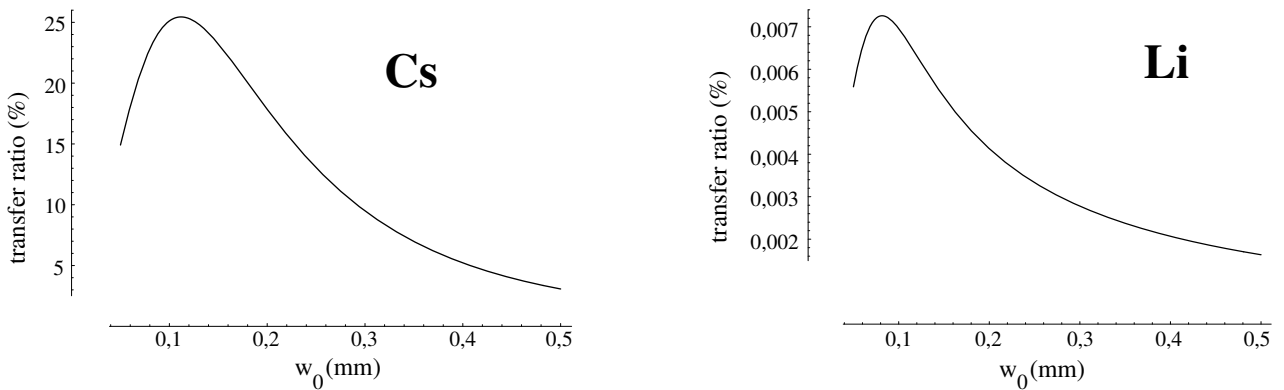


Figure 5.2: Calculated transfer efficiency of magneto-optically stored atoms into the QUEST in dependence of the CO_2 -laser waist w_0 for Cesium (left) and Lithium (right).

species closely. I have to admit this happened partly by chance, since the geometry of the laser setup and therefore w_0 was determined by the free aperture of the Zink-Selenite viewport and the location of the focusing lens (see Fig. 3.9).

For future experiments a 120 W CO_2 -laser will replace the current 30 W laser. In order to optimize N_T we will have to re-arrange the optical setup (as possible) such that w_0 is adapted to the higher laser power.

5.1.2 Monte-Carlo simulation

A computer program randomly generates 6-dimensional tuples, each representing an atom in the phase space of the MOT. By using an energy cut according to Eq. E.3 together with the potential shape of the QUEST the fraction of “atoms” successfully transferred into the QUEST is determined. Under the above assumptions, in the case of Cesium the transfer efficiency is

predicted to be 20 %, and in the case of Lithium 0.01 %. Again both values match the experimental outcome nicely.

The equations of motion, including gravity are solved for individual atoms. Thus we obtain information on the phase space distribution in the QUEST after transfer. Fig. 5.3 shows the resulting distributions for Cesium, respectively Lithium for 10^4 trapped particles 100 ms after transfer. While the Cesium distribution is well approximated by a Gaussian, a large fraction of Lithium atoms occupies high energetic states in the trap with large spatial extension. This is to be expected from the huge difference between the large temperature in the MOT and the shallow depth of the dipole trap. Under these circumstances, states at higher energy are more strongly populated due to the larger density of states. The axial rms extension of the Cesium cloud is $700 \mu\text{m}$, whereas the Lithium distribution has an axial width of $1500 \mu\text{m}$. The rms radial extension can be assumed to be on the order of the beam waist w_0 , hence one gets an estimation of the average Lithium density $\hat{n}_{Li} \simeq 10^8 \text{ cm}^{-3}$.

The Cesium distribution agrees well with the measured one in Fig. 8.1.

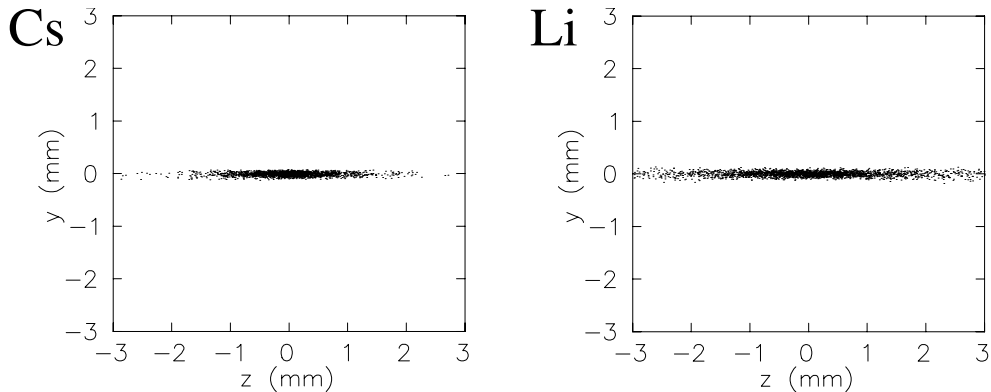


Figure 5.3: *Simulated distribution of Lithium and Cesium inside the QUEST, 100 ms after transfer.*

5.2 Cesium transfer

Supposing the MOT provides a sufficient number of atoms, according to the model described above one gets an increase in transfer efficiency with decreasing temperature (large overlap in momentum space) and increasing density (large overlap in real space). To fulfill these conditions different laser detunings and intensities for loading the magneto optical trap and preparing the sample for transfer are needed.

Similar to most other alkali atoms in the case of Cesium the optimum MOT laser detuning δ for accumulating atoms in the MOT is $\delta \simeq -2\Gamma_{Cs}$, which is relatively close to resonance. Here $\Gamma_{Cs} = 2\pi \times 5.3 \text{ MHz}$ stands for the natural line width (see section 3.2). In contrast the cooling is efficiently performed at larger detunings ($\simeq -20\Gamma_{Cs}$). Hence we distinguish between “accumu-

lating phase” and “transfer phase” in our experiment.

After a typical loading time of 5 s the atoms get prepared for transfer by a short polarization-gradient cooling phase: The CO₂-laser, generating the optical dipole potential is turned on at the end of the transfer phase, when some of the atoms still populate excited states. This results only in a shift of the atomic resonance (see Fig. 3.5.2) but does not cause serious heating effects, since atoms in the ground state as well as in the excited state are attracted by the CO₂-laser field, as stated in section 2.2. The resulting total light shift on the cooling transition of Cesium atoms is about -1.6 Γ [Lid90], which is small compared to the detuning for red-detuned molasses cooling². In the case of blue-detuned molasses cooling before transfer, the detuning is only a few linewidths and therefore we experienced an influence on the final temperature. We investigated the transfer for these two polarization-gradient cooling schemes.

5.2.1 Transfer with red-detuned molasses cooling

In earlier experiments we exclusively applied **red-detuned molasses cooling** using the MOT lasers. Here the detuning of the MOT cooling beam was switched to about $-27\Gamma_{Cs}$ with respect to the $6^2S_{1/2}, F = 4 \rightarrow 6^2P_{3/2}, F' = 5$ transition. This was done 40 ms before transfer (namely turn-off of MOT beams and anti-Helmholtz magnetic field). The detuning of the repumping laser is, due to the quasi closed transition in Cesium, negligible and therefore kept constantly on resonance (see section 3.2). An average density of 10^{10} atoms/cm³ at a rms radius of 120 μ m was reached. Right after turning off the MOT lasers the quadrupole magnetic field was switched off and the transfer into the QUEST was completed. By delaying the turn-off times either of the cooling or repumping beam for about 1 ms we optically pumped the atoms into the upper ground state $F = 4$ or the lower one $F = 3$.

During the MOT loading phase, the atomic sample has a temperature of about 70 μ K, with the red-detuned molasses cooling procedure we reached a temperature of 25 μ K. The total number of atoms in the MOT during these earlier experiments was on the order of $N_{MOT} \simeq 10^6$, resulting in a peak density of 3×10^{10} cm⁻³ when transferred. Independent of the ground state preparation typically up to 10^5 atoms were successfully transferred into the QUEST, yielding a transfer efficiency of about 10 %.

This scheme was used for the long time storing experiments, shown in chapter 6.1. The achieved transfer efficiency did not critically depend on the cooling detuning or duration. For cooling times longer than 50 ms the transfer efficiency dropped because the restoring force is low for large detunings, hence the density reduces. Applying red-detuned molasses for less than 4.5 ms reduces the transfer as well, since the temperature has not reached its lower limit. Fig. 5.4 shows the

²The principle of red-detuned molasses is described in detail in section 2.4.3, the one of blue-detuned molasses in section 2.4.4.

drop of temperature with cooling time for a detuning of $\delta = -150$ MHz.

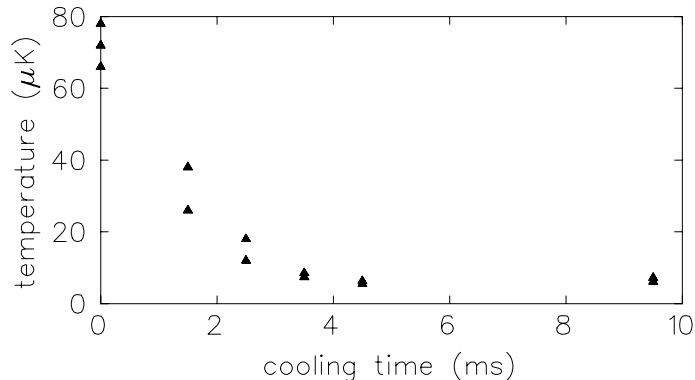


Figure 5.4: *Temperature versus cooling duration when applying red-detuned molasses cooling in free space (no magnetic fields on) to Cesium atoms. The detuning from resonance $F = 4 \rightarrow F' = 5$ was $\delta = -150$ MHz.*

Concerning the detuning, we found almost constant transfer conditions for red-detunings exceeding $-12 \Gamma_{Cs}$. For large detunings we were limited by our MOT laser locking scheme to about $-30 \Gamma_{Cs}$. Going to much larger detunings would not be promising, since one reaches the blue-detuned region of an other resonance in the Cesium excited state level structure, causing heating again.

Please note, in this scheme we used the same laser system for trapping and final cooling. The experimental setup provided no control of laser intensity, in order to tune intensity of the molasses field, and therefore the temperature reached (see section 2.4.2). The quadrupole magnetic field was still present during the cooling period, to provide a small restoring force.

5.2.2 Transfer with blue-detuned molasses cooling

Since **blue-detuned molasses cooling** allows for lower temperatures and higher densities due to the reduced scattering rate (see section 2.4.4) we added a blue-detuned molasses phase after the magnetic field turn-off. Therefore the transfer procedure described so far, was limited to a duration of 3 ms and served as a pre-cooling phase only, as long as the magnetic quadrupole field was present. The resulting rms radius of the cloud again was $120 \mu\text{m}$ and the achieved averaged density of 10^{10} atoms/cm³ can be considered to be maintained during the following blue-detuned molasses cooling procedure, since the atomic motion is strongly damped. Hence in the following we focus on the temperature development.

To generate a blue-detuned molasses an additional grating stabilized laser was implemented in a

way that its beam was overlapped with the MOT beams in all 3 dimensions³. Its intensity could be controlled and was typically a factor of 3 below the intensity of the MOT beams. Besides this we carefully equalized residual magnetic fields by making use of a dark state resonance method (see appendix A) to allow for ultra low temperatures on the order of $2 \mu\text{K}$.

The recent experiments are exclusively performed by using the additional laser for blue-detuned molasses cooling. As mentioned already, the transfer is now split into two phases, first part: cooling with MOT beams at $-27\Gamma_{C_s}$ before turning down the magnetic field, and a second part: applying a blue-detuned molasses phase using the additional laser when the magnetic field is zero. Here we were sensitive on the total light shift of the CO_2 -laser, which was present during the blue-detuned molasses phase.

The blue-detuned molasses cooling was carried out at $+5\Gamma_{C_s}$ to the blue side of the $F = 3 \rightarrow F' = 2$ and also on the $F = 3 \rightarrow F' = 3$ transition. One of the MOT beams was turned on during this phase and served as re-pumper on the $F = 4 \rightarrow F' = 4$ transition.

We applied the blue-detuned molasses phase at transfer for various times up to 20 ms, which is about 1/3 of the time it takes the atomic sample to reach its final distribution in the optical dipole potential of the CO_2 -laser (see Fig. 5.6). The resulting temperature and number of atoms inside the quasi-electrostatic trap is given in Fig. 5.5. For these measurements we stored the atomic sample for 100 ms inside the QUEST, before evaluating the temperature and particle number from a ballistic expansion measurement.

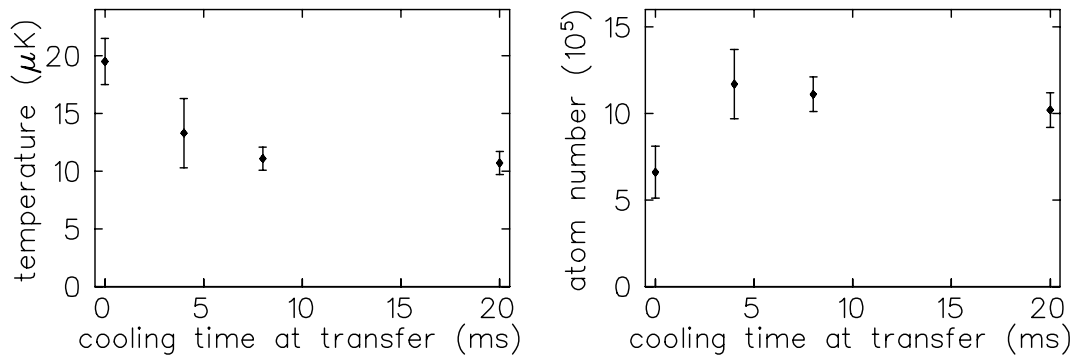


Figure 5.5: The **left side** shows the evolution of atomic temperature inside the QUEST in dependence of molasses duration after transfer. To the **right side** the evolution of stored particles in dependence of molasses duration is given.

The number of transferred particles is at its maximum at a molasses duration of 4 ms. For shorter blue-detuned molasses times the temperature has not dropped enough from the value given by the MOT molasses, leading to reduced transfer into the QUEST. Measurements of Sa-

³The beam overlap was done by a polarizing beam splitter cube used in the MOT laser setup. Hence the resulting polarization in one of the three blue-detuned molasses axes is perpendicular to the polarization of the associated MOT beam, leading to the wrong circular polarization in one axis. In the presence of the MOT quadrupole field this light causes instant trap loss, hence the laser could only be applied after turning down the MOT field.

lomon *et al.* [Boi96] show that typical cooling times of blue-detuned molasses are on the order of 2 ms.

Extending the molasses phase to times longer than 4 ms does not significantly reduce the temperature further but reduces the number of atoms in the QUEST, possibly due to weak radiation pressure or inelastic collisions. Hence for optimum transfer a blue-detuned molasses period of about 4 ms at transfer is indicated.

The exact timing scheme for optimum transfer is given in the following schedule, $t = 0$ denotes the time when blue-detuned molasses cooling is turned off:

$t = -5$ s	Loading, detuning MOT laser: $-2\Gamma_{Cs}$, MOT repumper on, CO ₂ -laser on
$t = -300$ ms	Zeeman-slower laser beam and atomic beam turn-off
$t = -15$ ms	Detuning of MOT laser: $-27\Gamma_{Cs}$, MOT repumper still on
$t = -12$ ms	Magnetic quadrupole field turn-off
$t = -10$ ms	Blue-molasses laser turn-on
$t = -9.5$ ms	MOT cooling laser turn-off, blue-detuned molasses repumper turn-on
$t = 0$ ms	Blue-molasses laser turn-off
$t = +0$ ms \pm 1 ms	Molasses repumper turn-off (\pm 1 ms allows for optical pumping)

Starting from an improved MOT providing 2×10^7 atoms, with the blue-detuned molasses scheme up to 2×10^6 particles were transferred into the QUEST in the experiment. Using the same scheme but instead of applying blue-detuned molasses cooling, maintaining the MOT molasses we ended up with typically 3×10^5 atoms. Hence implementing the blue-detuned molasses increased the number of atoms in the quasi-electrostatic trap by a factor of about 7.

One idea to improve the transfer was, as in the case of red-detuned molasses, to damp the motion of atoms initially located outside the CO₂-beam, when they cross the beam due to their motion in the gravitational field and therefore add them to the QUEST. Therefore the blue-detuned molasses field was maintained up to 100 ms after $t = 0$, which corresponds to roughly the oscillation time $\tau_z = 120$ ms along the weak axis of the QUEST (see section 4.2). But these efforts did not lead to better results, in contrast they resulted in a strong decrease of the number of transferred particles.

Remark: The timing given in the schedule is chosen quite conservatively in order to have reliable transfer, with moderate fluctuations from run to run. Typically the fluctuations of N_T are on the order of 30%, which is quite reasonable. If the timing is too critical, the fluctuations of N_T increase. This is due to the jitter of up to 1.5 ms of our mechanical shutter to turn off the MOT beams. If the cooling time is at its lower limit, the temperature strongly depends on the performance of the shutter. This is of course not desirable.

Fig. 5.6 shows snap-shots of the transfer described above from the magneto optical trap into the quasi-electrostatic trap for various times after MOT shut-off. Photograph number one shows the initial atomic distribution provided by the MOT, in picture number two the influence of the CO₂-laser can be noticed already. In the following pictures, atoms not affected by the optical dipole potential ballistically move apart while the cigar-shaped distribution in the QUEST forms. The last picture of the sequence shows the final atomic cloud in the QUEST.

We also investigated the performance of *red-detuned molasses cooling* with this additional laser. Since in contrast to the MOT lasers its intensity could be controlled, we tried to meet the results achieved with blue-detuned molasses cooling in the transfer. Even though in free space we reached similar results for the temperature with both detunings (see appendix C), concerning the transfer efficiency, red-detuned molasses cooling did not perform as well as blue-detuned molasses cooling. We did not find a combination of cooling time and detuning that would reach the success of blue-detuned molasses cooling. Usually, the results for the transfer efficiency were one order of magnitude below what we reached with the blue-detuned molasses cooling phase.

5.3 Lithium transfer

In the case of Lithium the same goals as in the case of Cesium were set: loading the MOT followed by a phase that increases the density and lowers the temperature before transfer. As in the case of Cesium the different aims are best realized by different detunings. In contrast to Cesium, due to the level structure of Lithium, one has to consider both MOT lasers, the “cooling” and the “repumping” beam, to be of equal importance (see section 3.1) when switching detuning and intensity.

Similar to Cesium transfer in the case of Lithium we also distinguish between an “accumulating phase” followed by a “transfer phase”. The transfer phase itself is split into a “compression phase” and “cooling phase”.

The loading scheme of the magneto optical trap is detailed in [Sch98b] and therefore based on the findings of that work. Loading of the Lithium MOT is best if both lasers are detuned -4 to $-5 \Gamma_{Li}$ to the red side of the $2^2S_{1/2}, F = 2 \rightarrow 2^2P_{3/2}, F' = 3$ respectively $2^2S_{1/2}, F = 1 \rightarrow 2^2P_{3/2}, F' = 2$ transition. A typical number of 2×10^8 atoms are accumulated. Under these conditions the cloud is at the threshold to its density limited regime, the peak density is on the order of 10^{10} , as stated in [Sch98b]. The temperature of the atoms during the accumulation phase is on the order of 2 mK.

The group of Salomon at ENS (Paris) explicitly studied the cooling of Lithium in a magneto optical trap below 1 mK [Mew99, Fer99]. The outcome of their efforts was in part the basis to our experimental strategy.

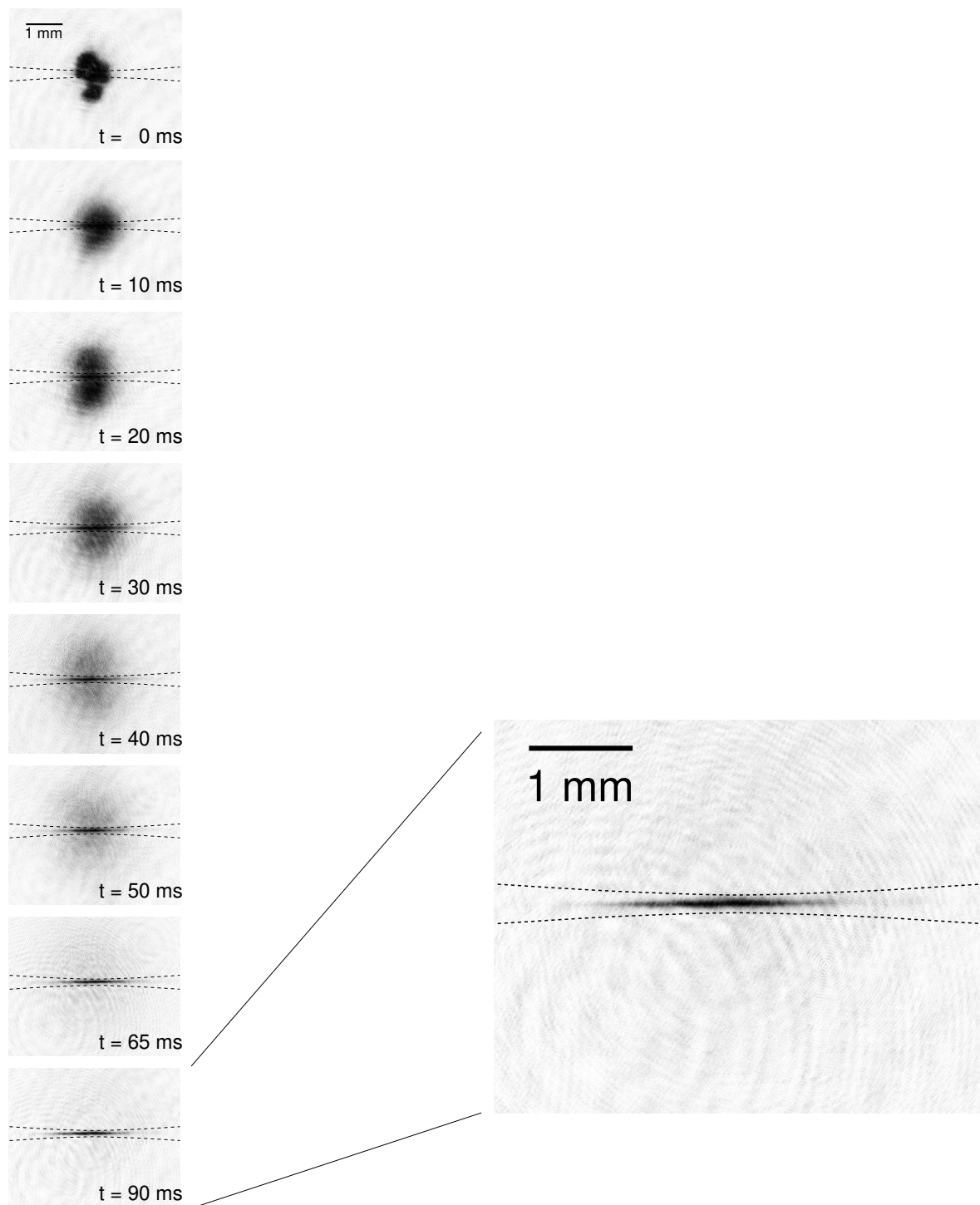


Figure 5.6: Sequence of the Cesium transfer from the MOT into the QUEST. The dashed lines indicate the waist envelope of the Gaussian shaped CO_2 -laser beam. From the pictures one sees nicely the differing extensions of the MOT and QUEST. The timing given below the pictures refers to the origin of time at MOT turn-off. The rms axial extension in the last picture is $700\ \mu\text{m}$.

Doppler cooling

In our experiment after a loading time of typically 7s the atomic cloud is first compressed to increase the density and afterwards cooled.

Therefore we varied the detuning of both lasers simultaneously. As a first step we investigated the *compression* of the Lithium cloud, by measuring the resulting transfer efficiency into the QUEST. Concerning the optimum detuning for compression, the measurements showed clearly a maximum transfer at a detuning of $-1.5\Gamma_{Li}$. In contrast to Cesium, where a sub-Doppler mechanism leads to higher densities due to the reduced temperature, here one has to switch closer to resonance in order to increase the spring-constant of the MOT. Unfortunately this is accompanied by a negative effect: switching the detuning closer to resonance leads also to higher scattering rates and therefore to trap loss, since, due to photon re-absorption, the atoms start to repel each other strongly, as the density increases [Tow96]. Hence the duration of compression is a critical parameter. Keeping the detuning at $-1.5\Gamma_{Li}$ we varied the compression time. The best transfer resulted from a compression time of 2ms. With this scheme typically a fraction of less than 1×10^{-4} out of 1×10^8 atoms were transferred into the QUEST.

Measuring the density of the Lithium cloud right after compression, with an absorption imaging method failed, since the CCD-camera shutter has a rise time of about 1ms. Hence taking a picture from the shadow of the Lithium cloud directly after compression was not possible, since it would have been saturated by the fluorescence of the compression cycle. We had to allow a delay of at least 1ms after the lasers were turned off. Due to the relatively high temperature of several millikelvin, the density was too low already to receive clear signals.

An absorption measurement with a focused probe beam right after compression was not reliable because of the varying optical pumping between the two ground states for different compression schemes.

After optimizing the compression cycle, the *cooling phase* was investigated. As stated in section 3.1, for the case of Lithium only Doppler-cooling can be expected, hence the temperatures one deals with are well above $T_{Dop}^{Li} = 140\mu\text{K}$.

Ballistic expansion measurements give the most reliable results on temperature measurements. This time we tried to shortly flash on the atoms after various times and take fluorescence pictures of the cloud expansion. But again we went into the same troubles with the CCD-camera. After 1ms of free expansion the detected fluorescence signal was too weak for reliable determination of the temperature. The problem of temperature measurement in the case of Lithium could not be overcome quickly, hence we had to postpone an improvement. To give a number for the temperature: Some measurements allowed for a rough estimation of the temperature between $300\mu\text{K}$ and 1mK at transfer.

Since our actual goal was to maximize the transfer efficiency, again we determined the conditions

for best transfer from the number of transferred atoms into the QUEST. Two electro-optical modulators allowed for intensity control of the MOT laser beams, used also for cooling. According to the theory of two level atoms, Doppler-cooling works most efficiently in the case of low intensity and at a detuning of $-1/2 \Gamma_{Li}$ [Coh92, Ada96]. By combining different intensities and detunings we found a maximum in transfer when detuning the “cooling laser” ($F = 2 \rightarrow F' = 3$) to $-5 \Gamma_{Li}$ while the “re-pumper” was switched to $-1.5 \Gamma_{Li}$ from its transition ($F = 1 \rightarrow F' = 2$). Both laser intensities were attenuated to 20% of their regular intensity I_0 . The optimum duration of this cooling phase turned out to be 7 ms. The CO₂-laser is switched on shortly before turn-down of the magnetic field.

The following list summarizes the results. Notation: $\delta_{F=2}$ and $\delta_{F=1}$ denote the detuning from the $F = 2 \rightarrow F' = 3$, respectively $F = 1 \rightarrow F' = 2$ transition, and I denotes the intensity of both lasers:

$t = -8$ s	Loading, detuning MOT laser: $\delta_{F=1} = \delta_{F=2} = -5 \Gamma_{Li}$, CO ₂ -laser on
$t = -300$ ms	Zeeman-slower laser beam and atomic beam turn-off
$t = -10$ ms	Compression detuning: $\delta_{F=1} = -2 \Gamma_{Li}$, $\delta_{F=2} = -2 \Gamma_{Li}$
$t = -8$ ms	Cool detuning: $\delta_{F=1} = -2 \Gamma_{Li}$, $\delta_{F=2} = -5 \Gamma_{Li}$ & $I = 20\% I_0$
$t = -1$ ms	First MOT cooling laser turn-off
$t = -0.5$ ms	Magnetic quadrupole field turn-off
$t = \mathbf{0}$ ms	Second MOT cooling laser turn-off

The delay between turning off the two cooling lasers allows for optical pumping in either ground state $F = 2$ or $F = 1$. With this schedule the long time storage measurements are taken. Starting from 1×10^8 atoms in the MOT typically 25000 atoms were transferred into the QUEST, yielding a transfer efficiency of 2.5×10^{-4} .

Chapter 6

Long time storage

Combining an excellent vacuum on the order of 2×10^{-11} mbar with the outstanding properties of a CO₂-laser trap, such as its purely conservative potential, the absence of photon scattering and the possibility to prepare the atoms in any ground state sub-level, opens new prospects to investigate the behaviour of atomic samples on very long time scales. Two extremely different representatives of alkalis, namely Cesium and Lithium, were stored in the CO₂-laser trap separately up to ten minutes. When prepared in the upper hyperfine structure ground state inelastic collisions are observed. In this chapter, firstly, the results on Cesium and secondly, the ones on Lithium are presented.

For both species the single particle loss lifetime due to background gas collisions was determined. In the case of Cesium additionally the loss coefficient due to inelastic binary ground state collisions was found.

6.1 Long storage times of Cesium

Since the realization of long storage times was one of the most important goals of our experiment, one of the first measurements we made was to determine the lifetime of Cesium in the QUEST. For systematic investigation two series of long time storage with Cesium were performed. The experimental procedures were identical, excluding the preparation of the ground states. In one series the atoms were prepared in the lower hyperfine structure ground state ($F = 3$), and in the other they were pumped into the upper hyperfine structure ground state ($F = 4$). The ground state preparation is done by optical pumping at the end of the transfer phase (see section 5.2.2). To determine the lifetime, atoms from the MOT are transferred into the QUEST, and after variable times, recaptured back into the MOT. With respect to the number of atoms in the initial MOT, the development of the number of recaptured atoms yields the ensemble lifetime in the QUEST. To measure the atomic numbers we took fluorescence pictures of the magneto-optically stored atoms with a CCD-camera. For each single cycle 4 pictures were taken:

1. Picture of MOT shortly before transfer.
2. Picture of a short flash on the atoms in the QUEST close to the end of storage.
3. Picture of recapture MOT.
4. Picture of background in absence of atoms, with MOT laser beams on.

The first picture is for normalizing the number of recaptured atoms from picture # 3 in order to compensate for fluctuations of the starting MOT. The last picture is for individual background subtraction from the pictures within the current cycle, in order to become independent of fluctuations of the background as well.

Picture # 2 was a snap-shot of the atomic distribution inside the optical dipole potential and served for investigating the temperature evolution due to evaporative cooling. This data is the basis for the measurements presented in section 7.1. For the present investigation this picture plays no role, since the fluorescence signal was low and therefore not suitable for data analysis after long storage times, when only a small fraction of the initial number of atoms is present. We took care that the flash from picture # 2 would not influence the life-time measurement at all. The number of initial and recaptured atoms differs typically by some orders of magnitude. To compensate for the large difference of the fluorescence signal in picture # 1 and # 3 different detunings were used. The CCD-camera exposure time was set to 40 ms. The picture of the starting MOT was taken during the 40 ms cooling phase before transfer (see sec. 5.2.1), at a detuning of $-27\Gamma_{Cs}$. To reach a wide “dynamic range” the detuning of the recapture MOT in picture # 3 was $-4\Gamma_{Cs}$ only. This way we were sensitive to a few hundreds of atoms in the recapture MOT and avoided saturation of the CCD-chip in picture # 1, since the CCD-camera used for these experiments did not allow for individual exposure times. The timing is shown in Fig. 6.1.

For both hyperfine structure sub-levels of the ground state storage times up to ten minutes

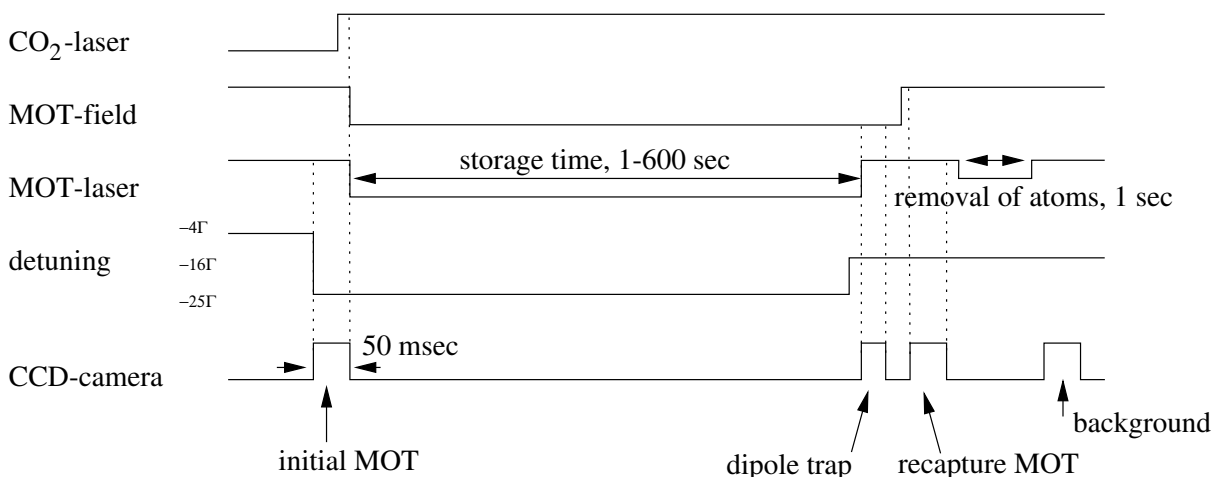


Figure 6.1: Illustration of the timing sequence for long time storage of Cesium in the QUEST. The horizontal axis denotes the time and is not true to scale.

were observed. According to the transfer scheme described in section 7.1, when prepared in the $F = 3$ ground state we have loaded 90000 atoms into the QUEST. In the $F = 4$ ground state 50000 atoms were successfully transferred. Fig. 6.2 shows the evolution of particle number versus storage time in the QUEST. Each point originates from one single cycle, the smoothness of the curve is remarkable, since the total run time for one of the curves is almost three hours.

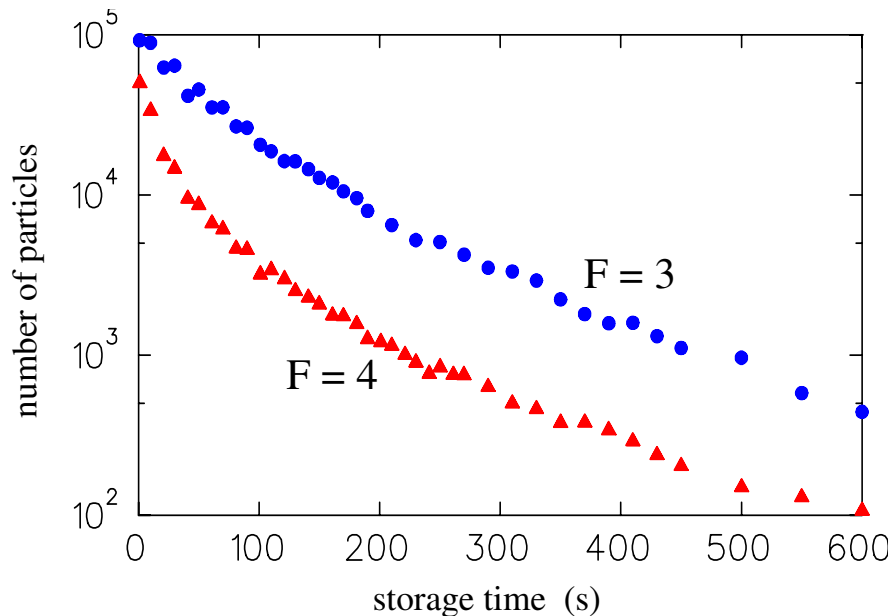


Figure 6.2: Long time storage of Cesium in the QUEST. The decay for each single ground state is given. A fit to the data points at long storage times in both curves yields a $1/e$ lifetime of some minutes. (Fit not shown in this picture.)

Interpretation of the decay curves

In general, for the atomic decay two processes are identified: collisions with background gas, expressed by a linear loss term $\alpha n(\vec{r}, t)$, and inelastic inner trap collisions, expressed by a quadratic loss term $\beta n^2(\vec{r}, t)$. Eq. 6.1 expresses the evolution of particle number N :

$$\frac{d}{dt}N(t) = -\alpha \int dV n(\vec{r}, t) - \beta \int dV n^2(\vec{r}, t) = -\alpha N(t) - \beta \bar{n}(t) N(t), \quad (6.1)$$

where $\bar{n}(t)$ denotes the average density at time t . For an harmonic approximation of the optical dipole potential and under the assumption of a thermalized atomic sample one can consider the distribution to be Gaussian. Taking the volume V to be constant, the solution of Eq. 6.1 is:

$$N(t) = \frac{N_0}{\exp(t/\tau) + \tau \beta \bar{n}(0) [\exp(t/\tau) - 1]}, \quad (6.2)$$

where $\tau \equiv 1/\alpha$ denotes the $1/e$ lifetime. In a Gaussian distribution the average density $\bar{n}(t)$ is related to the total number of atoms N by:

$$\bar{n}(t) = \frac{n_0}{2^{3/2}} = \frac{1}{2^{3/2}} \frac{N}{(2\pi)^{3/2} \sigma_x \sigma_y \sigma_z}. \quad (6.3)$$

Due to the radial symmetry of the QUEST potential, with the waist w_0 and the Rayleigh range z_R , one can take $\sigma_x = \sigma_y \equiv \sigma_r = w_0 \sqrt{k_B T / 4U_0}$ and $\sigma_z = z_R \sqrt{k_B T / 2U_0}$, getting:

$$\bar{n}(t) = \frac{2}{(2\pi)^{3/2}} \frac{N}{w_0^2 z_R} \left(\frac{U_0}{k_B T} \right)^{3/2}. \quad (6.4)$$

With the measured initial temperature of $25 \mu\text{K}$ (see section 5.2.1) and a trap depth of $U_0 = 118 \mu\text{K}$ one calculates an average initial density of:

$$\bar{n}(0) \simeq 4 \times 10^9 \text{ cm}^{-3}. \quad (6.5)$$

The lower curve in Fig. 6.2 shows the decay of atoms transferred in the $F=4$ ground state into the QUEST. The deviation of the data from a linear decay for storage times shorter than 150 s indicates inelastic collisions inside the trap. The collision of two atoms in the upper ground state can lead to a flip of nuclear momentum in one or both atoms, releasing 9.2 GHz, respectively 18.4 GHz of hyperfine structure energy. Both collision partners escape from the QUEST, since the trapping potential has a maximum depth of $U_0/h = 2 \text{ MHz}$ only.

Fig. 6.3 shows only the data of the $F=4$ decay together with a fit according to Eq. 6.2. The fit yields a lifetime of $\tau = 161 (\pm 25) \text{ s}$ and for the second fit parameter we get $\beta \bar{n}(0) = 0.088 \text{ s}^{-1}$. With the average density from Eq. 6.5 a quadratic loss parameter $\beta = 2.2 (\pm 0.4) \times 10^{-11} \text{ cm}^3/\text{s}$ is calculated. The value of the quadratic loss parameter β is in accordance with the values of $5 \times 10^{-11} \text{ cm}^3/\text{s}$ given by [Lem95, Ses89].

For atoms prepared in the absolute ground state $F=3$ one expects a purely exponential decay ($\beta = 0$), exclusively due to collisions with hot background gas atoms. For this case Eq. 6.2 simplifies to

$$N(t) = N_0 \exp(-t/\tau). \quad (6.6)$$

As one clearly sees, this pure exponential decay is well fulfilled in Fig. 6.4 for storage times longer than 200 s, (linear decay).

For shorter storage times we see a faster decay, indicating an additional loss mechanism, potentially associated with binary collisions among the trapped particles. Fig. 6.4 displays only the

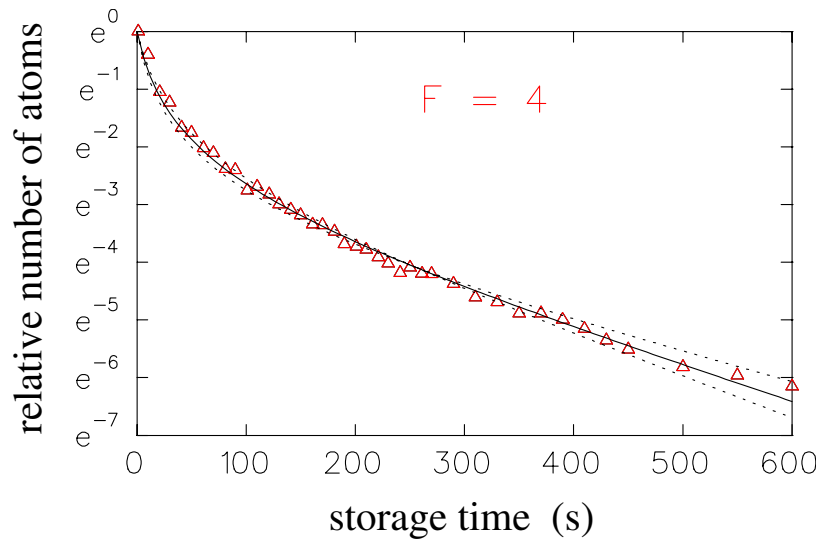


Figure 6.3: Decay of Cesium in the $F=4$ ground state in the QUEST (same data as in Fig. 6.2), together with a fit according to Eq. 6.2 (solid line), yielding a lifetime of 161 s. The dashed lines indicate the error on the fit.

$F = 3$ data together with the fit curve. A fit of Eq. 6.2 to the $F = 3$ decay curve in Fig 6.2, varying τ and $\beta\bar{n}(0)$, matches nicely the data points and yields a lifetime $\tau = 140 (\pm 20)$ s. The second fit parameter, $\beta\bar{n}(0) = 0.016 \text{ s}^{-1}$ leads with the known average density to a quadratic loss parameter of $\beta = 4.5 (\pm 1.2) \times 10^{-12} \text{ cm}^3/\text{s}$. The given value of β is of limited evidence, since from a pure $F = 3$ ground state Cesium sample one would not expect the existence of quadratic losses.

The appearance of $\beta \neq 0$ might indicate: a fraction of Cesium was initially not prepared in the $F = 3$ but in the $F = 4$ ground state sub-level, causing the observed inelastic binary collisions, until their fraction became negligible after about 200 s. It was checked that more than 95 % of the particles are initially prepared in the lower ground state so that inner trap inelastic collisions can be excluded.

The faster initial trap loss can be attributed to evaporation of highly-energetic particles from the trap leading to cooling, as described in section 7.1. At the initial temperature of $25 \mu\text{K}$ the trap depth is less than $5k_B T$. Since the evaporation scales with the square of the density, Eq 6.2 can be fitted to this data. The observation of evaporative cooling in the QUEST is discussed in detail in section 7.1.

The background gas limited lifetime is within the errors consistent with the value of the $F = 4$ decay.

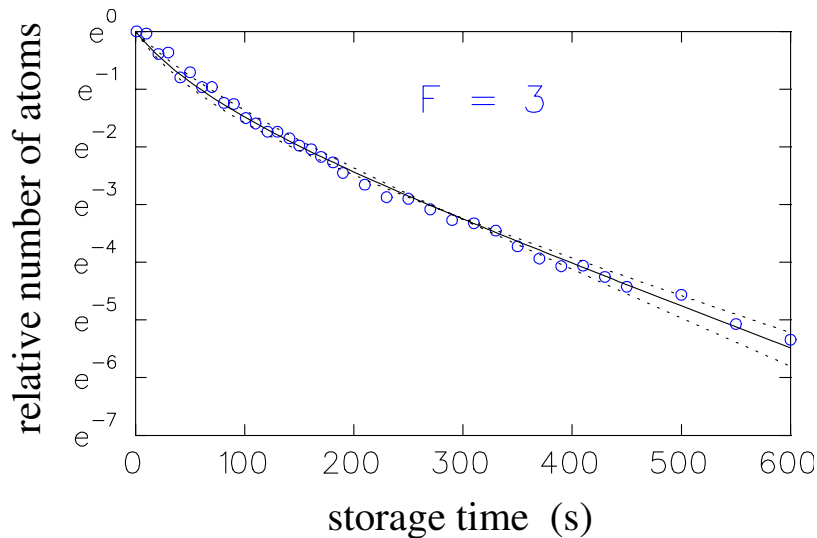


Figure 6.4: Decay of Cesium in the $F=3$ ground state in the QUEST (same data as in Fig. 6.2), a fit considering quadratic losses is also shown (solid line). It yields a $1/e$ lifetime of 140 s. The dashed lines indicate the error on the fit.

6.2 Long storage times of Lithium

Since the capability to trap all kinds of atoms in the quasi-electrostatic trap is one of the outstanding properties of our system, it was quite interesting to explore, if an atomic sample that has strongly differing properties compared to Cesium, would also achieve similar lifetimes in our QUEST. We repeated the long storage time experiment with Lithium. The transfer scheme is detailed in section 5.3. This time only three pictures with the CCD-camera were taken per cycle:

1. Picture of MOT shortly before transfer.
2. Picture of recapture MOT.
3. Picture of background in absence of atoms, with MOT laser beams on.

The first picture of the initial MOT was taken shortly before transfer in order to compensate for fluctuations on the initial number of atoms. The third picture was taken to subtract the “current” background from the two previous pictures.

Due to the small transfer efficiency on the order of 10^{-4} (see section 5.3) and since the optical dipole potential is extremely shallow in the case of Lithium ($U_0^{Li}/k_B = 48 \mu\text{K}$), we gave up taking a snap-shot of the atoms inside the QUEST, to make sure the Lithium sample would not be disturbed before MOT recapture.

Due to the extremely small transfer efficiency, the limited dynamic range of the CCD-camera could no longer be counterweighted simply by choosing different detunings for picture # 1 and

2. For the present measurements we used a new CCD-camera which has the option of setting individual exposure times from shot to shot. Hence picture # 1 had an exposure time of only a few milliseconds in contrast to 300 ms exposure time for picture # 2¹. Fig. 6.5 illustrates the schedule of the experiment:

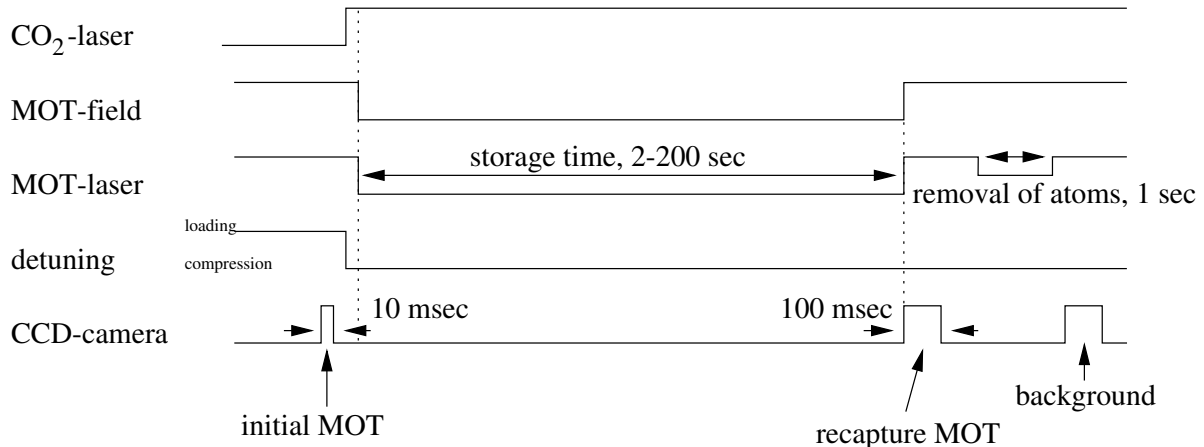


Figure 6.5: Illustration of the timing sequence for long time storage of Lithium in the QUEST. The horizontal axis denotes the time and is not true to scale.

Nevertheless the Lithium long time storage experiment delivered reliable data only up to a storage time of 200 s. For longer times the remnant number of atoms was only a few hundreds and the signal-to-noise ratio became unacceptable. Fig. 6.6 shows the Lithium decay for both ground state sub-levels. The initial MOT provided 2×10^8 atoms during this session on a very constant level. The fluctuations were about $\pm 5\%$.

For the prove of principle and to compare this measurement to the Cesium runs, we wanted to know if there is a tiny fraction of Lithium left in our QUEST after ten minutes. In a separated run we extended the exposure time to 2 s and took a picture of the MOT recapture after the maximum storage time of ten minutes. Indeed, the camera picture showed a clear signal of remnant Lithium atoms. Their number was far below 100 atoms.

Interpretation of the decay curves

The data analysis was done in analogy to the Cesium measurement. When prepared in the lowest ground state sub-level $F=1$, similar to the observation in the Cesium decay, a not expected quadratic loss appears for the first 100 s. The fit using Eq. 6.2 yields $\tau = 168 (\pm 27)$ s, in nice accordance with the previously described Cesium experiment. Due to the strong variation of the data points, the upper and lower limit differ significantly. A lifetime of 100 s can be considered as

¹Longer exposure times were excluded, because the fluorescence signal of the recapture MOT at short storage times would have saturated the CCD-chip.

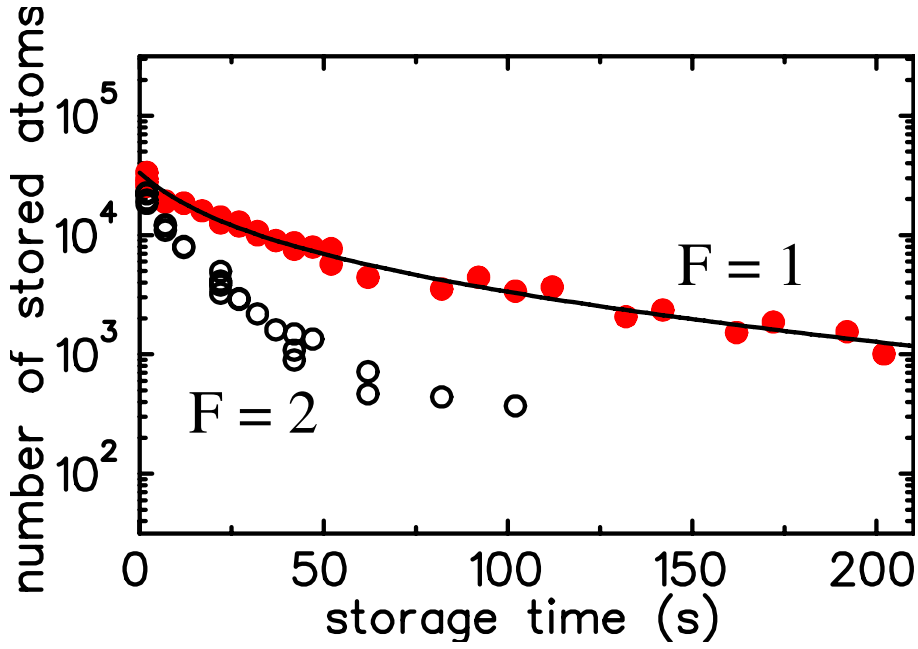


Figure 6.6: Long time storage of Lithium in the QUEST. The decay for each single ground state is given. A fit only to the long storage time data of the $F=1$ sub-level curve yields $\tau \approx 168$ s.

lower limit and 1000 s as upper limit for the Lithium ensemble inside the QUEST. Fig. 6.7 shows again the data of the $F = 1$ sub-level decay (same data as in Fig. 6.6) together with the fitted lifetimes.

The value of the second fit parameter $\beta\bar{n}$ from Eq. 6.2 is 0.06 ± 0.02 s $^{-1}$. Because of the high temperature (1 mK), the low trap depth ($U_0^{Li}/k_B = 48$ μ K) and the assumed small inner trap scattering rate, one can not consider the ensemble to be thermalized. Since we also couldn't take absorption images of the cloud, the average density $\hat{n}_{Li} \simeq 10^8$ cm $^{-3}$ is taken from the simulation in section 5.1.2. Therefore a quadratic loss rate coefficient of $\beta_{Li} \simeq 6 \times 10^{-10}$ cm 3 /s can be evaluated.

For the upper ground state sub-level $F=2$ the analysis is not trivial. Since we observed an extremely quick decay within the first 100 s, no reliable measurement for longer storage times was possible. We explored a dramatic decay due to inner trap collisions. Fig. 6.8 shows again the data of the $F = 2$ sub-level decay (same data as in Fig. 6.6) together with the fitted lifetimes. By using the fit, the lifetime due to single particle loss τ was kept constant at the value evaluated before for the lower sub-state $\tau = 168$ s, since the regime of linear decay was not observed here. For the value of $\beta\bar{n}$ the fit yields 0.25 s $^{-1}$, which is an outstandingly large value. This value might be considered as an estimation only, since the data points vary a lot, due to the small number of atoms. Therefore $\beta\bar{n}$ is given without errors.

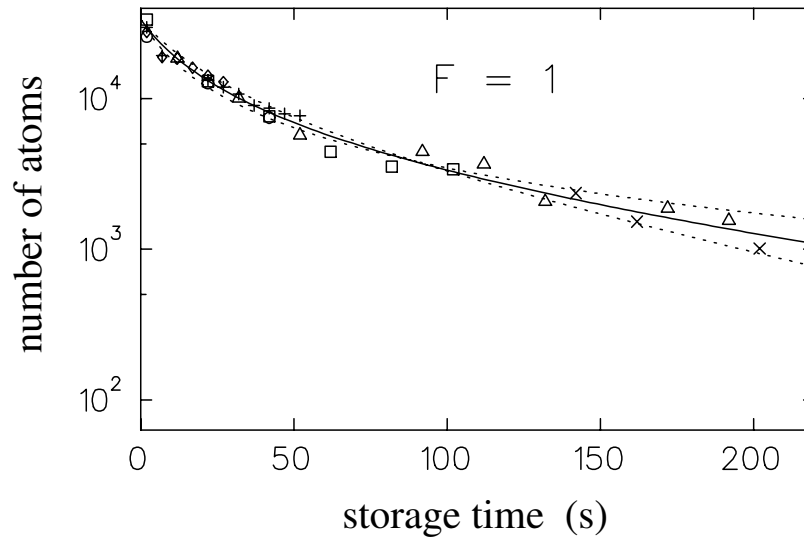


Figure 6.7: Decay of Lithium in the $F=1$ ground state in the QUEST (same data as in Fig. 6.6), a fit considering quadratic losses is also shown (solid line). It yields a lifetime of 168 s. The dashed lines indicate the error on the fit.

Summary Even though the number of Lithium atoms in our quasi-electrostatic trap lags behind the number of Cesium atoms, we have clearly demonstrated: long time storing of Lithium and Cesium in the CO_2 -laser trap works well and the achieved single particle loss lifetime of $\tau_{Li} = 168$ s is in nice agreement with the one of Cesium $\tau_{Cs} = 161$ s and purely background gas limited. Furthermore, as expected, no principle difference in long time storing between Cesium and Lithium was found.

These results are very promising with respect to future experiments concerning the sympathetic cooling of Lithium by Cesium, where we expect the interaction to take place on time scales of some 10 s.

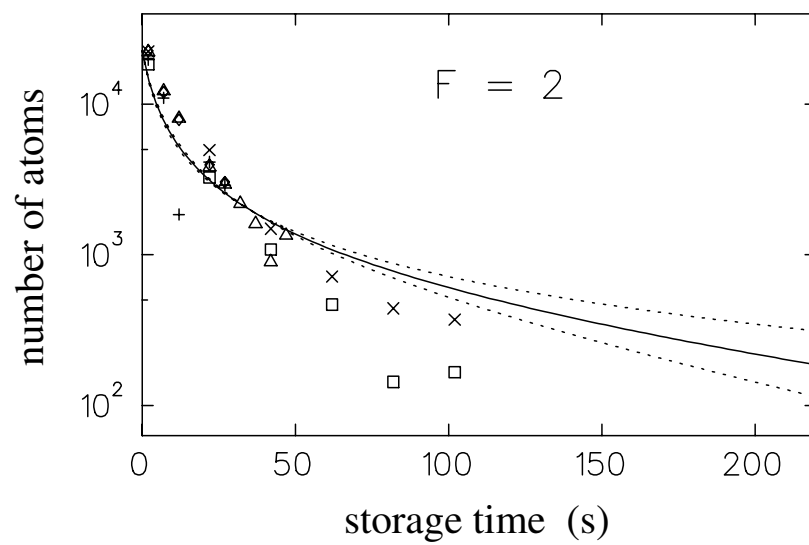


Figure 6.8: Decay of Lithium in the $F=2$ ground state in the QUEST (same data as in Fig. 6.6), a fit considering quadratic losses is also shown (solid line). For short storage times, it yields a lifetime of about 25 s. The dashed lines indicate the error on the fit.

Chapter 7

Cooling of Cesium

The present chapter reports on two cooling processes observed on the trapped Cesium ensemble in our QUEST:

Firstly, evaporative cooling down to temperatures corresponding to about a tenth of the trap depth. And secondly, active cooling by subjecting the trapped Cesium atoms to blue-detuned molasses inside the QUEST. Here we reached even lower temperatures, namely on the order of $6\text{-}7\ \mu\text{K}$. A cooling process on Lithium was not studied during this thesis.

7.1 Evaporative cooling of Cesium

The general principles of evaporative cooling are introduced in section 2.4.1 already. Here the individualities concerning evaporative cooling in our experiment and the results are given.

Even though evaporative cooling is a widely used technique for efficient cooling in magnetic traps to achieve Bose-Einstein condensation [Ket96], up to now, only one experiment demonstrated evaporative cooling in an optical trap. In order to achieve sufficiently high densities, Adams et al. have demonstrated evaporative cooling of sodium atoms in a crossed beam dipole trap, providing tight confinement in all three dimensions [Ada95].

For the simple focused-beam geometry in our experiment it is somewhat surprising to find evaporative cooling since the achievable densities are rather low. The reason that evaporation takes place lies in the combination of very long storage times in our experimental setup and the anomalously large elastic cross section of Cesium at low temperatures [Arn97]. Although the density of Cesium atoms in our dipole trap is only on the order of $10^9\ \text{atoms}/\text{cm}^3$, one expects a thermalization time of several seconds due to the abnormal large interaction cross section. This time scale is indeed more than one order of magnitude smaller than the achieved storage time, and therefore evaporative cooling can take place.

7.1.1 Estimation of thermalization time

In order to quantitatively describe the evaporation, one first has to determine the elastic scattering cross section σ_{el} and the elastic scattering time τ_{el} . For thermalization the evaporation process needs a sufficient rate of elastic collisions among the particles, which can be estimated from the following.

Measurements by Guéry-Odelin et al. [Gué98] gave a lower limit on the Cesium scattering length of $a_{Cs} \geq 600 a_0$, where a_0 denotes the Bohr radius. The scattering cross section of non-identical bosons can be calculated from [Arn97], where $|\vec{k}|$ denotes the de-Broglie wave vector:

$$\sigma_{el} = 4\pi \frac{a^2}{1 + (a|\vec{k}|)^2}. \quad (7.1)$$

Since the atomic cloud represents a thermal distribution of atoms, we have to approximate σ_{el} by an effective cross section σ_{eff} , which depends on an effective de-Broglie wave vector $|\vec{k}| \equiv k_{eff} = k(\bar{v}_{rel})$. The effective de-Broglie wave vector depends on the mean relative atomic motion \bar{v}_{rel} . From the following evaluation of the absolute value of the effective de-Broglie wave vector results a simplification of σ_{eff} .

$$k_{eff} = \frac{\bar{p}_{rel}}{\hbar} = \frac{\mu \bar{v}_{rel}}{\hbar} = \frac{m_{Cs}}{2\hbar} 4 \sqrt{\frac{k_B T}{\pi m_{Cs}}} = \frac{2}{\hbar} \sqrt{\frac{m_{Cs} k_B T}{\pi}} \gg 1/a, \quad (7.2)$$

where $\mu = m_{Cs}/2$ denotes the reduced mass and $\bar{v}_{rel} = 4\sqrt{k_B T / (\pi m_{Cs})}$ the mean relative velocity between two Cesium atoms. In the present temperature regime we find $(k_{eff} a)^2 \gg 1$ and therefore σ_{eff} becomes independent of the scattering length a . This regime is called the *unitary limit*, for which Eq. 7.1 can be approximated by

$$\sigma_{eff} \approx \frac{4\pi}{k^2} = \frac{\pi^2 \hbar^2}{m_{Cs} k_B T}. \quad (7.3)$$

In the present case the scattering cross section only depends on the temperature T via k . Assuming an average temperature of $15 \mu\text{K}$ the cross section becomes $\sigma_{el} \approx (930 a_0)^2$. Taking the values of the mean density in our trap $\bar{n} = 4 \times 10^9 \text{ cm}^{-3}$, and the mean relative velocity $\bar{v}_{rel} = 6.4 \text{ cm/s}$, one calculates an elastic scattering time of:

$$\tau_{el} = \frac{1}{\sqrt{2} \sigma_{el} \bar{n} \bar{v}_{rel}} = 2.1 \text{ s}. \quad (7.4)$$

An atomic ensemble is considered to be in its thermal equilibrium after roughly 11 collisions of each particle [Arn97], resulting in a *thermalization time* of about 23 s, which is short compared to the life time of Cesium in the trap.

7.1.2 Observations

Temperature measurement from cloud expansion The data of the temperature evolution is mainly taken in the course of the long storage time experiment, described in section 6.1.

Therefore the experimental parameters are introduced already. Here we focus on the cloud size, which we get from the CCD-picture labeled number two in the schedule of section 6.1. One can deduce the temperature from the spatial extension of the atomic ensemble inside the well-known optical dipole potential according to:

$$n(\vec{r}) = n_0 \exp(-U(\vec{r}) / k_B T). \quad (7.5)$$

The explicit conversion of measured spatial distribution into temperature is detailed in [Web00, Wei00]. Due to the limited resolution of the imaging system of the CCD-camera, we only evaluated the temperature from the “long axis” of the trapped cloud (distribution along the CO₂-laser propagation axis). The radial extension of the cloud is about 100 μm. Variations with temperature on this short scale would not be resolved by the imaging system used during those experiments.

On the left side of Fig. 7.1 the temperature of the trapped atoms in the $F = 3$ ground state is

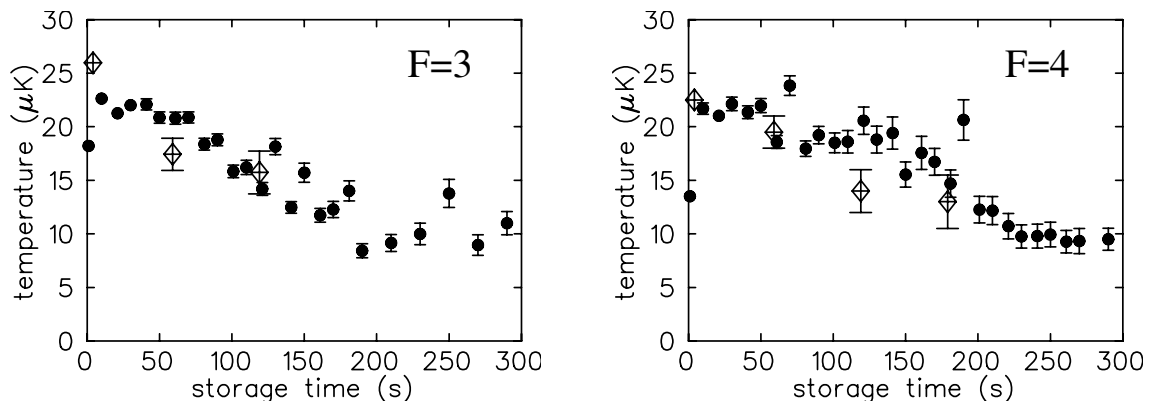


Figure 7.1: *Evaporative cooling of the trapped Cesium gas, prepared in the $F = 3$ (left side) and $F = 4$ ground state (right side). The dots give the temperature derived from the axial extension of the trapped cloud while the diamonds show the result of a ballistic expansion measurement.*

plotted versus storage time. The dots represent the temperature derived from the density distribution. In contrast to the long storage measurement, here the quality of the snap-shot picture is only sufficient for reliable analysis up to storage times of 300 s. Which is long enough, since the evaporation has come to its end after 200 s, where $T \approx U_0/10 \approx 10 \mu\text{K}$ is reached, as explained in section 2.4.1.

Temperature measurement by ballistic expansion To cross-check the temperature measurement described above, we took independent measurements via ballistic expansion after release from the QUEST at three different storage times ¹: 4, 59, and 119 seconds. The results of these

¹One temperature determination via ballistic expansion measurement requires a whole series of transfer and storage cycles in the QUEST. Therefore a temperature measurement takes a long time, especially when the tem-

measurements are given by the diamonds in Fig. 7.1. This second method nicely confirms the previous temperature determination.

The temperature evolution for atoms in the $F = 4$ ground state to the right side of Fig. 7.1 shows a similar behaviour, but with a slower decrease of the temperature. This is to be expected due to the faster initial density decrease through inelastic collisions and the resulting decrease in the rate of thermalization through elastic collisions. Again, the temperature derived from the density distribution (shown by the dots) is in good agreement with a temperature evaluation based on ballistic expansion measurements (given by the diamonds) after evaporation times of: 4, 59, 119, and 179 seconds.

One clearly observes cooling of the gas caused by evaporation of atoms from the QUEST at constant trap depth (*plain evaporation*). Although the temperature is reduced by about a factor of two after 150s, the phase space density remains almost constant, since the particle number diminishes by a factor of 10 at the same time, as shown in Fig. 7.2. The solid line gives the predictions of a model calculation, briefly given in the following section, simulating plain evaporative cooling from the trap.

From the observation of evaporative cooling with a temperature decrease of $10 \mu\text{K}$ over a time scale of 100 s, one can infer that heating rates induced by laser noise are much lower than 100 nK/s .

7.1.3 Model of evaporation

Luiten et al. [Lui96] give a quantitative model to simulate the evolution of temperature T and particle number N during evaporation. For the given shape of the potential and the corresponding density of states, the model provides two coupled differential equations for the evolution of particle number N and temperature T :

$$\frac{dN(t)}{dt} = -\sigma \beta_{evap}(T(t)) N(t)^2 - \alpha_{bg} N(t) \quad \text{and} \quad (7.6)$$

$$\frac{dT(t)}{dt} = -\sigma \gamma_{evap}(T(t)) N(t), \quad (7.7)$$

where σ is the elastic scattering cross section, $\beta_{evap}(T(t))$ denotes the loss rate coefficient for N , $\alpha_{bg} = 1/\tau$ the background gas collision rate, and $\gamma_{evap}(T)$ the rate coefficient of the temperature decrease. As the temperature drops, the number of atoms that are able to leave the trap is exponentially suppressed, approximately like $\exp(-U_0/k_B T)$ [Lui96]. One therefore expects β_{evap} to decrease with temperature and to finally vanish once the temperature has reached a certain threshold on the order of $U_0/10$. For more details see also [Wei00].

Since the potential is fully determined by the QUEST parameters, the only adjustable parameters perature is evaluated after storage times of some minutes. Therefore we performed the ballistic expansion cycle only after certain storage times. This measurement must be considered as a cross-check of the previously described method.

in the model are the background gas collision rate $\alpha_{bg} = 1/140 \text{ s}^{-1}$ and the cross section for elastic collisions σ among the trapped atoms. As estimated in section 7.1.1, due to the large scattering length the elastic collision cross section σ depends on the temperature. In the model a temperature independent interaction cross section σ is assumed, therefore we have fixed the effective cross section to the value $\sigma_{el} = (930 a_0)^2$, corresponding to an assumed average temperature of $15 \mu\text{K}$. The resulting curves are displayed in Fig 7.2. As one sees, the model slightly overestimates the rate of evaporation, but for both curves it is in reasonable agreement with the experimental data. The little discrepancy can be explained by the influence of gravity on one hand and the temperature dependent cross section σ on the other hand, which both are not considered in the model. Gravity restricts evaporation essentially to one spatial dimension and thus slows down the cooling process. The temperature dependence of the cross section gives rise to an increased thermalization time so that the rate of evaporative cooling is decreased.

The model also shows that in the long time storage experiment the observed initial faster loss of particles in the $F = 3$ state (see Fig. 6.4) mainly stems from the evaporation process.

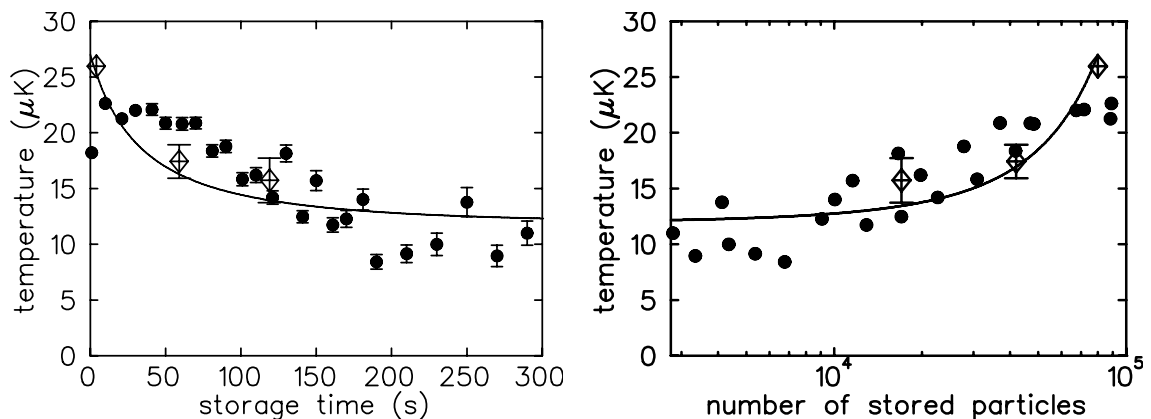


Figure 7.2: Comparison between measurement and simulation for evaporative cooling. **Left side:** Temperature versus evaporation time of the trapped Cesium gas, prepared in the $F = 3$ state. **Right side:** Temperature versus particle number for the same atomic sample. The data stems from the set shown in Fig. 7.1. The dots give the temperature derived from the axial extension of the trapped cloud while the diamonds show the result of a ballistic expansion measurement. The solid line gives the predictions of a model calculation, simulating plain evaporative cooling from the trap, according to [Lui96] and [Wei00].

7.2 Polarization-gradient cooling of Cesium inside the QUEST

One of the most challenging goals for future experiments inside the quasi-electrostatic trap is sympathetic cooling of Lithium by using Cesium as a cooling agent. Therefore we investigated an active cooling mechanism on Cesium atoms stored in the QUEST. The most important requirement on the cooling process is to reach a temperature on the order of a few μK quickly after

transferring the atoms into the QUEST without dramatic trap loss at the same time. As stated in section 2.4 the most promising technique is to apply polarization-gradient cooling not only during the transfer but also inside the CO₂-laser trap shortly after transfer. Doing so suppresses particle loss due to evaporation from the very beginning, since the expected temperatures are below $U_0/10$. Particularly, applying blue-detuned molasses cooling is expected to prevent strong particle loss during the cooling process, since the atoms are mainly populating “dark states” (referring to section 2.4.4) which are decoupled from the molasses light field. Because of the resulting reduced photon scattering rate (with respect to red-detuned molasses cooling) one neither expects losses related to imbalanced radiation pressure along the CO₂-laser axis, nor losses caused by inelastic inner trap collisions, since only a small fraction of atoms populates excited states. The atoms are prepared in their absolute ground state and therefore even inelastic ground state collisions are excluded.

Nevertheless we applied both, red-detuned molasses and blue-detuned molasses cooling to the Cesium sample in the QUEST.

For all measurements we started with the optimized transfer scheme given in section 5.2.2. Hence the initial temperature of the atomic ensemble in the QUEST was about 12 μK and typically 1.5×10^6 particles were transferred during these measurements.

To give an impression about the results of our cooling efforts on Cesium inside the QUEST, Fig 7.3 shows ballistic expansion measurements for three different situations. The left picture corresponds to an experimental run without subjecting the atoms to blue-detuned molasses during transfer and without cooling inside the QUEST. The associated ensemble temperature is 22 μK . The middle one shows the ballistic expansion of the cloud, applying blue-detuned molasses during the transfer. The corresponding temperature is 11.8 μK . The data on the right hand side shows a sequence of the cloud expansion after additional blue-detuned molasses cooling of the atoms inside the QUEST down to a temperature of 6.5 μK .

To our knowledge there is only the group of M. Weitz and T.W. Hänsch at the Max-Planck-Institut für Quantenoptik in Munich where polarization-gradient cooling was applied to atoms in a CO₂-laser trap. [Fri98a, Fri98c] reports on blue-detuned molasses cooling of Rubidium atoms in a standing wave CO₂-laser trap down to 15 μK .

In section 7.1.1 we saw that the relevant time scale for thermalization of the Cesium sample in the QUEST is given by the elastic collision time of 2.1 s, which predicts a *thermalization time* of 23 seconds. Relevant for polarization-gradient cooling inside the QUEST is a much shorter *cooling time*, which is related to the axial oscillation time in the shallow potential of $\tau_z \approx 120$ ms. After this time each atom twice has converted its potential energy into kinetic and vice versa. If the cooling duration is short compared to this time scale but comparable to the radial oscillation

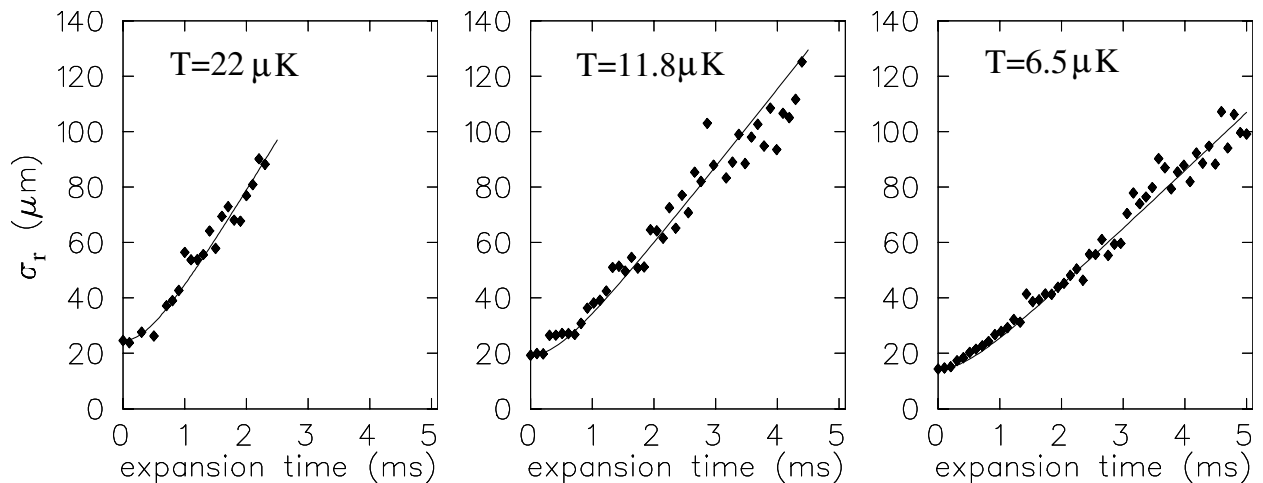


Figure 7.3: *Ballistic expansion measurements from the QUEST for different experimental situations. The fitted Cesium ensemble temperatures are given in the pictures. The **left side** shows an expansion for a situation, where blue-detuned molasses was applied neither during the transfer, nor during the storage in the QUEST. The **middle** picture shows the ballistic expansion, when the blue-detuned molasses was applied during the transfer. On the **right** side a sequence of the cloud expansion after additional blue-detuned molasses cooling of the atoms inside the QUEST is shown. The particle number during these measurements was about 1.5×10^6 .*

time $\tau_{rad} = 4$ ms, only the transversal motion is well damped. Thus an atom located at the outer axial-region of the trap potential might not get efficiently cooled, since its axial velocity is small already. Such an atom gains back kinetic energy after a short cooling pulse, by moving downwards in the trapping potential. Via elastic collisions the energy gets distributed between all degrees of freedom after several seconds and the cooling effect on all atoms is reduced.

Applying polarization-gradient cooling on a time scale of 100 ms is not advisable, since it turned out it gives raise to non-negligible trap loss. Therefore the cooling time is supposed to be as short as possible. Fig 7.4 shows the behaviour of the number of Cesium atoms for various durations of red-detuned, respectively blue-detuned molasses cooling up to 20 ms. The loss in the case of red-detuned molasses cooling is roughly a factor of 4 larger as compared to the case of blue-detuned molasses cooling. Nevertheless, for both situations the induced particle loss would be too strong if the cooling period was extended to about 100 ms in order to finally damp the atomic motion in axial direction.

The particle loss is in part due to inelastic collisions involving excited states, and partly due to small residual radiation pressure during the cooling phase. Since the potential depth is so small, hyperfine structure changing collisions lead to immediate trap loss. Due to the weak gradient along the CO₂-laser axis, a small radiation pressure imbalance will push the atoms along this axis out of the trap. Since both effects are more important in red-detuned molasses cooling, the particle loss is stronger.

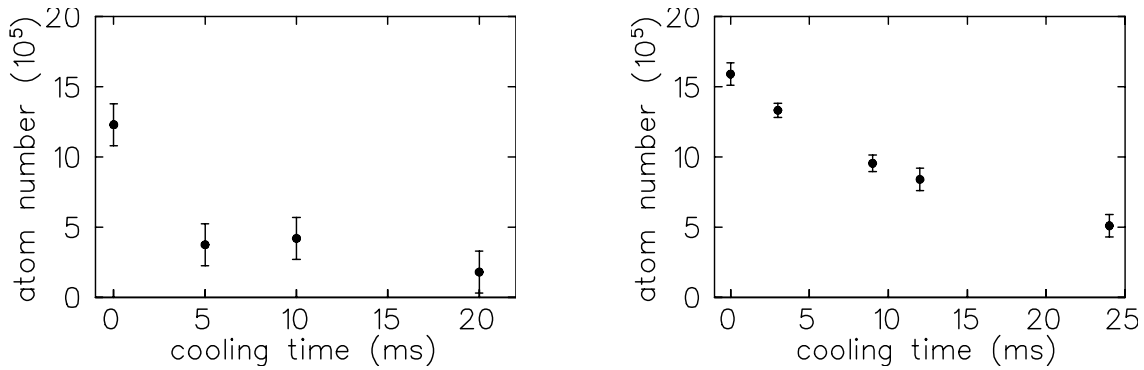


Figure 7.4: Applying red-detuned molasses cooling (**left side**) and blue-detuned molasses cooling (**right side**) to Cs inside the QUEST. The evolution of particle number versus cooling time is shown.

In order to finally damp the atomic motion, we considered a sequence of short pulses, with some ten milliseconds delay between the single pulses. Doing so damps the axial atomic motion in the optical dipole potential during different oscillation phases step by step and at the same time results in reduced photon scattering rates for both, red-detuned molasses and blue-detuned molasses configurations (compared to continuous cooling). The delay time between two cooling periods was technically determined by our mechanical laser shutters to 180 ms. This delay time is reasonable since it is short compared to the inner trap collision time of 2.1 s and it is not an integer multiple of the axial oscillation time τ_z . Therefore efficient cooling can be expected. The results are given in the following.

7.2.1 Cooling in red-detuned molasses

From experiments with red-detuned molasses in free space, shown in Fig. 5.4, we learned it takes typically 5 ms to cool the Cesium sample. This time determines the duration of each red-detuned molasses phase in the cycle of repeated cooling pulses. The first cooling pulse was applied 100 ms after transfer, every following pulse with a delay of 180 ms, as stated above. The number of cooling pulses was varied. Ten seconds after the last cooling pulse the temperature of the Cesium ensemble was measured by a ballistic expansion method.

The temperature achieved after a certain number of pulses is displayed in Fig. 7.5. During these measurements we started from about 2×10^7 atoms in the MOT, and transferred typically 1×10^6 atoms into the QUEST. The atoms were prepared in their absolute ground state $F = 3$.

What we found was not a cooling effect, but a heating effect. The temperature was increased from the transfer temperature of $12 \mu\text{K}$ to about $23 \mu\text{K}$ after applying the 4th cooling pulse.

The increase in temperature can be blamed on the random character of photon scattering in the

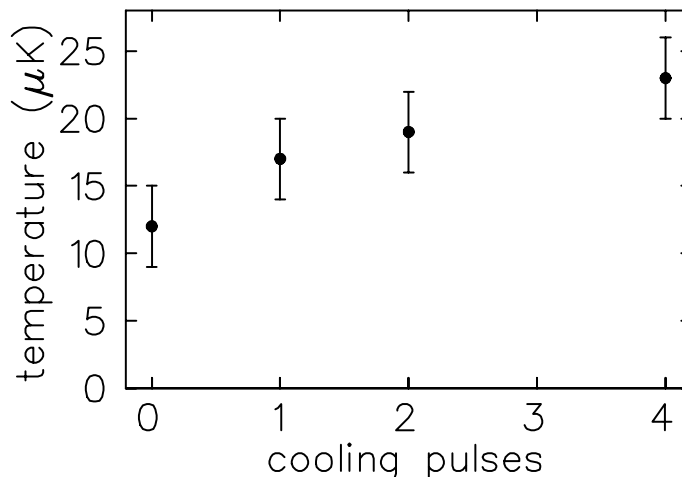


Figure 7.5: Applying 5 ms pulses of red-detuned molasses cooling inside the QUEST. The temperature versus number of molasses pulses is given. The detuning was $\delta = -17\Gamma_{Cs}$ with respect to the $F = 4 \rightarrow F' = 5$ transition.

molasses field.

The cooling detuning for the data presented in Fig. 7.5 was $\delta = -90$ MHz with respect to the $F = 4 \rightarrow F' = 5$ transition and the intensity was about $3 \times I_0$.

Varying the detuning and intensity of the molasses light did not improve the situation. Since we expected better results on blue-detuned molasses cooling we did not spend more time on closer investigations about the performance of red-detuned molasses cooling inside the QUEST.

7.2.2 Cooling in blue-detuned molasses

In contrast to red-detuned molasses cooling, applying blue-detuned molasses worked quite well. The initial temperature of $12 \mu\text{K}$ after transfer was reduced to $6\text{-}7 \mu\text{K}$, when the cooling was performed on the blue side of the $F = 3 \rightarrow F' = 2$ transition.

In free space blue-detuned molasses cooling on the $F = 3 \rightarrow F' = 3$ transition yielded the same results as cooling on the $F = 3 \rightarrow F' = 2$ transition. When applied inside the QUEST, blue-detuned molasses cooling on the $F = 3 \rightarrow F' = 3$ transition worked not efficiently and resulted in temperatures around $10 \mu\text{K}$. The difference in cooling performance between both transitions can be found in the differing light shift potentials due to the different Clebsch-Gordon coefficients and in the selection rules of electric dipole transitions. The latter reason plays the dominant role, since the $F = 3 \rightarrow F' = 2$ transition is a “closed” one. Whereas in the case of a $F = 3 \rightarrow F' = 3$ transition optical pumping into the $F = 4$ ground state leads to interruptions in the cooling process, and therefore a reduction of the average friction coefficient is experienced.

In the following we concentrate on the results achieved with blue-detuned molasses cooling on the closed $F = 3 \rightarrow F' = 2$ transition.

During these measurements we started from about 2×10^7 atoms in the MOT, and transferred typically 1×10^6 atoms into the QUEST. The atoms were prepared in their absolute ground state $F = 3$.

At 100 ms after transfer into the optical dipole potential we applied the first blue-detuned molasses pulse. As in the case of red-detuned molasses the delay between two pulses was 180 ms. Since the cooling time in blue-detuned molasses is about 2 ms only (see [Boi96]), the duration of a single pulse was 3 ms. The number of cooling pulses was varied. Ten seconds after the last cooling pulse the temperature of the Cesium ensemble was measured by a ballistic expansion method. The temperature achieved after a certain number of pulses is displayed in Fig. 7.6.

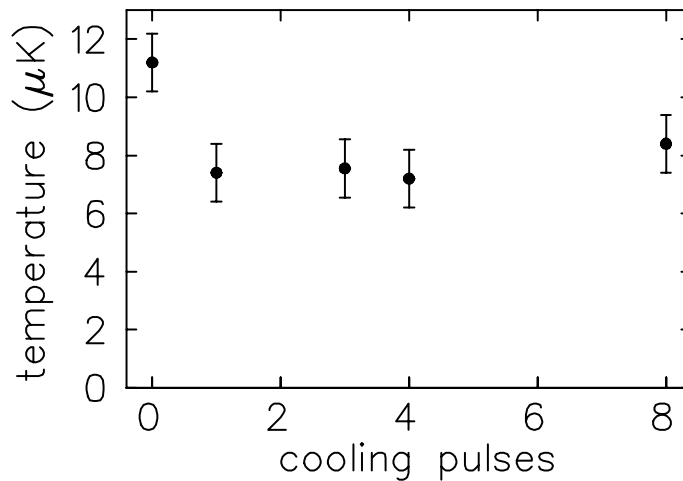


Figure 7.6: Applying 3 ms pulses of blue-detuned molasses cooling inside the QUEST. The temperature versus number of molasses pulses is given. The detuning was $\delta = +5\Gamma_{Cs}$ with respect to the $F = 3 \rightarrow F' = 2$ transition.

We clearly observed a cooling effect. Starting from $12 \mu\text{K}$ the final temperature of about $6\text{--}7 \mu\text{K}$ is reached after 3 cooling pulses. The data presented in Fig. 7.6 was taken for a cooling detuning of $\delta = +5\Gamma_{Cs}$ with respect to the $F = 3 \rightarrow F' = 2$ transition and at an intensity of about $3 \times I_0$. These values combined an optimum cooling effect and moderate particle loss. Since the detuning is a few linewidths only, the reached temperature was sensitive to variations of less than one linewidth.

In order to prove the cooling effect for even higher initial temperatures, we increased the temperature at transfer to about $25 \mu\text{K}$ simply by cutting out the blue-detuned molasses phase during transfer. And again, after 3 cooling pulses, the temperature was reduced to $7 \mu\text{K}$. Since in this case the number of transferred particles is lower, we did not investigate the behavior of these initial conditions further.

Lower temperature limit inside the QUEST

Subjecting Cesium atoms to blue-detuned molasses in free space led to a final temperature as small as $1.7 \mu\text{K}$ (see appendix C). Whereas applying blue-detuned molasses cooling inside the QUEST leads to a typical temperature 4 times above the one achieved in free space.

All efforts we made to further reduce the temperature inside the quasi-electrostatic trap failed. The lower temperature limit of $6.5 \mu\text{K}$ turned out to be independent of the repumper detuning and repumper intensity. Also varying the timing of the cooling did not reduce the temperature any further. At this point we tried various schemes such as applying a pulse chain of $6 \times 0.5 \text{ ms}$ pulses, each separated by 4.5 ms off periods instead of a 3 ms continuous pulse. Respectively we varied the delay between two cooling pulses or applied more cooling pulses. Neither configuration did reduce the final temperature in the QUEST further.

Since the peak density reached in the QUEST is on the order of $4 \times 10^{11} \text{ atoms/cm}^3$ we considered the occurrence of photon reabsorption as a temperature limiting source. But reducing the number of atoms, and therefore the density, in the QUEST and applying our cooling scheme resulted in the same lower limit for the temperature.

Hence the question arises: how can the discrepancy between the lower limits of the final temperature in free space and inside the QUEST be understood?

The optical dipole potential of the CO_2 -laser influences the cooling process. One might consider the spatially varying light shift of the CO_2 -laser trap acting on the cooling transition (see Fig. 3.7) as a reason for the discrepancy, since the final temperature depends on the detuning of the molasses field [Boi96]. But this effect is too weak, since the light shift of the CO_2 -laser varies only by about 15 % over the spatial distribution of the Cesium atoms around the center of the QUEST potential. A more reasonable explanation is connected to the intensity fluctuations of the CO_2 -laser. The oscillation frequencies of the atoms in the molasses potential wells are different from the oscillation frequencies in the QUEST. Therefore possible CO_2 -laser intensity noise in that spectral region leads to parametric heating of the atoms only in presence of the molasses field. The noise in the light shift of the atomic transition caused by the intensity noise of the CO_2 -laser leads to fluctuations of the relative detuning of the molasses field. Hence one can regard the light shift of the molasses field as the mediator of the heating process, caused by the CO_2 -laser intensity noise. Therefore the cooling process competes with an additional heating mechanism and one would expect the lower limit of the Cesium temperature in the QUEST to be significantly above the corresponding temperature limit in free space molasses.

Since the noise spectrum of the CO_2 -laser is unknown, the statements above are only speculation.

Chapter 8

Simultaneous trapping of Cesium and Lithium

After having investigated collisions between ground state atoms of the same species (sec. 6.1 and 6.2), the next natural step is to study processes involving atoms of different species in the ground state. The quasi-electrostatic trap represents a unique tool to study ground state collisions between different atomic species. The absence of magnetic fields allows us to prepare the atoms in any ground state sublevel. Especially the possibility to store the atoms in their absolute hyperfine structure ground state distinguishes this trap from magnetic traps. In this section the first results on simultaneous trapping of Cesium and Lithium in the CO₂-laser trap are displayed. As a first step we decided to investigate hyperfine structure changing ground state collisions. Via optical pumping the Cesium atoms were prepared in the upper $F = 4$ and lower $F = 3$ ground state. The results presented here must be regarded more as a status report than a description of a complete series of experiments.

In the first part of this chapter the loading of the combined QUEST is introduced, and in the second part first results on interspecies ground state collisions in the Cs-Li system are shown.

8.1 Combined transfer of Cesium and Lithium

Combining Cesium and Lithium in the QUEST is a challenging experimental task, not only because the two species behave so differently, but also due to their possible destructive interaction [Wal94]. Even though the transfer schedules of both candidates are similar, a synchronous MOT loading and transferring would not be promising due to light-induced inelastic collisions, opening additional loss channels.

The simultaneous trapping of Lithium and Cesium in a MOT was closely investigated by our group [Sch99, Sch98a]. The existence of Cesium in its excited state causes strong trap loss for both species, since the interspecies potential is attractive. Inelastic collisions, changing the Ce-

sium excited state hyperfine structure or fine structure population, release sufficient energy to repel both collision partners from the MOT as well as from the QUEST. Such processes not only limit the absolute number of atoms in the MOT during the loading phase to a low level, but also induce losses during the transfer phase, while Cesium is cooled in a blue-detuned optical molasses for several milliseconds.

Therefore transfer into the dipole trap has to be done separately and in a way, such that no Cesium excitation is involved when Lithium is present. This led us to a procedure in which, under the absence of Lithium, firstly Cesium is accumulated in the MOT and transferred into the QUEST. After a short time, allowing for optical pumping and cooling of Cesium in the QUEST, the Lithium MOT gets loaded, while Cesium is still trapped in the QUEST, but populating one of its ground state sublevels. This way we make use of optical shielding processes. The interaction potential between Lithium in the excited state and Cesium in its ground state is repulsive, preventing losses due to inelastic collisions.

The sequenced loading of Cesium and Lithium into the QUEST allows for following the optimized procedures described in section 5.2 and 5.3. Neither turning on the magnetic quadrupole field ($\mu_B B_{MOT} \ll U_0^{Cs}$), nor the off-resonance scattering rate (1 photon per month) from the operation of the Lithium MOT leads to irritation of the Cesium in the optical dipole potential of the QUEST. Fig. 8.1 illustrates the typical timing of the combined transfer into the QUEST.

At the current state of the experiment, we trap 10^3 Lithium and 3×10^4 Cesium atoms simultaneously in the QUEST. The smaller Cesium number as compared to our single species experiments, is mainly due to inelastic collisions of Cesium in the QUEST with the Lithium atomic beam during the Lithium MOT loading. Therefore the Lithium MOT was loaded only for a short time (1.5 s). This compromise results in smaller numbers of Lithium in the transfer MOT and therefore in the QUEST. On the other hand, only a moderate loss of Cesium from the QUEST is experienced.

Improvements on these numbers are possible. Since the volume of the dipole trap is relatively small, the beam scattering problem can be circumvented by implementing a small anti-aperture in front of the QUEST to block the Lithium atomic beam. Since the trapping volume of the MOT is much larger than the QUEST volume, no significant influence on the loading rate of the Lithium MOT is expected.

The influence of the Cesium atomic beam on the Cesium sample in the QUEST was of much less strength, since the total flux is much smaller than in the case of Lithium. Nevertheless, an anti-aperture for this beam should also be considered.

Due to the small Lithium density ($\bar{n}_{Li} \approx 10^5 \text{ cm}^{-3}$) inside the QUEST, a loss mechanism due to interaction with the atomic beams was not experienced on the Lithium ensemble.

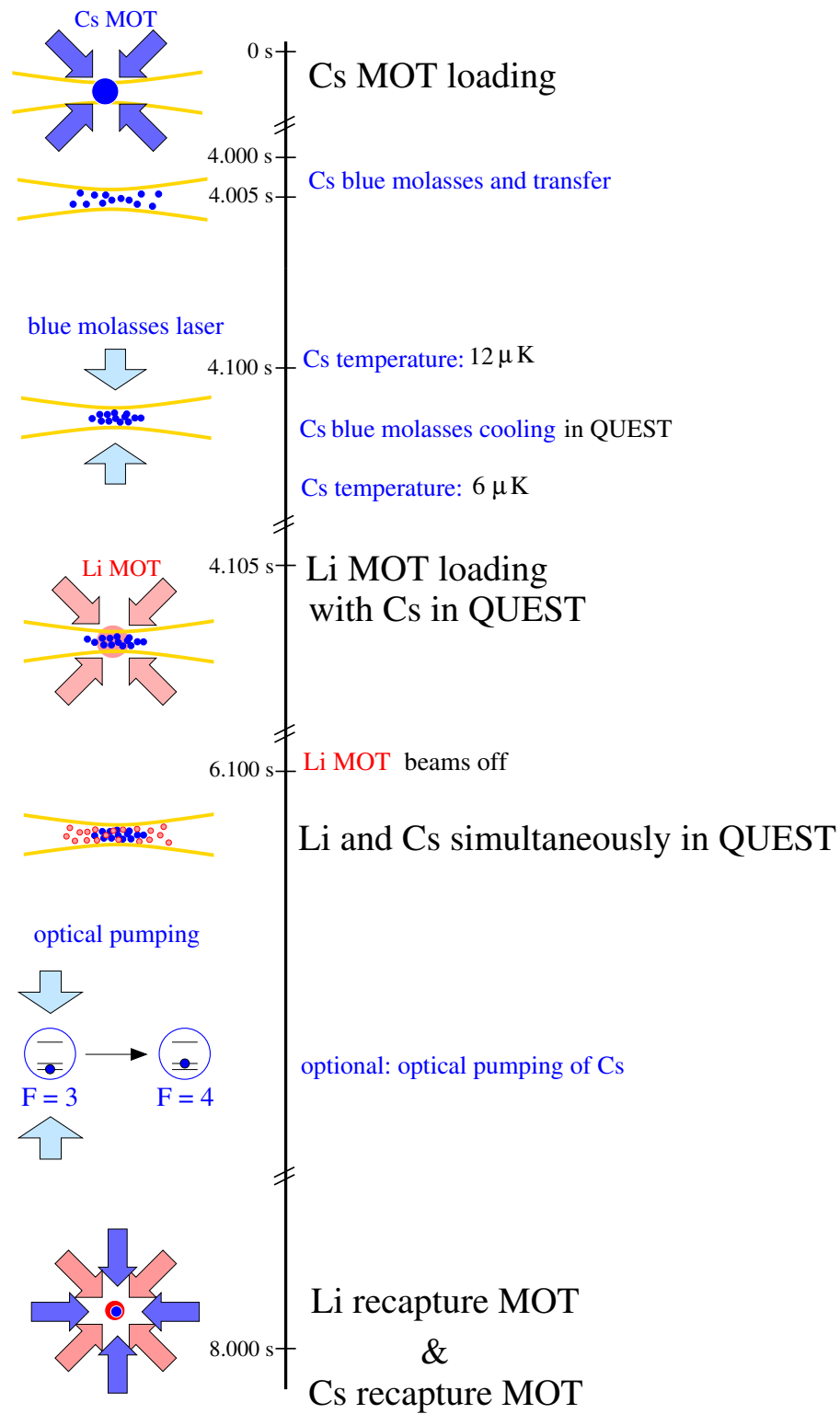


Figure 8.1: Illustration of the combined transfer into the QUEST. The sequenced loading of Cesium followed by Lithium allows for retaining the optimized procedures of the single transfers.

8.2 Inelastic interspecies ground state collisions

This section reports on first experiments about inelastic ground state collisions between Lithium and Cesium in the QUEST.

We started this sequence of experiments by measuring the decay of the trapped particles. When one species is prepared in the upper ground state, one expects stronger particle loss due to hyperfine structure changing collisions. For a Li-Cs collision, the mass ratio predicts that 95% of the released hyperfine energy will be transferred to the Lithium atom. Nevertheless, due to the small trap depth, both collision partner will escape from the QUEST.

Since the interaction cross-section of the Li-Cs system is unknown, one of the most important questions was, whether at the densities ($\bar{n}_{Li} \approx 10^5 \text{ cm}^{-3}$, $\bar{n}_{Cs} \approx 10^9 \text{ cm}^{-3}$) and particle numbers currently achieved in the QUEST ($N_{Li} = 10^3$, $N_{Cs} = 3 \times 10^4$), we would be able to find a signature of Li-Cs interactions.

We measured the decay of the trapped particle number for both species. In the first run Lithium and Cesium were prepared in the energetically lowest hyperfine ground state ($F_{Li\downarrow} = 1$, $F_{Cs\downarrow} = 3$).

In a second measurement we prepared the Cesium atoms in the upper hyperfine ground state ($F_{Cs\uparrow} = 4$) by an optical pumping pulse, while Lithium remained in the lower hyperfine ground state. From the difference in the associated decay curves one sees evidence for inter-species inelastic processes. In particular, signatures for inelastic processes in the Lithium decay can only result from collisions with Cesium atoms, since Lithium still populates the absolute energetic ground state.

The evolution of the Cesium and Lithium particle number as a function of storage time is shown in Fig. 8.2. Open symbols represent the particle number for both atoms in the absolute energetic ground state ($F_{Li\downarrow} = 1$, $F_{Cs\downarrow} = 3$), while the full symbols give the number of atoms for Cesium being pumped to the upper hyperfine ground state ($F_{Li\downarrow} = 1$, $F_{Cs\uparrow} = 4$). In the case of Cesium being in its absolute ground state, an exponential fit to the data yields a $1/e$ lifetime of $\tau_{Cs\downarrow Li\downarrow} = 45 \text{ s}$ for the Cesium particle number, and $\tau_{Li\downarrow Cs\downarrow} = 26 \text{ s}$ for the Lithium particle number. These storage times are considerably smaller than the time constants for the single-species trapping in the QUEST, presented in chapter 6.1 and 6.2. This is surprising, since inelastic processes should be excluded by the fact that both species are prepared in the absolute ground state. The reason for this behaviour is still not clear and will be subject of further experimental investigation.

For Cesium populating the upper hyperfine ground state, one clearly observes a faster decay of both particles numbers. The associated $1/e$ lifetimes for Cesium are $\tau_{Cs\uparrow Li\downarrow} = 34 \text{ s}$ and for

Lithium we find $\tau_{Li\downarrow Cs\uparrow} = 14$ s. The slightly decreased lifetime for the Cesium ensemble can be mainly attributed to hyperfine structure changing collisions within the Cesium system, when one or both Cesium atoms are prepared in the upper hyperfine ground state. Due to the much smaller number of trapped Lithium atoms, inelastic $Li\downarrow - Cs\uparrow$ collisions practically have no influence on the Cesium particle number.

The faster decay of stored Lithium atoms can be explained by hyperfine structure changing $Li\downarrow - Cs\uparrow$ collisions. The data is still preliminary and we are currently improving the measurements to provide rate coefficients and cross-sections.

Nevertheless, Fig. 8.2 unambiguously provides for the first time evidence of pure ground state collisions between two different atomic species.

The case of Lithium being in the upper hyperfine ground state was not investigated, since the Lithium number and density in the quasi-electrostatic trap is small and an effect on the Cesium sample will be hard to detect. For future experiments, with improved Lithium numbers, one can expect an additional trap loss due to the released Lithium hyperfine energy of $h \times 803$ MHz $\hat{=} k_B \times 40$ mK in inelastic Li-Cs collisions. Even such small energies will be sufficient to cause trap loss of both collision partners: $\Delta E_{Li} = 38$ mK $\gg \Delta E_{Cs} = 2$ mK $\gg U_0 = 0.1$ mK.

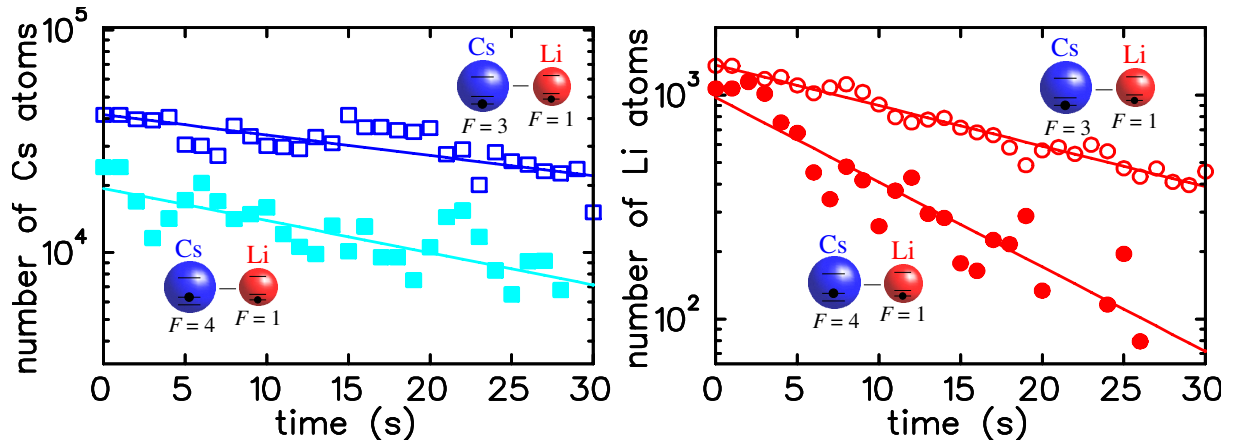


Figure 8.2: Interspecies hyperfine structure changing collisions between Lithium and Cesium atoms in the QUEST. The graphs show the evolution of the particle number of simultaneous trapped cesium (left) and Lithium (right) with time. Open symbols represent the particle number for both atoms in the absolute energetic ground state ($F_{Li\downarrow} = 1$, $F_{Cs\downarrow} = 3$), while the full symbols give the number of atoms for Cesium being pumped to the upper hyperfine ground state ($F_{Li\downarrow} = 1$, $F_{Cs\uparrow} = 4$).

Chapter 9

Status and prospects

The quasi-electrostatic trap is an outstanding tool to investigate the interaction of neutral atoms prepared in any ground state sublevel. For the first time the simultaneous trapping of two different species and their elastic as well as inelastic scattering was demonstrated. In principle mixtures of any atomic species and even molecules can be stored and manipulated in the QUEST.

We have studied the transfer of magneto optically trapped Cesium and Lithium into our QUEST, which is realized by an industrial grade 30 W CO₂-laser. Storage times on the order of several minutes were realized. Elastic as well as inelastic ground state collisions within one single species were investigated. The corresponding quadratic loss parameters are: $\beta_{Cs} = 2.2 (\pm 0.4) \times 10^{-11} \text{ cm}^3/\text{s}$. and $\beta_{Li} \simeq 6 \times 10^{-10} \text{ cm}^3/\text{s}$.

For Cesium we observed evaporative cooling from a temperature of 25 μK to 12 μK within 200 s. With respect to the relatively small density of about 10^{10} cm^{-3} the observation of evaporative cooling was only possible by the combination of very long storage times, the absence of heating processes and the unusual large elastic scattering cross section in ultra cold Cs-Cs ground state collisions [Arn97].

By applying polarization-gradient cooling on the Cesium ensemble inside the QUEST we reduced the temperature to about 6.5 μK . Here we took advantage of the unique properties of a quasi-electrostatic trap which allows one to manipulate the internal degrees of freedom (optical pumping) of the atoms without affecting the trapping potential.

We saw a clear signature of inelastic interspecies ground state collisions when Cesium and Lithium were together confined in the QUEST. Currently we trap 3×10^4 Cesium atoms and 10^3 Lithium atoms simultaneously in our CO₂-laser trap. These numbers are partly limited by inelastic scattering with the atomic beams during MOT loading and by light assisted collisions during the loading of the Lithium MOT, whereas Cesium is stored in the QUEST. When studied separately two orders of magnitude more atoms are captured by the QUEST.

Hence improvements in the simultaneous transfer, such as implementing an atomic beam block, should lead to higher numbers of simultaneously trapped particles. Currently a new transfer

scheme is tested, based on a displacement of the Lithium MOT during the loading. This is accomplished by an additional magnetic bias field. When the quadrupole field is shifted along the radial coordinate of the dipole trap, the Lithium MOT can be loaded well above the Cesium cloud stored in the CO₂-laser focus, reducing the rate of light assisted collisions. After sufficient loading the atomic beam is turned off and, by shifting the bias field, the Lithium sample is also transferred to the QUEST.

In order to reach in general higher particle numbers we will replace the current 30 W CO₂-laser by a new laser, providing 120 W output power. From the simulations of the transfer efficiency (see section 5.1) we expect a 10-fold increased number of stored Lithium atoms and a factor of two more Cesium particles.

The increased number of simultaneously stored particles opens up new vistas for investigations of interspecies ground state interactions, such as elastic collisions and sympathetic cooling of Lithium by Cesium. So far no information on elastic collision properties of the Li-Cs system is available. From the thermalization rates between the two gases cross sections and scattering length can be deduced. With the polarization-gradient cooling scheme introduced in section 7.2 we can cool Cesium down to 6.5 μ K inside the QUEST. Because of its high recoil temperature this technique would not work efficiently on Lithium. If it is possible to transfer the Cesium temperature to the Lithium sample, the way to physics in the regime of quantum degeneracy outside a magnetic trap would be open not only for the bosonic isotope ⁷Li, but also for the fermionic isotope ⁶Li. Bose-Einstein condensation with ⁷Li has already been demonstrated in magnetic traps [Bra95, Bra97]. In magnetic traps only atoms in the upper hyperfine ground state are captured. Due to the attractive interaction between the Lithium atoms in the magnetically trapped state, only a condensate of about 2000 atoms can be formed. In a QUEST the atoms can be prepared in their absolute ground state where a repulsive interaction is present and for which larger condensates can be studied. Using Cesium as a cold reservoir, it should be possible to reduce the Lithium temperature inside the QUEST via elastic collisions (sympathetic cooling) with the Cesium atoms to a few μ K on time scales short compared to the demonstrated storage times. For an assumed temperature of 5 μ K Lithium will have a de Broglie wavelength of about 1 μ m. Therefore, for Lithium the quantum-degenerated regime ($n\Lambda_{th}^3 \geq 1$) will be reached at moderate densities of 10¹³ atoms/cm³. These densities will be hard to achieve in a simple focused beam trap, due to the weak confinement along the laser propagation axis. A better option will be a trap formed by two focussed beams crossing under right angle [Gri00]. We possess already two CO₂-lasers and the design of the vacuum chamber gives us the opportunity to realize a crossed-beam configuration, hence such a setup is considered for future experiments.

A second challenging topic is the formation of ground state molecules via photoassociation. As described in [Wei00, Sch99], we performed photoassociation experiments in the MOT already. Photoassociation on cold heteronuclear dimers has not been reported so far. Photoassociation

of Li-Cs dimers would be a major step towards the formation of more complex molecules. In contrast to our experiments in the two species MOT, where we were limited by various fluctuations associated with the MOT light, in the QUEST trap-loss signals through photoassociation should be background free. The new detection method will be based on photoionization of the molecules. The architecture of the new vacuum apparatus allows for implementation of a channeltron ion-detector.

The Li-Cs dimer is expected to have a large internal dipole moment. It can serve as a prototype molecule for the development of manipulation techniques based on electrostatic fields. Electrostatic cages for the storage of cold polar molecules could be designed and tested with the Li-Cs dimer.

Appendix A

B-field compensation by ground state Hanle effect

This section gives information on the magnetic field adjustment. The presence of a residual magnetic field $\vec{B}_{res} = (B_x; B_y; B_z)$ at the location of the trapped atoms limits the temperature achievable with polarization-gradient cooling to $\approx \vec{\mu}_B \vec{B}_{res}$. Hence it is important to have a sensitive method to minimize the magnetic field in the area of the trapped atomic sample (inside the vacuum system). The method we employed makes use of the ground state Hanle effect [Mor91]. It relies on the ground state sub-level mixing of Cesium in presence of a magnetic field.

The classical Hanle effect Consider an atomic sample illuminated resonantly by linearly polarized light. The emitted fluorescence light is detected perpendicular to the incident light beam and perpendicular to its polarization. Under absence of external magnetic fields, the detected fluorescence light is linearly polarized along the same direction as the incident light. Wood and Ellett observed in 1923 that the presence of a magnetic field parallel to the direction of detection strongly affects the polarization degree of the fluorescence light. The polarization degree is defined as $P = (I_p - I_o)/(I_p + I_o)$. Where I_p and I_o denote the detected intensities with polarization parallel respectively orthogonal to the one of the incident light. The first quantitative description was given by Eldrige:

$$P = \frac{1}{1 + (e B \tau / m_0)^2}, \quad (\text{A.1})$$

where e is the electron charge, m_0 the electron mass, B the magnetic field along the direction of detection and τ the lifetime of the atomic excited state. This relation gives with the knowledge of B exact values for excited state lifetimes.

The semi classical interpretation of this effect relies on the coherent superposition of atomic states. Consider a $J = 1$ state: under the presence of magnetic fields perpendicular to the polarization

axis of the incident light, a coherent state $(|m = -1\rangle + |m = +1\rangle)/\sqrt{2}$ is formed, as long as the Zeeman splitting is less than the natural linewidth of the transition. The formation of a coherent state between magnetic ground state sublevels is exactly what we make use of, when equalizing the magnetic field. Going back to the classical Hanle effect, from Eq A.1 one can see: for “long” lifetimes τ , as realized in the ground state, the polarization degree P is determined by the magnetic field only.

The ground state Hanle effect The method we used is described on a $J = 1 \rightarrow J' = 0$ transition in the classical picture and illustrated in Fig. A.1. Consider an atom subjected to a light field with linear polarization along the z -axis, which represents the quantization axis. If no transversal magnetic fields are present, according to the selection rules for electrical dipole transitions, the atom will be pumped either into the $|m = -1\rangle$ or $|m = +1\rangle$ state, and hence be decoupled from the light field. The atom now populates a “dark state”, meaning that light is no longer absorbed by the atom.

When transversal magnetic fields are present, a mixing of all ground state sublevels is induced by the Larmor precession of the atomic dipole moment, resulting in an exchange of population between the sublevels. Hence the atomic cloud appears not transparent any more. The mixing is regarded in the following as a coupling between the ground state sublevels.

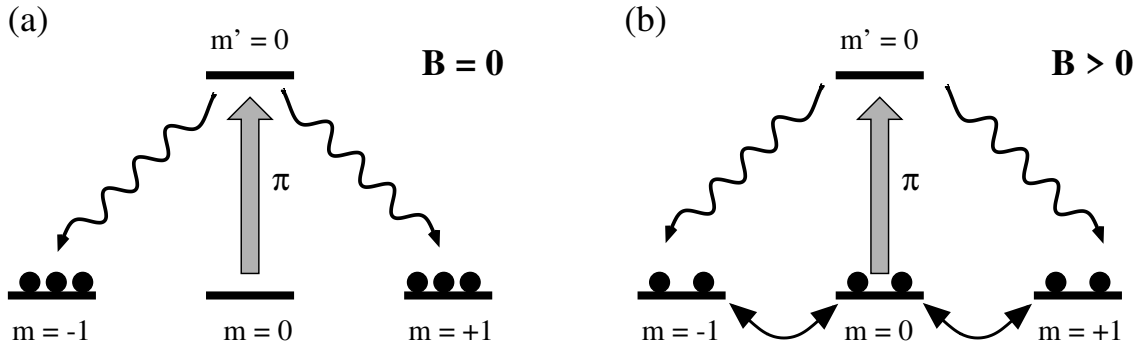


Figure A.1: *Illustration of the dark state resonance. Considering a $J = 1 \rightarrow J' = 0$ transition, the direction of polarization defines the quantization axis. For π polarized light, the $|m = -1\rangle$ and $|m = +1\rangle$ substates are decoupled from the light field, hence they are called dark states (a). In the presence of transversal magnetic fields, the Larmor precession couples the $|m = -1\rangle$ and $|m = +1\rangle$ substates to $|m = 0\rangle$ (b). Therefore the population is exchanged between all ground states.*

The experimental setup is illustrated in Fig. A.2. A weak probe laser was pointed through the atomic cloud, retroreflected (to avoid light pressure effects) and by a beam splitter directed to a photodiode. The probe laser was tuned on resonance with the $F = 3 \rightarrow F' = 2$ transition in Cesium and its absorption in the atomic cloud was monitored. The measurement was performed on a cold and dense Cesium sample in free space, 1 ms after release from the MOT, to make sure the MOT quadrupole field has vanished.

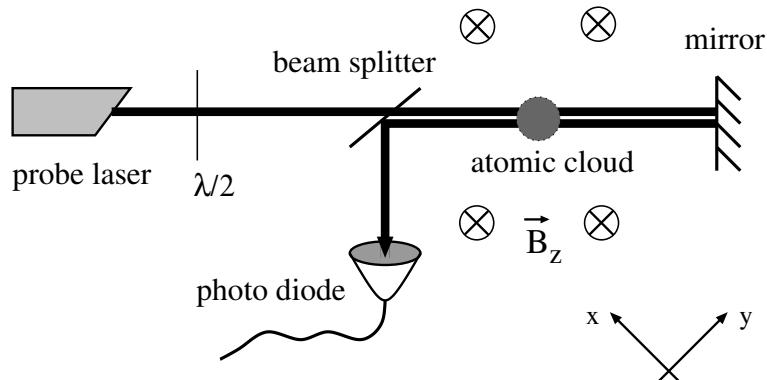


Figure A.2: Illustration of the experimental setup for the dark state method used to equalize the magnetic field in the area of the trapped atomic sample, \vec{B}_z denotes the ramped magnetic field field. The half wave plate is used to adjust the linear polarization of the probe beam.

First, for a coarse adjustment, the laser field is in the x - y -plane, its polarization vector \vec{E} perpendicular to it. The fields in x -axis B_x and y -axis B_y are adjusted, while ramping the magnetic field in z -axis B_z , parallel to \vec{E} . As long as B_z is much larger than B_x resp. B_y , the resulting field is almost along the z -axis. The ground state sublevels are decoupled from each other and the population is prepared in the dark states $|m = \pm 1\rangle$. No light is absorbed. As B_z decreases the transversal fields get more and more influence on the resulting field and the ground state sublevels couple to each other (see Fig. A.1), hence light gets absorbed again. The absorption signal in Fig. A.3 shows a peak at the region where $B_z^2 \lesssim B_x^2 + B_y^2$. Repeating the ramping and adjusting the current through the x - y -compensation coils the absorption peak is maximized in height and its width narrowed. With this treatment the total magnetic field was equalized to about 100 mG.

Secondly, for the fine tuning the laser field still is in the x - y -plane, but the polarization \vec{E} is rotated into the x - y -plane. Now \vec{E} is not parallel to the magnetic field of any of the compensation coils. Again, B_z is ramped but this time on a smaller amplitude, since the fields are coarsely adjusted. When decreasing B_z , the total magnetic field decreases and the $|m = -1\rangle$ and $|m = +1\rangle$ sublevels decouple more and more from the $|m = 0\rangle$ sublevel. Due to optical pumping the absorption decreases and the atomic sample becomes transparent. The absorption signal in Fig. A.4 shows a dip in the region where $B_z^2 \lesssim B_x^2 + B_y^2$. Again, by repeating the ramping of B_z and fine tuning the current through the x - y -compensation coils, the absence of absorption is maximized and its width narrowed. From the width of the dip in the lower curve in Fig. A.4, one can estimate that the total magnetic field is equalized to a few 10 mG, corresponding to a magnetic energy $\vec{\mu}_B \vec{B}$ of a few μK times k_B .

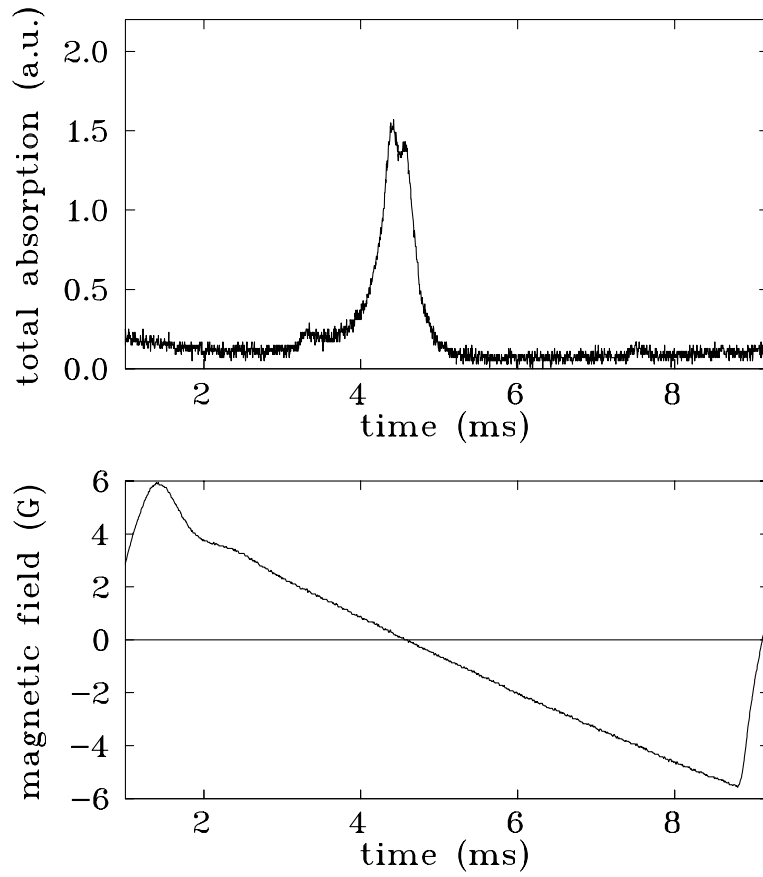


Figure A.3: The **upper** picture shows the absorption of the trapped atoms. Higher values correspond to stronger absorption. In the **lower** picture the associated sweep of the magnetic field B_z parallel to the polarization \vec{E} is given.

The value of the current through the coils of the ramped field B_z is finally set to the corresponding current in the region of the dip. The equalization of the total magnetic field is confirmed by the measured temperatures of the Cesium atomic sample in our gray molasses of $1.7 \mu\text{K}$.

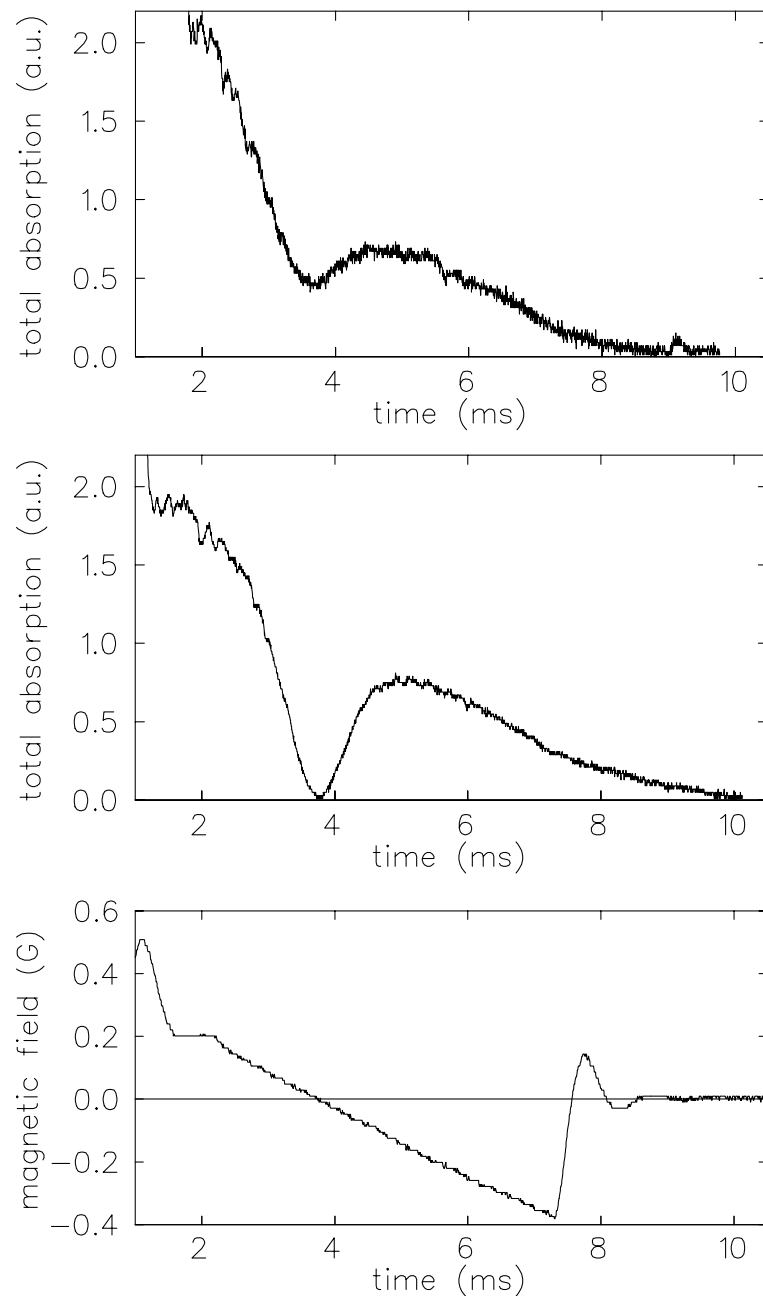


Figure A.4: The **upper** picture shows a dip in the absorption signal, when B_x and B_y are almost equalized and B_z is ramped through zero. The **middle** picture displays the same case, but for better adjustment of B_x and B_y . The **lower** picture displays the ramped magnetic field. When B_z reaches zero, the absorption vanishes completely. Higher values correspond to stronger absorption, the curves are descending to the right, because atoms are leaving the interaction region during the sweep, at the right end of the sweep all atoms have left the interaction region. Therefore one clearly sees, the bottom of the absorption dip corresponds to zero absorption.

Appendix B

Magnetic fields of the new apparatus

In the following a documentation of the new magnetic field setup is given. The given values and parameters are the ones used during all experiments introduced in this thesis.

First the magnetic field for magneto-optical trapping is displayed, followed by the magnetic field for the compensation of residual fields. The last two sections cover the magnetic field setup of the Zeeman-slower sections, including the most important atomic beam properties.

B.1 MOT magnetic field

The mechanical setup of the new, compact MOT coils is detailed in section 3.4.3 already. Here I will focus on the magnetic field of the MOT. The windings have an inner diameter of 16 cm and an outer diameter of 18.5 cm. The distance between the coils is 16 cm, each coil consists of 67 windings.

In Fig B.1 the designed field of the anti-Helmholtz coils is given for a current of 30 A. The picture to the left shows the field in x - y -plane (horizontal plane), in which the atomic beams propagate. The calculation is based on [Sch73] and takes the cross-section of the coils into account. On the right side the vertical field, along the symmetry axis of the quadrupole, is given. It is calculated from integrating Biot-Savard's law.

To see if the MOT field in our experimental setup meets the designed values, we measured the field in the x - y -plane. Fig. B.2 shows the nice matching with the solid curve, representing the calculated field. An adjustment of the current was not necessary. The behaviour of the field in the vertical axis was not measured.

For magneto-optical trapping the gradient of the quadrupole field is as interesting as the field itself, since the gradient determines the stiffness of the MOT potential. In Fig. B.3 the gradient of the designed MOT field is shown. To the left one finds the gradient in the x - y -plane and to the

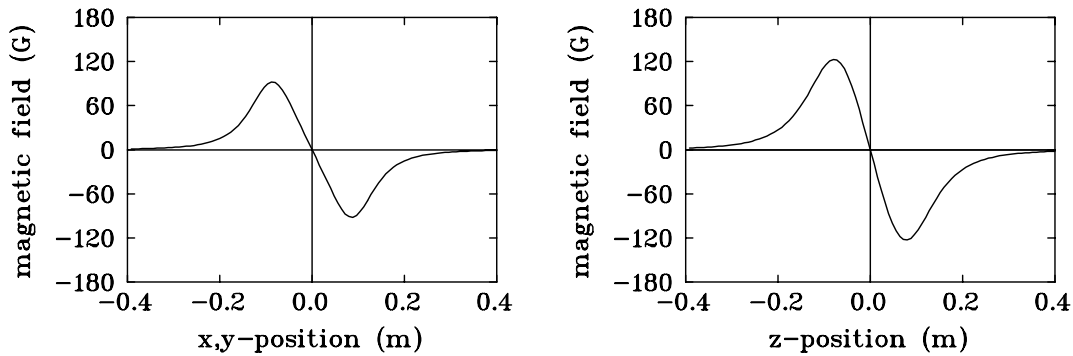


Figure B.1: Calculated magnetic field of the MOT quadrupole field for a current of 30 A. The trap center is located at the origin. The **left** picture shows the field in x-y-plane, in which the atomic beams propagate. On the **right** side the vertical field is shown.

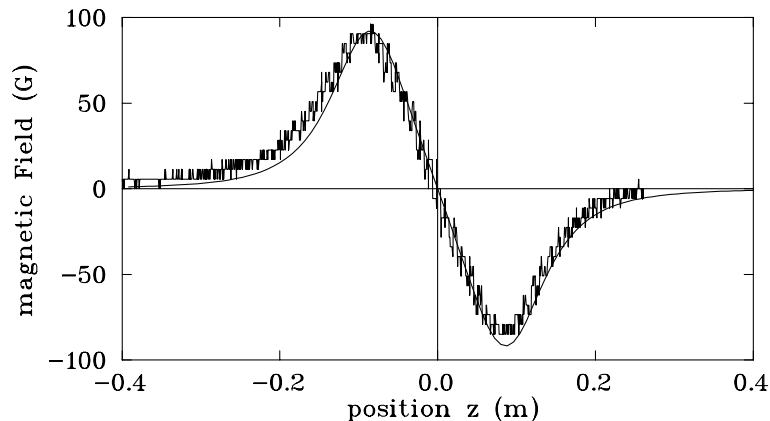


Figure B.2: Cross-check of the actual MOT field in the x-y-plane with the designed (solid line) field.

right the one in vertical direction. In the area of interest the field gradient long the symmetry axis is 26 G/cm, in any perpendicular direction 13 G/cm.

B.2 Magnetic field for compensation of residual fields

In the present section the compensation fields are characterized. We implemented 3 independent pairs of coils to compensate non-controllable fields. These compensation coils are operated in Helmholtz configuration. The windings are supported by a large box (dimension of $1.60 \times 1.10 \times 0.80$ m), centered on the main chamber. Each coil has 96 windings.

Table B.2 gives the orientation and dimension of the coils, the measured magnetic field at the center of the box (which is approximately the area of the MOT) for a current of $I = 5$ A, and the electrical resistance.

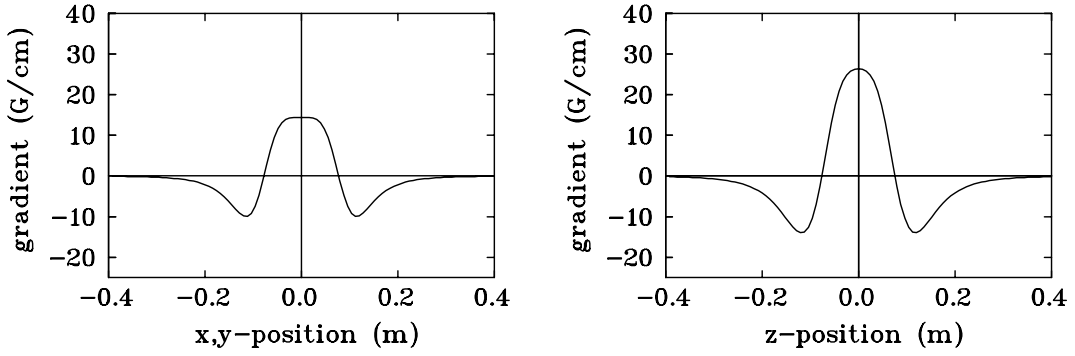


Figure B.3: Gradients of the MOT field. On the **left** side the gradient in the x-y-plane and on the **right** side the one in vertical direction is given.

number	field orientation	dimension [m]	magnetic field [G]	resistance [Ω]
1	horizontal	1.15×0.8	2.3	7.2
2	horizontal	1.3×0.8	3.8	9.2
3	vertical	1.15×1.3	6.0	10.4

Table B.2: Relevant parameters of the compensation coils (96 windings).

The magnetic field corresponds to a current of 5 A.

Fig. B.4 shows the calculated magnetic field of each pair along the axis connecting the center of both coils. The assumed current is 5 A.

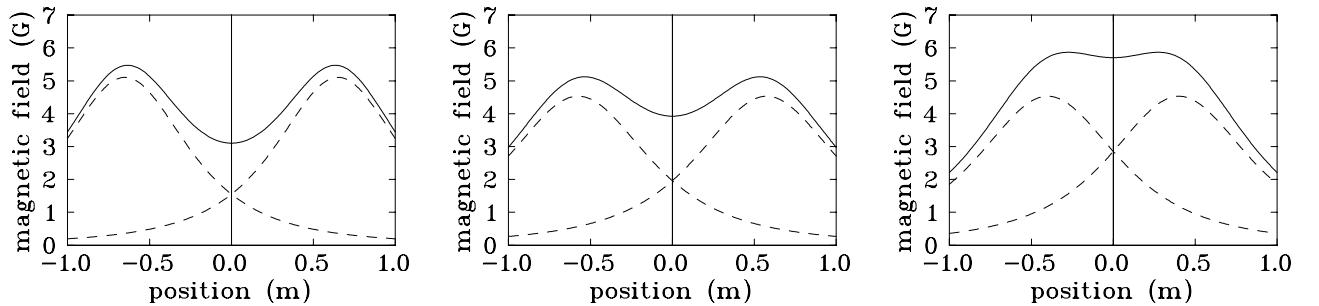


Figure B.4: The calculated magnetic field of each pair of compensation coils (96 windings) for a current of 5 A. Dashed lines indicate the field generated by a single coil, the solid lines denote the total field. The **left** picture shows the field of pair number 1, in the **middle** we see the field of pair number 2, and to the **right** the field of pair number 3 is displayed.

The properties described so far refer to the full number of 96 windings per coil. In order to adjust residual magnetic fields sensitively, we separated 32 windings from each coil of pair number one and 16 windings from pair number two. Pair number 3 (vertical direction) was not changed.

To fine tune the field in vertical direction, we used the extra turns around each of the main MOT coils (35 turns each). This pair of coils is labeled number 4 in the following. The main part of each coil is powered by stabilized commercial power-supplies. The separated windings and pair number 4 are operated by self-made electronics, which allows for a sensitive fine adjustment of the current.

The sensitivity of the fine adjustment is as follows: A current of 1 A in the 32 windings of pair number 1 corresponds to a magnetic field of 153 mG, in the 16 windings of pair number 2 to 127 mG and in pair number 4 to 2400 mG. The maximum current available is 3.5 A.

B.3 New Lithium Zeeman-slower section

All aspects concerning the mechanical and electrical setup of the Lithium Zeeman-slower are detailed in [Eng97].

For the present experiment some modifications on the magnetic field were made. In this work the quantities of the current magnetic field and the resulting beam parameters are introduced.

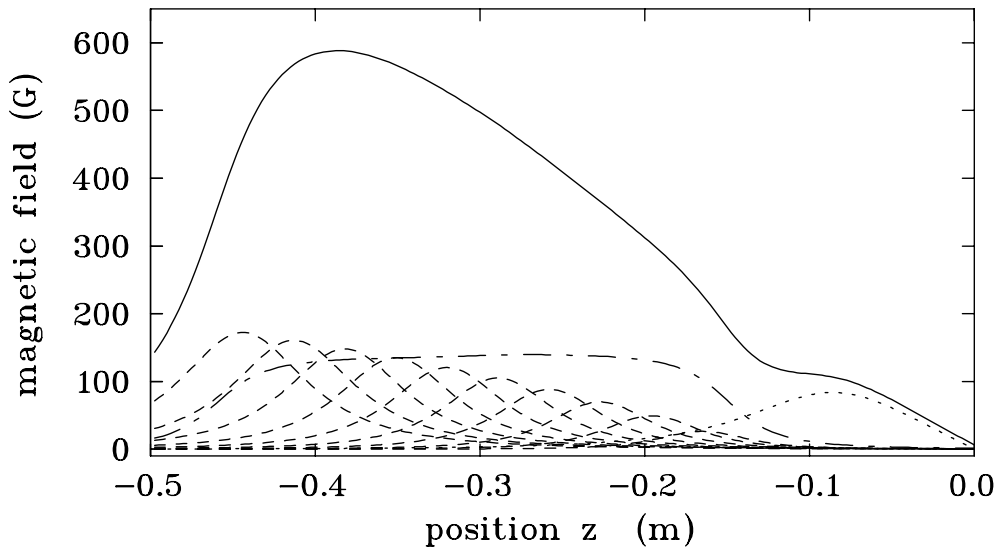


Figure B.5: Calculated longitudinal magnetic field of the Lithium Zeeman-slower section, including the MOT field. The solid line shows the resulting, total field. The dotted line indicates the MOT field, the dashed lines correspond to each of the ten segments of the solenoid. The dash-dotted line shows the field contribution of the offset windings inside the solenoid. The trap center lies in the origin, the solenoid is placed between $z = -0.17$ m and $z = -0.48$ m.

Fig. B.5 shows the simulation of the current Zeeman-slower field in direction of atomic beam propagation (in the x - y -plane). Details about the calculations are given in [Eng97]. The solid line shows the resulting total field. The dotted line indicates the MOT field, the dashed lines correspond to each of the ten segments of the solenoid. The dash-dotted line shows the field

contribution of the offset windings inside the solenoid. The corresponding currents assumed in the simulation are: $I_{MOT} = 30$ A, $I_{solenoid}^1 = 6.7$ A and $I_{offset} = 1.2$ A.

One nicely sees the smooth transition between Zeeman-slower field and MOT field.

To cross-check the matching of the actual field with the designed field we measured the longitudinal field with a Hall detector. The nice agreement of the total fields is shown in Fig. B.6. The experimental values are: $I_{MOT} = 30$ A, $I_{solenoid} = 6.5$ A and $I_{offset} = 1.5$ A.

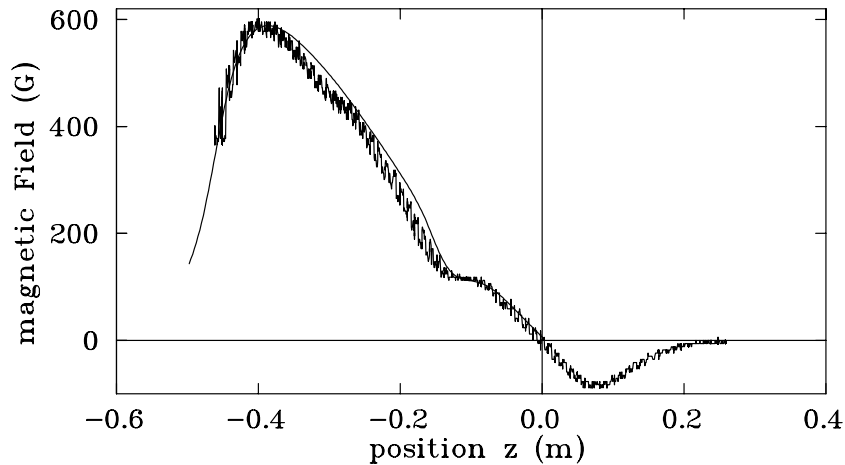


Figure B.6: Measurement of the longitudinal magnetic field in the Lithium section. The solid line corresponds to the designed field (displayed already in Fig. B.5). The trap center lies in the origin.

The corresponding beam parameters, such as maximum capture velocity, behaviour of the slowing force, transverse beam velocity and -radius versus deceleration length are illustrated in Fig. B.7. The curves shown in Fig. B.7 result from the integration of the equation of motion, using the calculated total magnetic field described above. The assumed slowing laser detuning is $-9\Gamma_{Li}$ and the saturation parameter is $S = 1$. In the upper left picture the behaviour of the resonance velocity is displayed. The maximum velocity decelerated in the Lithium Zeeman-slower is 600 m/s. The slowing process ends with a velocity of 45 m/s. Atoms with such speeds can easily be captured in the MOT. The resulting trap loading flux corresponds to typically 1% of the total atomic flux. In the lower left picture the behaviour of the associated decelerating force is shown. Desired is a constant force. In order to achieve reliable operation, the force must not exceed half of the maximum spontaneous force $\hat{F} = \hbar k \gamma$ (see Eq. 3.3). Both conditions are well fulfilled. In the upper right picture the transverse atomic velocity is given. From the beam shaping system in the differential pumping sections, the initial transverse velocity is 5 cm/s. Due to the random character of the emitted photon momentum, the transverse velocity increases with the square

¹This value denotes the current through the ten segments of the Zeeman-slower solenoid, which are connected in series.

root of the number of scattered photons. The resulting transverse beam radius is given in the lower right picture. Its maximum of less than 7 mm is by 2 mm smaller than the $1/e^2$ -intensity radius of the Lithium MOT laser beams. Therefore we can assume that all decelerated atoms are captured in the MOT.

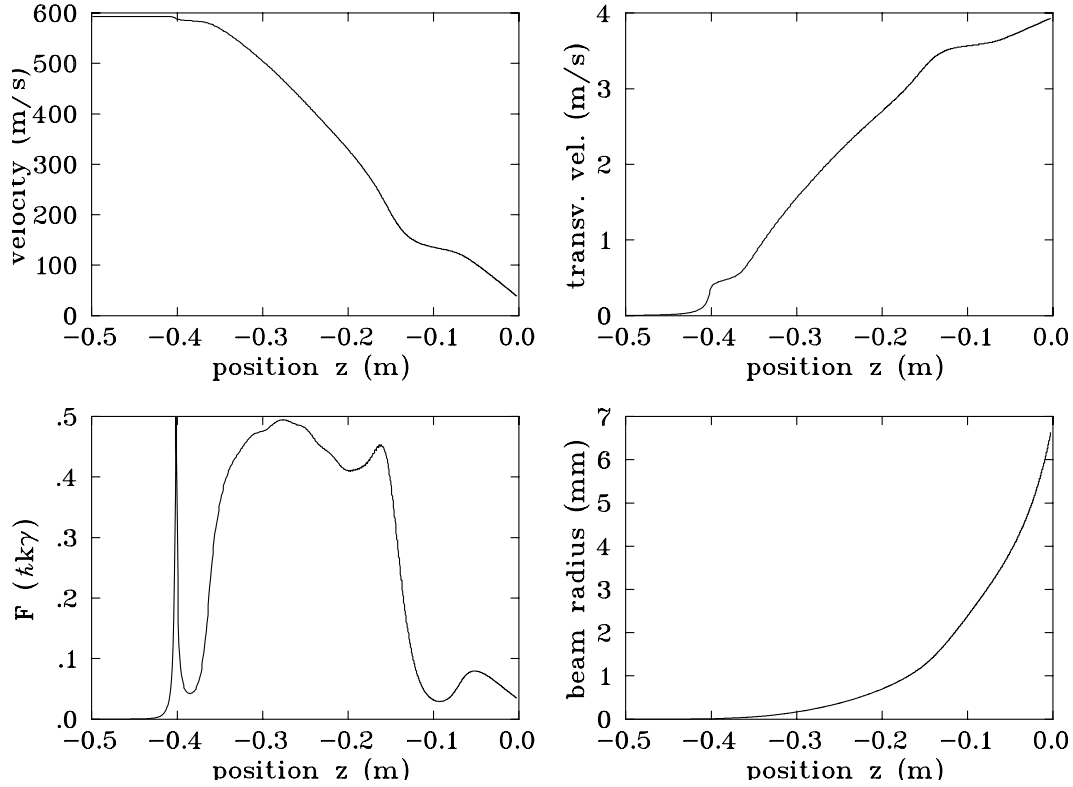


Figure B.7: Atomic beam quantities following from the designed magnetic field of the Lithium Zeeman-slower. In the **upper left** picture the atomic resonance velocity versus deceleration length is given. In the **lower left** picture the behaviour of the associated decelerating force is shown. The behaviour of the transversal velocity due to photon scattering is displayed in the **upper right** picture, and the resulting transversal blow-up of the atomic beam is shown in the **lower right** picture.

B.4 New Cesium Zeeman-slower section

In this section the basic quantities of the Cesium Zeeman-slower are introduced. Similar to the case of Lithium, the Cesium slower is designed as a “decreasing field slower” [Tho94, McA95], in a way that the ending tail of the slowing field fits smoothly into the quadrupole field of the MOT. The solenoid has a total length of 20 cm and consists of 3 independent segments to generate the gradient field and allowing for fine tuning. An additional coil allows for generating a homogeneous offset field. Fig. B.8 shows the mechanical setup.

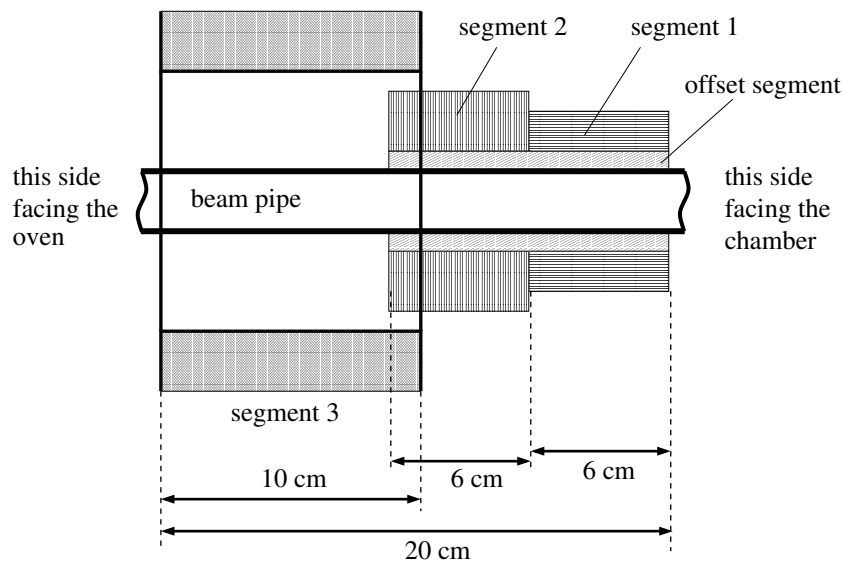


Figure B.8: Mechanical setup of the Cesium Zeeman-slower used in the current apparatus. Coils number 1 and number 2 have a length of 6 cm, coil number 3 has a length of 10 cm. The windings for an optional offset field lie inside of coil number 1 and number 2.

The windings for the offset field and segment number 1 and number 2 are turned directly around the atomic beam pipe, the ones of segment number three are supported by an aluminum cylinder, allowing for water cooling. Table B.4 gives the measured magnetic fields inside each segment², produced by a current of 1 A.

segment	1	2	3	offset
magnetic field [G]	12	26	64	7

Table B.4: Magnetic field inside each segment for a current of 1 A.

²The architecture of the Cesium Zeeman-slower section does not allow a measurement of the magnetic field, like in the case of the Lithium section. Therefore the measurements are taken with a Hall device at certain accessible spots only. The values given in table B.4 must be regarded as an estimation of the magnetic field. As it turned out, it is a very precise estimation.

In Fig. B.9 the designed shape of the longitudinal magnetic field, including the MOT field, is displayed. The dotted line indicates the MOT field, the dashed lines correspond to each of the 3 segments of the solenoid. In contrast to the Lithium Zeeman-slower where the same current runs through all segments, in the case of Cesium we use different currents for the segments. In the simulation the associated currents through each of the segments are: $I_1 = 2.4$ A, $I_2 = 1.4$ A, and $I_3 = 1.2$ A. The offset field is not needed in the current setup. The current to generate the MOT quadrupole field is $I_{MOT} = 30$ A.

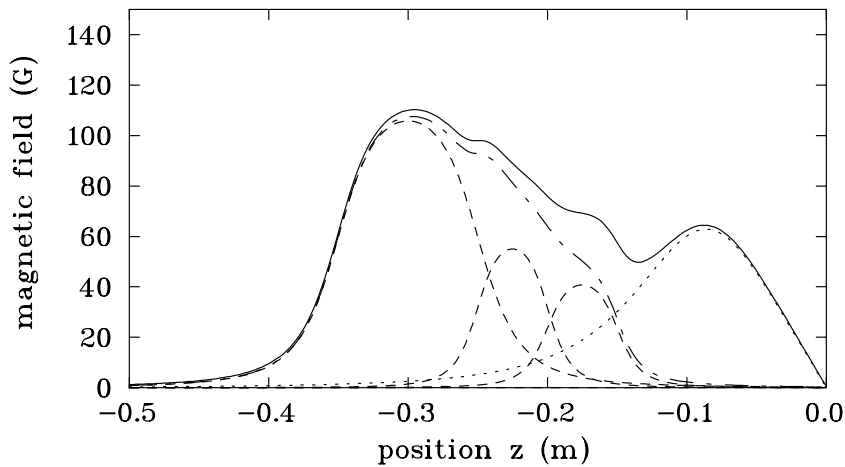


Figure B.9: Calculated longitudinal magnetic field of the Cesium Zeeman-slower together with the longitudinal MOT quadrupole field. The solid line shows the resulting, total field. The dotted line indicates the MOT field, the dashed lines correspond to each of the 3 segments of the solenoid (from left to right: #3; #2; #1). The dash-dotted line shows the total field contribution of the slower windings. The trap center is located at the origin.

The corresponding beam parameters, such as maximum capture velocity, behaviour of the slowing force, transverse beam velocity and -radius versus deceleration length are illustrated in Fig. B.10. Like in the case of Lithium, the curves shown in Fig. B.10 result from the integration of the equation of motion, using the calculated total magnetic field described above. The assumed slowing laser detuning is $-6\Gamma_{Cs}$ and the saturation is $S = 30$. In the upper left picture the behaviour of the resonance velocity is displayed. The maximum velocity decelerated in the Cesium Zeeman-slower is 160 m/s. The slowing process ends with a velocity of 22 m/s. Cesium atoms with such speeds can reliably be captured in the MOT. The resulting trap loading flux corresponds to typically 8.5% of the total atomic flux. Without using the Zeeman-slower the trap loading flux due to slowing in the fringe fields of the MOT is 1.7% only. This designed gain by a factor of 5 was experimentally confirmed.

In the lower left picture the behaviour of the associated decelerating force is shown. Desired is a

constant force. Due to the large saturation, we allowed a higher maximum deceleration compared to the case of Lithium. In the case of Cesium the force must not exceed 95% of the maximum spontaneous force $\hat{F} = \hbar k \gamma$ (see Eq. 3.3). Both conditions are well fulfilled.

In the upper right picture the transverse atomic velocity is given. From the beam shaping system in the differential pumping sections, the initial transverse velocity is about 1 cm/s. Due to the random character of the emitted photon momentum, the transverse velocity increases with the square root of the number of scattered photons. The resulting transverse beam radius is given in the lower right picture. The final atomic beam spread of about 1 mm due to photon scattering is negligible. Not considered in the simulation is the initial radius of the atomic beam of 0.75 mm. Hence the total radius of the Cesium atomic beam at the trap position can be estimated as 2 mm, which is small compared to the $1/e^2$ -intensity radius of 5 mm of the Cesium MOT laser beams. Therefore we can assume that all decelerated atoms are captured in the MOT.

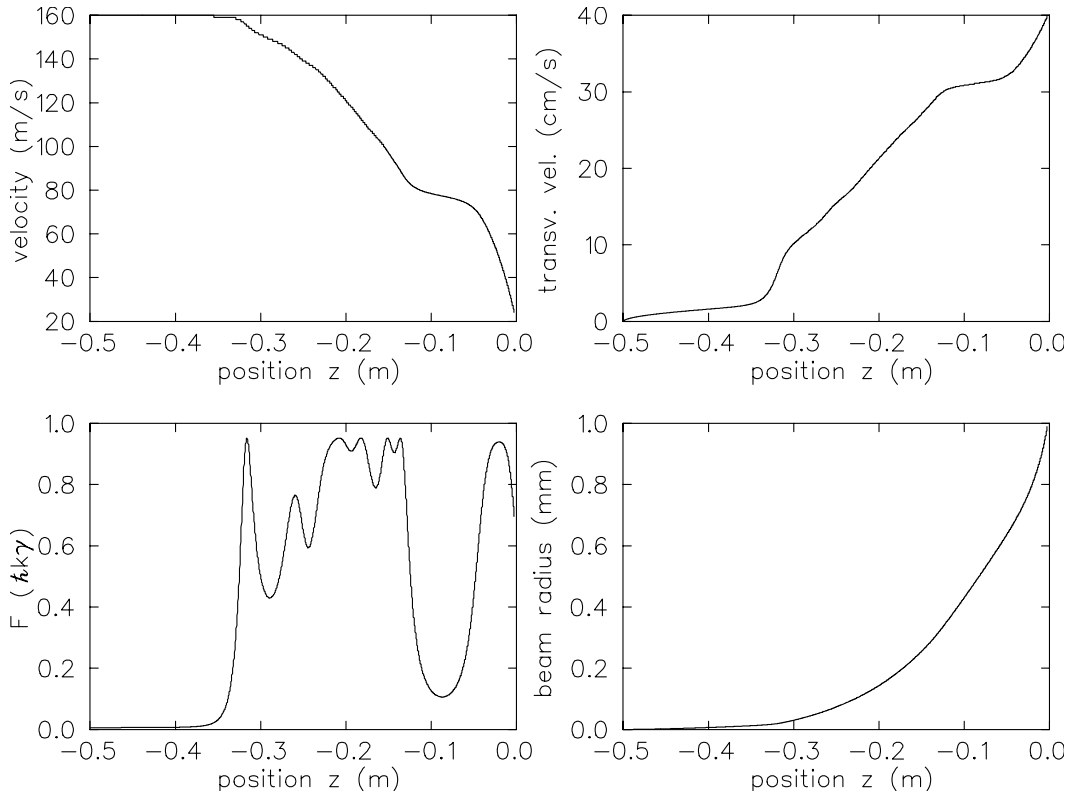


Figure B.10: Atomic beam quantities following from the designed magnetic field of the Cesium Zeeman-slower. In the **upper left** picture the atomic resonance velocity versus deceleration length is given. In the **lower left** picture the behaviour of the associated decelerating force is shown. The behaviour of the transversal velocity due to photon scattering is displayed in the **upper right** picture, and the resulting transversal blow-up of the atomic beam is shown in the **lower right** picture.

We could not measure the Cesium Zeeman-slower field in order to equalize it with the cal-

culated field. Therefore we adjusted the currents by optimizing the trap loading. Starting with segment number one we gradually optimized the current through each segment. Table B.4a gives the actual currents, they are in good agreement with the designed values, also given in Table B.4a. This nice agreement and the fact that the loading flux is indeed increased by a factor of 5 when the Cesium Zeeman-slower is used, shows the exactness and reliability of the field simulation.

segment	1	2	3	offset
designed current [A]	2.4	1.4	1.2	0
actual current [A]	2.25	1.34	1.47	0

Table B.4a: *Actual and designed currents in each segment of the Cs Zeeman-slower.*

Appendix C

Polarization-gradient cooling of Cesium in free space

Since the transfer efficiency strongly depends on the temperature of the atomic sample provided by the MOT, we closely investigated polarization-gradient cooling on Cesium in free space. A series of experiments on various combinations between detuning, intensity and duration of cooling was performed. The prerequisite for these experiments was a well equalized magnetic field in the area of the atoms. This short section gives an overview on typically achieved temperatures in our Cesium MOT and molasses for different experimental conditions. To determine the temperature we used absorption imaging technique in combination with a standard ballistic expansion method. The number of atoms in each run was on the order of 2×10^7 .

As mentioned already, for *loading* of Cesium into the MOT the cooling laser detuning is $2 \Gamma_{Cs}$ to the red side of the transition $F = 4 \rightarrow F' = 5$, while the repumper is resonant with the transition $F = 3 \rightarrow F' = 4$. Under these conditions the temperature of the trapped atoms is $74 (\pm 6) \mu\text{K}$, which is already below the Doppler temperature of $130 \mu\text{K}$. It is interesting to note that even for such a small detuning sub-Doppler cooling is significantly present already in the case of Cesium.

With our standard *MOT red-detuned molasses cooling* scheme at a MOT repumper detuning of $-27 \Gamma_{Cs}$ and in the presence of the magnetic quadrupole field the temperature drops to $25 (\pm 2) \mu\text{K}$. *Extending the red-detuned molasses cooling*, using the MOT laser (at a detuning of $-27 \Gamma_{Cs}$), to periods after the magnetic quadrupole field was turned off, led to temperatures of $7 (\pm 2) \mu\text{K}$. Here the extended cooling period had to be applied longer than 4 ms.

By using the *grating stabilized laser*, we reduced the temperature further. Applying *red-detuned*

*molasses in free space*¹ on the $F = 4 \rightarrow F' = 5$ transition led to a temperature of $2.3 (\pm 1) \mu\text{K}$ for a detuning of $-10 \Gamma_{Cs}$ at an intensity of about $I_{MOT}/3$. A repumper was needed, resonant with the $F = 3 \rightarrow F' = 4$ transition. The final temperature was reached for cooling times of at least 7 ms.

Applying *blue-detuned molasses in free space*, yielded for both cooling transitions $F = 3 \rightarrow F' = 2$ and $F = 3 \rightarrow F' = 3$ temperatures of $1.7 (\pm 0.5) \mu\text{K}$. Here the detuning was in both cases $+6 \Gamma_{Cs}$. The repumper was tuned resonantly on the $F = 4 \rightarrow F' = 4$ transition, its detuning had no influence. The final temperature was reached after 2 ms cooling and did not drop further for longer cooling times. This temperature is one of the lowest ever achieved with polarization-gradient cooling on Cesium, see [Boi96, Tri99]. Fig. C.1 shows a ballistic expansion measurement for blue-detuned molasses cooling in free space on the $F = 3 \rightarrow F' = 3$ transition.

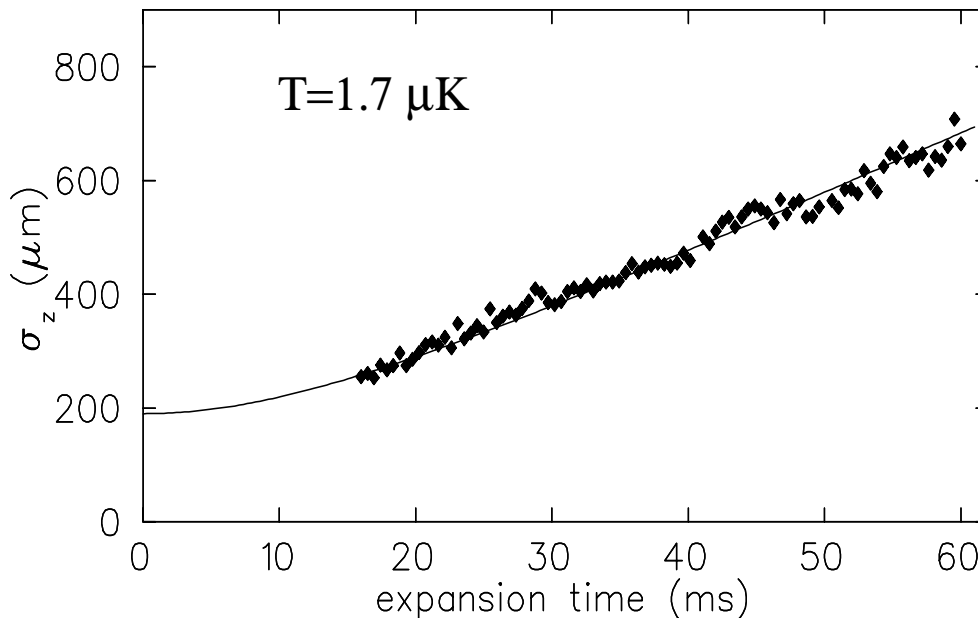


Figure C.1: Ballistic expansion measurement after 4 ms blue-detuned molasses cooling in free space on the $F = 3 \rightarrow F' = 3$ transition of Cesium; $t=0$ denotes the time when blue-detuned molasses was turned off. The fitted temperature is $1.7 \mu\text{K}$. The data is taken by absorption imaging technique, the total number of atoms was about 2×10^7 .

It is interesting to note the difference in detuning for optimized blue-detuned molasses cooling in presence and absence of the CO_2 -laser. Optimized transfer was given at detunings of $+5 \Gamma_{Cs}$ (CO_2 -laser on), while in free space the lowest temperature was achieved at $+6 \Gamma_{Cs}$. The difference corresponds well to the maximum light shift of $1.6 \Gamma_{Cs}$ caused by the CO_2 -laser. When we repeated the run with the optimized detuning for cooling in presence of the CO_2 -laser, in free space

¹Meaning after release from the MOT, hence magnetic quadrupole field and MOT laser turned off.

the resulting temperature was $3.3 (\pm 0.8) \mu\text{K}$. Simply by turning back to $+6 \Gamma_{Cs}$ the temperature minimum of about $1.7 \mu\text{K}$ was achieved again. As it turned out during the experiments with blue-detuned molasses cooling, the detuning had to be adjusted on an accuracy of half a linewidth, since the temperature depends critically on the detuning. Due to the larger detuning in red-detuned molasses the dependence of the temperature on detuning was less critical, here a significant temperature change was realized for a difference in detuning of about 2 linewidths.

Appendix D

Absorption imaging

This section is based on [Gri99]. Consider a given density distribution $n(\vec{r})$ with the total number of atoms $N = \int d^3r n(\vec{r})$. For a probe laser propagating in z -direction, the absorptive effect of the atoms is described by the x - and y -dependent transmission factor

$$T(x, y) = \exp[-\sigma \eta(x, y)], \quad (\text{D.1})$$

where σ denotes the cross section for absorption and $\eta(x, y) = \int dz n(\vec{r})$ gives the column density in the x - y -plane. Assuming a Gaussian distribution of the atom cloud with a number density $n(\vec{r}) = \hat{n} \exp[-(\frac{x}{x_0})^2 - (\frac{y}{y_0})^2 - (\frac{z}{z_0})^2]$, where x_0 , y_0 and z_0 denote the $1/e$ -radii of the cloud. The corresponding column density is

$$\eta(x, y) = \hat{\eta} e^{-(x/x_0)^2} e^{-(y/y_0)^2} \quad (\text{D.2})$$

with the peak column density $\hat{\eta} = \sqrt{\pi} z_0 \hat{n}$ related to the peak number density \hat{n} . The transmission factor of the cloud is now expressed as

$$T(x, y) = \exp\left[-\sigma \hat{\eta} e^{-(x/x_0)^2} e^{-(y/y_0)^2}\right]. \quad (\text{D.3})$$

A two dimensional fit of this equation to the observed absorption image (quotient of the two pictures) yields the three parameters $\sigma \hat{\eta}$, x_0 and y_0 .

To get an absolute number on $\hat{\eta}$, one has to calculate the value of the cross section σ . In the case of low saturation the resonant absorption cross section σ_{res}^* for a two level transition is

$$\sigma_{res}^* = \frac{3}{2\pi} \lambda^2. \quad (\text{D.4})$$

Taking a small detuning δ into account, the resonant absorption cross section has to be modified due to the typical Lorentz shape of the resonance:

$$\sigma^* = \frac{3}{2\pi} \lambda^2 \frac{1}{1 + (2\delta/\Gamma)^2}. \quad (\text{D.5})$$

Since real atoms are not two level systems, the line strengths of the various ground state excitations must be considered. The relative line strength is given by the squared Clebsch-Gordon coefficient $C(F, m_F; 1, q; F', m_{F'})$. Assuming equal distribution between the magnetic sub-states in the atomic ground state one has to take the average over the squared relative Clebsch-Gordon coefficients of the excited transition [Zie99].

For Cesium atoms in the upper hyperfine ground state, the absorption cross section for the $F=4 \rightarrow F'=5$ transition excited by π -polarized light at weak intensity, is

$$\sigma_{Cs} = 0.1945 \frac{\lambda_{Cs}^2}{1 + (2\delta/\Gamma_{Cs})^2}. \quad (\text{D.6})$$

The laser detuning is given by δ and $\Gamma_{Cs} = 2\pi \times 5.3$ MHz is the natural linewidth of the Cesium transition at $\lambda_{Cs} = 852$ nm.

In the case of Lithium and excitation of the $F=2 \rightarrow F'=3$ transition with π -polarized light, the cross section is

$$\sigma_{Li} = 0.2228 \frac{\lambda_{Li}^2}{1 + (2\delta/\Gamma_{Li})^2}, \quad (\text{D.7})$$

with $\Gamma_{Li} = 2\pi \times 5.87$ MHz and $\lambda_{Li} = 671$ nm.

Now the total number of atoms can be calculated as

$$N = \pi x_0 y_0 \hat{\eta}. \quad (\text{D.8})$$

This is the result assuming absolutely monochromatic light. In reality the linewidth of the probe laser is larger than the natural linewidth Γ , which causes reduced maximum absorption. To compensate for that, one has to fold the Gaussian frequency distribution of the laser with the Lorentz profile of the transition.

The resulting width in the case of Cesium was $2\pi \times 16$ MHz $\approx 3 \times \Gamma_{Cs}$. A three times wider Lorentz profile causes a reduction of the maximum absorption $\hat{\eta}$ by a factor of 1/3, when keeping the curve integral constant. Hence the actual number of Cesium atoms is three times larger than calculated in Eq. D.8.

In the case of Lithium absorption imaging did not work properly so far. When this technique was applied in the QUEST, the total number of atoms was too low and hence the density as well. When used in ballistic expansion measurements from the MOT, the cloud was too hot and therefore spread out too fast, resulting again in a low density. Additionally, in the case of Lithium the regarded transition $F=2 \rightarrow F'=3$ is not ‘‘closed’’. Of course a repumping beam was applied but nevertheless roughly half their time the atoms spend in the $F=1 \rightarrow F'=2$ transition and hence the sample appears more transparent for the probe beam.

Appendix E

Analytical model of transfer efficiency

Since the QUEST parameter such as intensity distribution $I(r, z)$ and trap depth U_0 , as well as the atomic distribution in the MOT are well known, one can calculate the expected transfer efficiency from the overlap in phase space between the MOT distribution and QUEST potential.

In good agreement with data from pictures we took of the magneto-optically trapped atoms right before transfer, one can assume a Gaussian phase space distribution in the MOT:

$$f(\vec{x}, \vec{p}) = N \frac{1}{V_{\vec{x}}} \exp\left(-\frac{x^2}{2\sigma_x^2} - \frac{y^2}{2\sigma_y^2} - \frac{z^2}{2\sigma_z^2}\right) \frac{1}{V_{\vec{p}}} \exp\left(-\frac{\vec{p}^2}{2mk_B T}\right) \quad (\text{E.1})$$

with the normalization

$$V_{\vec{x}} = (2\pi)^{3/2} \sigma_x \sigma_y \sigma_z, \quad V_{\vec{p}} = (2\pi)^{3/2} (mk_B T)^{3/2}.$$

Integrating Eq. E.1 yields the total number of atoms N :

$$\int d^3x d^3p f(\vec{x}, \vec{p}) = N. \quad (\text{E.2})$$

Here a sufficient ergodicity of the potential is presumed, what basically means that the momentum distribution is not a function of \vec{x} .

An atom is successfully transferred into the QUEST, if the sum of its kinetic energy $E_{kin} = \vec{p}^2 / (2m)$ and potential energy $U(\vec{x})$ is not exceeding the potential depth U_0 :

$$U_0 - U(\vec{x}) - \frac{\vec{p}^2}{2m} \leq 0. \quad (\text{E.3})$$

Using Eq. E.3 for limiting the phase space distribution one calculates the number of transferred atoms from:

$$N_T = \int d^3x d^3p f(\vec{x}, \vec{p}) \theta \left(U_0 - U(\vec{x}) - \frac{\vec{p}^2}{2m} \right) \quad (\text{E.4})$$

$$= N \frac{1}{V_{\vec{x}}} \int d^3x e^{-\frac{x^2}{2\sigma_x^2} - \frac{y^2}{2\sigma_y^2} - \frac{z^2}{2\sigma_z^2}} \frac{4\pi}{V_{\vec{p}}} \int_0^{\hat{p}} dp p^2 e^{-\frac{p^2}{2mk_B T}}, \quad (\text{E.5})$$

Expression E.4 describes the projection of the phase space distribution in the MOT onto the dipole trap. The Heavyside step function $\theta \left(U_0 - U(\vec{x}) - \frac{\vec{p}^2}{2m} \right)$ equals 1 when the total energy of the atoms in the QUEST is smaller than the trap depth, and 0 elsewhere; $\hat{p}(\vec{x}) = \sqrt{2m(U_0 - U(\vec{x}))}$ denotes the maximum momentum of a trapped atom at position \vec{x} . This cut-off condition is implemented in the integral of momentum distribution.

The last term in Eq. E.5 can be brought into the form:

$$\frac{4\pi}{V_{\vec{p}}} \int_0^{\hat{p}} dp p^2 e^{-\frac{p^2}{2mk_B T}} = \frac{4\pi}{V_{\vec{p}}} \int_0^{\hat{\kappa}} d\kappa \kappa^2 e^{-\kappa^2}, \quad \hat{\kappa} = \sqrt{\frac{U_0 - U(\vec{x})}{k_B T}} \quad (\text{E.6})$$

$$\begin{aligned} &= \text{Erf}(\hat{\kappa}) - \frac{2}{\sqrt{\pi}} \hat{\kappa} e^{-\hat{\kappa}^2} \\ &= \frac{4}{\sqrt{\pi}} \sum_{l=1}^{\infty} \frac{(-1)^{l+1}}{(2l+1)(l-1)!} \hat{\kappa}^{2l+1}. \end{aligned} \quad (\text{E.7})$$

Plug-in of expression E.7 into Eq. E.5 yields:

$$N_T = N \frac{1}{V_{\vec{x}}} \int d^3x e^{-\frac{x^2}{2\sigma_x^2} - \frac{y^2}{2\sigma_y^2} - \frac{z^2}{2\sigma_z^2}} \frac{4}{\sqrt{\pi}} \sum_{l=1}^{\infty} \frac{(-1)^{l+1}}{(2l+1)(l-1)!} \hat{\kappa}^{2l+1} \quad (\text{E.8})$$

$$= N \frac{4}{\sqrt{\pi}} \sum_{l=1}^{\infty} \frac{(-1)^{l+1}}{(2l+1)(l-1)!} \frac{1}{V_{\vec{x}}} \int d^3x e^{-\frac{x^2}{2\sigma_x^2} - \frac{y^2}{2\sigma_y^2} - \frac{z^2}{2\sigma_z^2}} \hat{\kappa}^{2l+1}. \quad (\text{E.9})$$

The general expression of Eq. E.9 can be simplified by making use of symmetry properties of the optical dipole potential $U_0(\vec{x})$ represented in $\hat{\kappa}(\vec{x})$. In our case $U_0(\vec{x})$ gets well approximated by a three dimensional Gaussian potential:

$$U(\vec{x}) = U_0 \left[1 - \exp \left(-\frac{x^2}{2w_x^2} - \frac{y^2}{2w_y^2} - \frac{z^2}{2w_z^2} \right) \right], \quad (\text{E.10})$$

yielding

$$\hat{\kappa}(\vec{x}) = \sqrt{\frac{U_0}{k_B T}} \exp \left[\frac{1}{2} \left(-\frac{x^2}{2w_x^2} - \frac{y^2}{2w_y^2} - \frac{z^2}{2w_z^2} \right) \right] \quad (\text{E.11})$$

This expression factorizes into single terms of one dimension only. Thus the 3 dimensional integration in Eq. E.9 splits into a product of three one dimensional integrals of the form:

$$\int_{-\infty}^{+\infty} di \exp \left(-\frac{i^2}{2\sigma_i^2} \right) \exp \left(-(2l+1) \frac{i^2}{2w_i^2} \right) = \sqrt{2\pi} \frac{\sigma_i}{\sqrt{1 + (2l+1) \frac{\sigma_i^2}{w_i^2}}}, \quad (\text{E.12})$$

where $i = x; y; z$. Hence the total expression of Eq. E.9 can be written in the form:

$$N_T = N \frac{4}{\sqrt{\pi}} \sum_{l=1}^{\infty} \frac{(-1)^{l+1}}{(2l+1)(l-1)!} \eta^{l+1/2} \prod_{i=x;y;z} \frac{1}{\sqrt{1 + (2l+1) \frac{\sigma_i^2}{w_i^2}}} \quad (\text{E.13})$$

The parameter $\eta = \frac{U_0}{k_B T}$ denotes the optical dipole potential depth in terms of the ensemble temperature T .

The sum of Eq. E.13 can be calculated numerically by mathematica[©]. The only free parameters are η , σ_i and w_i , they all are well known in our experiment: η and the final MOT radii $\sigma_x, \sigma_y, \sigma_z$ depend on the regarded species, while $w_x = w_y \equiv w_0 = 108 \mu\text{m}$ is given by the CO₂-laser waist and $w_z \equiv z_R = 2.4 \text{ mm}$ by the Rayleigh range of the CO₂-laser beam.

Bibliography

- [Ada95] C. S. Adams, H. J. Lee, N. Davidson, M. Kasevich and S. Chu, Phys. Rev. Lett. **74**, 3577 (1995).
- [Ada96] C.S. Adams and E. Riis, *Laser cooling and trapping of neutral atoms*, (Progress in Quantum Electronics, 1996).
- [Arn97] M. Arndt, M. Ben Dahan, D. Guéry-Odelin, M. W. Reynolds and J. Dalibard, Phys. Rev. Lett. **79**, 625 (1997).
- [Asp86] A. Aspect, J. Dalibard, A. Heidmann, C. Salomon and C. Cohen-Tannoudji, Phys. Rev. Lett. **57**, 1688 (1986).
- [Bal99] S. Bali, K.M. O'Hara, M.E. Gehm, S.R. Grande and J.E. Thomas, Phys. Rev. A **60**, R29 (1999).
- [Ber87] T. Bergeman, Gidon Erez and Harold Metcalf, Phys. Rev. A **35**, 1535 (1987).
- [Ber95] J.C. Bergquist, *Symposium on Frequency Standards and Metrology*, (World Scientific, Singapore, 1995) .
- [Boi95] D. Boiron, C. Triche, P. Verkerk D.R. Meacher and G. Grynberg, Phys. Rev. A **52**, R3425 (1995).
- [Boi96] D. Boiron, A. Michaud, P. Lemonde, Y. Castin and C. Salomon, Phys. Rev. A **53**, R3734 (1996).
- [Boi98] D. Boiron, A. Michaud, J. M. Fournier, L. Simard, M. Sprenger, G. Grynberg and C. Salomon, Phys. Rev. A **57**, R4106 (1998).
- [Bra95] C. C. Bradley, C. A. Sackett, J. J. Tollett and R. G. Hulet, Phys. Rev. Lett. **75**, 1687 (1995).
- [Bra97] C. C. Bradley, C. A. Sackett and R. G. Hulet, Phys. Rev. Lett. **78**, 985 (1997).
- [Chu86] S. Chu, J. Bjorkholm, A. Ashkin and A. Cable, Phys. Rev. Lett. **57**, 314 (1986).

- [Coh92] C. Cohen-Tannoudji, J. Dupont-Roc and G. Grynberg, *Atom-Photon-Interactions*, (Wiley, New York, 1992) .
- [Dal85] J. Dalibard and C. Cohen-Tannoudji, *J. Opt. Soc. Am. B* **2**, 1707 (1985).
- [Dal89] J. Dalibard and C. Cohen-Tannoudji, *J. Opt. Soc. Am. B* **6**, 2023 (1989).
- [Dre94] M. Drewsen, Ph. Laurent, A. Nadir, G. Santarelli and C. Salomon, *Appl. Phys. B* **59**, 283 (1994).
- [Eic91] J. Eichler and H.-J. Eichler, *Laser: Grundlagen, Systeme, Anwendungen*, (Springer-Verlag, Berlin, Heidelberg, New York, 1991) 2. edition.
- [Eng97] H. Engler, “Aufbau eines ‘Zeeman-Abbremsers’ und Inbetriebnahme einer magnetooptischen Falle für Lithium-Atome”, Master’s thesis Universität Heidelberg and Max-Planck-Institut für Kernphysik 1997.
- [Fer99] G. Ferrari, M.-O. Mewes, F. Schreck and C. Salomon, *Opt. Lett.* **24**, 151 (1999).
- [Fri98a] S. Friebe, *Mikrofallen aus Licht zur Speicherung kalter Atome*, PhD thesis MPQ236, Max-Planck-Institut für Quantenoptik, Munich, 1998.
- [Fri98b] S. Friebe, C. D’Andrea, J. Walz, M. Weitz and T. W. Hänsch, *Phys. Rev. A* **57**, 20 (1998).
- [Fri98c] S. Friebe, R. Scheunemann, J. Walz, T. W. Hänsch and M. Weitz, *Appl. Phys. B* **67**, 699 (1998).
- [Gor80] J. P. Gordon and A. Ashkin, *Phys. Rev. A* **21**, 1606 (1980).
- [Gre95] K.O. Greulich, *Micromanipulation by light in Biology and Medicine - The laser microbeam and optical tweezers*, (Birkhäuser, Basel, 1995) .
- [Gri99] R. Grimm, Sminar on laser cooling and related topics (1999).
- [Gri00] R. Grimm, M. Weidemüller and Y. Ovchinnikov, *Adv. At. Mol. Opt. Phys.* **42** (2000).
- [Gué98] D. Guéry-Odelin, J. Söding, P. Desbiolles and J. Dalibard, *Optics Express* **2** (1998).
- [Hei99] D.J. Heinzen, “Ultracold atomic interactions”, in , *Proceedings of the International School of Physics - Enrico Fermi*, edited by M. Inguscio, S. Stringari and C. E. Wieman, (IOS Press, 1999) , S. 67.
- [Hes87] Harald F. Hess, Gregory P. Kochanski, John M. Doyle, Naoto Masuhara, Daniel Kleppner and Thomas J. Greytak, *Phys. Rev. Lett.* **59**, 672 (1987).

- [Jac62] J. D. Jackson, *Classical electrodynamics*, (Wiley, New York, USA, 1962) .
- [Kas92] A. Kastberg, W. D. Phillips, S. L. Rolston and R. J. C. Spreeuw, Phys. Rev. Lett. **74**, 1542 (1992).
- [Ker99] A.J. Kermann, V. Vuletić, C. Chin and S. Chu, Phys. Rev. Lett. **84**, 439 (1999).
- [Ket96] Wolfgang Ketterle and N. J. van Druten, Adv. At. Mol. Opt. Phys. **37**, 181 (1996).
- [Ket99] W. Ketterle, D. S. Durfee and D. M. Stamper-Kurn, “Making, probing and understanding Bose-Einstein condensates”, in , *Proceedings of the International School of Physics - Enrico Fermi*, edited by M. Inguscio, S. Stringari and C. E. Wieman, (IOS Press, 1999) , S. 67.
- [Kuh96] A. Kuhn, H. Rerrin, W. Hänsel and C. Salomon, *SOA TOPS on ultracold atoms and BEC*, edited by K. Burnett, Optical Society of America, Washington D.C. (1996).
- [Lee96] H. J. Lee, C. S. Adams, M. Kasevich and S. Chu, Phys. Rev. Lett. **76**, 2658 (1996).
- [Lem95] P. Lemonde, O. Morice, E. Peik, J. Reichel, H. Perrin, W. Hänsel and C. Salomon, Europhys. Lett. **32**, 555 (1995).
- [Let88] P. D. Lett, R. N. Watts, C. I. Westbrook, W. D. Phillips, P. L. Gloud and H. J. Metcalf, Phys. Rev. Lett. **61** (1988).
- [Lid90] D.R. Lide, *CRC Handbook of Chemistry and Physics*, (CRC Press, Boca Raton, 1990) .
- [Lui96] O.J. Luiten, M.W. Reynolds and J.T.M. Walraven, Phys. Rev. A **53**, R381 (1996).
- [Mar66] R. Marrus, D. Malcom and J. Yellin, Phys. Rev. Lett. **147** (1966).
- [McA95] W. I. McAlexander, E. R. I. Abraham, N. W. M. Ritchie, C. J. Williams, H. T. C. Stoof and R. G. Hulet, Phys. Rev. Lett. **51**, 871 (1995).
- [Met94] H. Metcalf and P. van der Straten, Phys. Rep. **244** (1994).
- [Met95] H. Metcalf and P. van der Straten, *Laser Cooling and Trapping*, (Springer-Verlag New York, USA, 1995) .
- [Mew99] M.-O. Mewes, G. Ferrari, F. Schreck, A. Sinatra and C. Salomon, physics/99090007 (1999).
- [Mil93] J. D. Miller, R. A. Cline and D. J. Heinzen, Phys. Rev. A **47**, R4567 (1993).

- [Min87] V. G. Minogin and V. S. Letokhov, *Laser Light Pressure on Atoms*, (Gordon and Breach, New York, 1987) .
- [Mor91] G. Moruzzi and F. Strumia, *The Hanle Effect and Level-Crossing Spectroscopy*, (Plenum Press, New York/London, 1991) .
- [Nes63] A. N. Nesmeyanov, *Vapour Pressure of the Chemical Elements*, (North Holland, Amsterdam, 1963) .
- [Nil99] M. Nill, “Eine quasi-elektrostatische Laserfalle für Cäsium und Lithium”, Master’s thesis Universität Heidelberg and Max-Planck-Institut für Kernphysik 1999.
- [O’H99] K.M. O’Hara, S.R. Granade, M.E. Gehm, T.A. Savard, S. Bali, C. Freed and J.E. Thomas, *Phys. Rev. Lett.* **82**, 4204 (1999).
- [Raa87] E. L. Raab, M. Prentiss, A. Cable, S. Chu and D. E. Pritchard, *Phys. Rev. Lett.* **59**, 2631 (1987).
- [Sal90] C. Salomon, J. Dalibard, W.D. Phillips and S. Guelatti, *Europhys. Lett.* **12**, 683 (1990).
- [Sav97] T. A. Savard, K. M. O’Hara and J. E. Thomas, *Phys. Rev. A* **56**, R1095 (1997).
- [Sch73] G. Schnell, *Magnete*, (Verlag Karl Thiemig, München, 1973) .
- [Sch98a] U. Schlöder, “Ultrakalte Stöße zwischen Lithium- und Cäsiumatomen in einer kombinierten magnetooptischen Falle”, Master’s thesis Universität Heidelberg and Max-Planck-Institut für Kernphysik 1998.
- [Sch98b] U. Schünemann, H. Engler, M. Zielonkowski, M. Weidemüller and R. Grimm, *Opt. Commun.* **158**, 263 (1998).
- [Sch99] U. Schlöder, H. Engler, U. Schünemann, R. Grimm and M. Weidemüller, *Eur. Phys. J. D* **7**, 331 (1999).
- [Ses89] D. Sesko, T. Walker, C. Monroe, F. Gallagher and C. Wieman, *Phys. Rev. Lett.* **63**, 961 (1989).
- [Sie86] A. E. Siegman, *Lasers*, (University Science Books, Mill Valley, Ca, USA, 1986) .
- [Sin95] A.G. Sinclair and E. Riis, *Opt. Comm.* **14**, 527 (1995).
- [Sta98] D. M. Stamper-Kurn, M. R. Andrews, A. P. Chikkatur, S. Inouye, H.-J. Miesner, J. Stenger and W. Ketterle, *Phys. Rev. Lett.* **80**, 2027 (1998).
- [Tak95] T. Takekoshi, J. R. Yeh and R. J. Knize, *Opt. Comm.* **114**, 421 (1995).

- [Tak96] T. Takekoshi and R. J. Knize, *Opt. Lett.* **21**, 77 (1996).
- [Tak98] T. Takekoshi, B.M. Patterson and R. J. Knize, *Phys. Rev. Lett.* **5105** (1998).
- [Tho94] H. R. Thorsheim, J. Weiner and P. S. Julienne, *Phys. Rev. Lett.* **58**, 2204 (1994).
- [Tor98] Y. Torii, N. Shiokawa, T. Kuga, Y. Shimizu and H. Sasda, *J. Phys. J. D.* **1**, 239 (1998).
- [Tow96] C. Townsend, N. Edwards, K. Zetie, C. Cooper and C. Foot, *Phys. Rev. A* **52**, 1423 (1996).
- [Tri99] C. Triche, P. Verkerk and G. Grynberg, *J. Phys. J. D.* **5**, 225 (1999).
- [Ver94] P. Verkerk, D. R. Meacher, A. B. Coates, J.-Y. Courtois, S. Guibal, B. Lounis, C. Salomon and G. Grynberg, *Europhys. Lett.* **26**, 171 (1994).
- [Vul99] V. Vuletić, C. Chin and S. Chu, *Phys. Rev. Lett.* **82**, 1406 (1999).
- [Wal94] T. Walker and P. Feng, *Advances in Atomic, Molecular and Optical Physics*, Vol. **34**, 125 (1994).
- [Wea88] R. C. Weast, *CRC Handbook of Chemistry and Physics*, (CRC Press, Boca Raton, Florida, 1988) 69th ed.
- [Web00] T. Weber, “Langzeitspeicherung verschiedener atomarer Spezies in einer quasi-elektrostatischen Dipolfalle”, Master’s thesis Universität Heidelberg and Max-Planck-Institut für Kernphysik 2000.
- [Wei94] M. Weidemüller, T. Esslinger, M.A. Ol’Shanii, A. Hemmerich and T.W. Hänsch, *Europhys. Lett.* **27**, 109 (1994).
- [Wei99a] M. Weidemüller and R. Grimm, *Physikalische Blätter* **55**, 41 (1999).
- [Wei99b] J. Weiner, V.S. Bagnato, S. Zilio and P. Julienne, Experiments and theory in cold and ultracold collisions. *Rev. Mod. Phys.* **71**, 1 (1999).
- [Wei00] M. Weidemüller, “Mixtures of ultracold atoms and the quest for ultracold molecules”, Habilitations Schrift, Universität Heidelberg (2000).
- [Win92] L. Windholz, M. Musso, G. Zerza and H. Jäger, *Phys. Rev. A* **46**, 5812 (1992).
- [Win98] S.L. Winoto, M.T. DePu, N.E. Bramall and D.S. Weiss, *Phys. Rev. A* **53**, R3734 (1998).
- [Wit87] W. J. Witteman, *The CO₂ [CO] Laser*, (Springer-Verlag, Berlin, Heidelberg, New York, 1987) .
- [Zie99] M. Zielonkowski, *Spindynamik von Alkaliatomen in Lichtfeldern*, PhD thesis Universität Heidelberg and Max-Planck-Institut für Kernphysik 1999.